8-2018

Modeling and Performance Analysis of A Sloshing Ferrofluid Based Electromagnetic Energy Harvester

Qi Liu
Clemson University, iamllqq@gmail.com

Modeling and Performance Analysis of a Sloshing Ferrofluid Based Electromagnetic Energy Harvester

---

A Dissertation
Presented to
the Graduate School of
Clemson University

In Partial Fulfillment
of the Requirements for the Degree
Doctor of Philosophy
Mechanical Engineering

---

by
Qi Liu
August 2018

Accepted by:
Dr. Gang Li, Committee Chair
Dr. Mohammed Daqaq
Dr. Lonny Thompson
Dr. Xiangchun Xuan

Abstract

Computational modeling and performance analysis are carried out for a ferrofluid based electromagnetic energy harvester which converts ambient vibratory energy into electromotive force through sloshing motion of a ferrofluid. The system consists of a tank partially filled with ferrofluid, magnets placed on the opposite sides of the tank and a copper coil wound around the tank. In the presence of an external magnetic field, magnetic dipoles in the ferrofluid rotate and produce a net magnetic moment aligned in the direction of the field. When the device is subjected to an external excitation, the ferrofluid in the tank undergoes a sloshing motion which induces a time-varying magnetization in the fluid, causing a time-varying magnetic flux and electromotive force in the copper coil according to Faraday's law of induction. Compared to traditional solid-state vibratory energy harvesters, this liquid-state harvester provides better conformability, sensitivity, tunability and response bandwidth. This study provides useful insights for designing high performance ferrofluid based energy harvesters and is divided into three sections.

First, A continuum level finite element model is developed and implemented for the multi-physics computational analysis of the energy harvester. The model solves the coupled magnetic scalar potential equation and Navier-Stokes equations for the dynamic behavior of the magnetic field and fluid motion. The model is validated against experimental results for eight configurations of the system. The validated model is then employed to study the underlying mechanisms that determine the electromotive force of the energy harvester.

Furthermore, computational analysis is performed to test the effects of several modeling aspects, such as three-dimensional effect, surface tension and type of the ferrofluid-magnetic field coupling, on the accuracy of the model prediction.

Second, a series of numerical simulations are performed to investigate the influence of several design parameters on the electromotive force of the energy harvester. From the eight configurations used for model validation, two configurations that give the highest electromotive forces are chosen for further performance analysis. The design parameters considered in this investigation include the device's geometric parameters, external excitation amplitude and material properties of the ferrofluid, which affect either the magnetic flux in the device or the sloshing behavior of the ferrofluid.

Third, non-equilibrium molecular dynamics (NEMD) simulations are employed to obtain an understanding of the dynamic magnetization behavior of the ferromagnetic nanoparticles and microscopic structures of the ferrofluid. The results from the continuum level numerical simulations reveal that the magnetic susceptibility/magnetization of ferrofluid greatly influences the performance of the energy harvester. Since the ferrofluid in the energy harvester undergoes sloshing motion under external mechanical excitations, it is also expected that fluid motion would significantly influence the aggregation behavior of the nano-particles, thereby playing an important role in determining the magnetization of the ferrofluid and the performance of the energy harvester. In this study, ferrofluid systems containing both small and large particles under the influence of both magnetic field and shear flow are considered. The computational model involves long-range dipolar interaction as well as short-range repulsive interaction of the nano-particles. The factors investigated include solvent friction coefficients, particle size, magnetic field strength and direction, and shear rate.

Table of Contents

List of Figures

Chapter 1

Introduction

1.1 Background and Motivation

Energy harvesting (also known as power harvesting or energy scavenging) is a process by which energy is derived from external sources (e.g. solar power, thermal energy, wind energy, salinity gradients, and kinetic energy, also known as ambient energy), and converted to electric energy to power micro electronics such as wireless sensors, actuators and implantable medical devices, which require only sub-milliwatts to function. Battery, being the current most widely used power option, is unfortunately left behind compared to the development of wireless devices, especially in terms of energy density [6]. Besides, battery replacement can be difficult, costly or dangerous in certain situations. For example, continuous battery replacement is extremely laborious for networks with thousands of physically embedded wireless sensor nodes [7]. Changing batteries for patients' implantable pace makers is very inconvenient and dangerous. On the other hand, mechanical vibrations exist ubiquitously in applications including industrial plant equipment, man-made structures and so on. Innovative energy harvesting designs that are able to utilize vibration energy and provide continuous power supply for wireless devices will be very

meaningful.

1.2 Current Approach: Solid-State Energy Harvesting

Because of the unsatisfactory performance of current batteries and low-power consumption of newly-designed electronics, in recent decades, energy harvesting using micro-power generators (MPGs) has received considerable attention and been investigated extensively in the literature [8–14]. Among the energy harvesting methods, vibratory energy harvesting has become one of the focal areas. Much work has been done to convert mechanical vibrations to electric energy through piezoelectric, magnetostrictive, electrostatic or electromagnetic mechanism [8].

Solid-state materials are typically used as the working material of vibratory energy harvesters. For example, as shown in Fig. 1.1, the strain generated in a piezoelectric beam is transformed into electric charge through the piezoelectric effect, and the strain in a magnetostrictive rod is transformed into magnetic field through the Villari effect [2, 15–17]. In the electrostatic mechanism as shown in Fig. 1.2a, one charged plate moves relative to another oppositely charged plate to provide the electric energy [8]. In electromagnetic energy harvesting, as shown in Fig. 1.2b, electric potential is generated by either the relative movement of the magnet and coil, or by a change in the magnetic field [18–20]. However, the applications of solid-state energy harvesters may be limited due to the difficulty in conforming to different shapes, narrow bandwidth and low sensitivity to external excitations.

1.3 Proposed Approach: Liquid-State Energy Harvesting

Recently, ferrofluid has become a good alternative to solid-state materials in energy harvesting, due to its unique combination of magnetic characteristics and liquid state

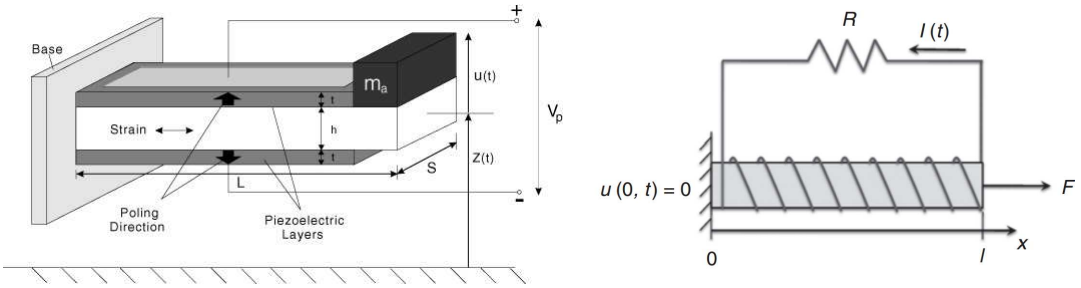

(a) (b)

Figure 1.1: (a) A typical piezoelectric power generator [1]. (b) Schematic diagram of a magnetostrictive energy harvester subjected to axial vibrations [2].

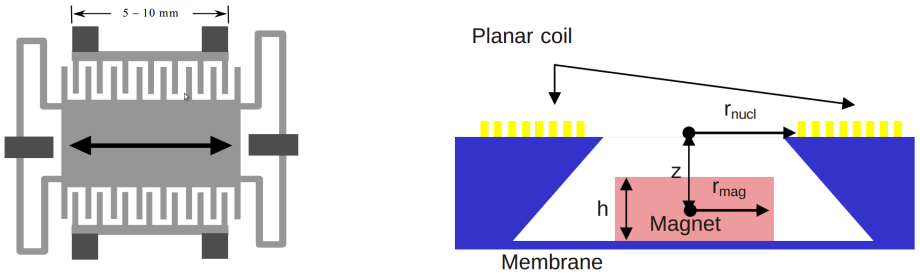

(a) (b)

Figure 1.2: (a) Schematic diagram of an electrostatic energy harvester [3]. (b) Schematic cross section of an electromagnetic energy harvester [4].

which can overcome the aforementioned conformability, bandwidth and sensibility issues. Ferrofluid is a colloidal liquid with nanoscale magnetic particles suspended in a water or organic carrier liquid. A ferrofluid particle can be regarded as a single magnetic domain with a permanent dipole moment fixed at its center. To prevent agglomeration of the magnetic nanoparticles, the particles are stabilized either sterically by being coated with long-chain surfactant or electrostatically by including charged groups. In the absence of an external magnetic field, magnetic dipoles in ferrofluid are randomly oriented and the overall magnetization is zero. With applied external magnetic field, ferrofluid behaves in a way similar to a paramagnetic material. The dipoles rotate to produce a net magnetic moment which aligns in the direction of the magnetic field. Some other energy harvesters have

also used ferrofluid in various configurations. Refs. [21–24] used ferrofluid as a liquid bearing/lubricant and Ref. [25] as a liquid spring in a spring-mass electromagnetic energy harvester. Ref. [26] studied an electromagnetic energy harvester utilizing air bubble movement in a ferrofluid filled channel. Ref. [27] proposed an electrostatic energy harvester with magnetic field-driven ferrofluid droplets moving between electrodes.

Contrary to these configurations, Bibo, Alazemi et al. designed a ferrofluid based electromagnetic vibratory energy harvester [28–31] which converts ambient vibratory energy into electromotive force through the sloshing motion of a ferrofluid. Their configuration consists of a tank partially filled with ferrofluid, two permanent magnets placed on two opposite sides of the tank and a copper coil of N_{turns} turns wound around the tank either directly or through a ferromagnetic core. The entire setup is mounted on a shaker, which provides an external harmonic excitation to the tank. When the frequency of the harmonic excitation matches one of the infinite modal frequencies of the ferrofluid column, large surface waves will be generated, which induce a time-varying magnetization in the fluid, causing a time-varying magnetic flux and electromotive force in the copper coil according to Faraday's law of induction. This proposed energy harvester also inspired more research works (Ref. [32] added a back yoke to the sloshing electromagnetic energy harvester to create a closed magnetic flux path. Ref. [33] studied a sloshing triboelectric-electromagnetic hybrid generator). The proposed sloshing ferrofluid based energy harvester can make use of vibration energy and meanwhile work as a tuned liquid damper [34]. This novel energy harvesting design has the following advantages:

- **Conformability:** Being liquid, ferrofluid is able to conform to various shapes, which will inspire new design and manufacture of energy harvesters of complex shapes for more demanding work environments.

- **Sensitivity:** Liquids are much more sensitive to low-level excitations than solids are.

This is one reason why mammals' ears incorporate a fluid called Perilymph to transform mechanical vibrations from the middle ear into waves that can be carried to the sensory ducts at the end of the cochlea. Thus, it is believed that liquid-state materials are capable of responding to the smallest levels of environmental excitations including, but not limited to, the nature-common acoustic excitations.

- **Tunability:** External magnetic field and shear can change the viscosity of ferrofluid by hindering the rotation of magnetic particles through magnetic torques (magneto-viscous effect) [35]. In addition, magnetic body force can also influence the effective gravity that exerts on the ferrofluid column. Both effects can help tune the modal frequencies of the energy harvester to match the environmental vibration frequencies for higher energy conversion efficiency.

- **Bandwidth:** Most linear energy harvesters operate efficiently only within a narrow frequency bandwidth very close to the resonant frequency of the harvester. Small variations in the excitation frequency around the harvester's resonant frequency drop its small energy output even further making the energy harvesting process inefficient [36–41]. This becomes an even more pressing issue when one realizes that most environmental excitations have broad-band or time-dependent characteristics, i.e. the energy is distributed over a wide spectrum of frequencies or the dominant frequencies vary with time. Electromagnetic energy harvesters that incorporate solid-state magnets respond only at one modal frequency [42] or widely-spaced modal frequencies [43], and thus have a very narrow response bandwidth. On the contrary, a harvester incorporating liquid-state materials can respond at infinite closely-spaced frequencies, corresponding to the infinite modal frequencies of the fluid column which excite the large amplitude rotational and horizontal surface waves. The presence of a large number of closely-spaced modal frequencies can also facilitate the activation of non-

linear modal interactions between the different vibration modes. Such interactions occur when two or more modal frequencies are commensurate or nearly commensurate, i.e. multiple integers of each other [29], leading to energy exchange among the commensurate modes resulting in large-amplitude responses over a wide range of frequencies. This further enhances the broadband characteristics of the ferrofluid based harvester in the random and non-stationary environments.

1.4 Objectives

Previous experimental results demonstrated the feasibility of this promising concept, and revealed that transduction efficiency of the energy harvester depends on many factors including the magnet placement and excitation amplitude [28, 29]. However, a mathematical model that describes the interconnected relation between the fluidic, magnetic, and electric domains in this multiphysics system is still unavailable, which is essential for the investigation and optimization of energy harvester performance. The parameters that influence the performance of the energy harvester include but are not limited to the geometry of the container, the depth and material properties of the ferrofluid, the strength and spatial distribution of the magnetic field, and the excitation amplitude.

In order to elucidate the underlying macroscopic mechanisms that determine the performance of the energy harvester, the dependence of the performance on various design parameters and the microscopic behavior of the ferrofluid, it is necessary to develop computational models and analysis tools of the system that are able to efficiently and accurately describe the physical behavior of the system and accelerate the design and optimization of the device. To achieve this goal, we investigate these relations through detailed computational analysis at several different levels:

- **Develop a continuum level finite element model for fully coupled computational**

analysis which alleviates some assumptions made in the analytical model of Ref. [30]. This computational model solves the coupled magnetic scalar potential equation and Navier-Stokes equations for the dynamic behavior of the magnetic field and free surface fluid motion [44].

- **Conduct experiments to validate the continuum level computational model.** The experiments are based on the design of Ref. [29] with modifications to accommodate the assumptions of the computational model. The model is validated against the experimental results for eight configurations of the system [44].

- **Employ the validated model to study the underlying mechanisms of ferrofluid based energy harvesting and test the effects of several modeling aspects.** A better understanding of the energy conversion mechanisms of the energy harvester is obtained through the computational analysis. Furthermore, computational analysis is performed to test the effects of several modeling aspects, such as the three-dimensional effect, surface tension and type of the ferrofluid-magnetic field coupling, on the accuracy of the model prediction [44].

- **Perform a parametric study to investigate the influence of several design parameters on the output electromotive force.** Two configurations of the energy harvester that give the highest electromotive forces are considered for performance analysis. The design parameters considered in this investigation include the device's geometric parameters, external excitation amplitude and material properties of the ferrofluid, which affect either the magnetic flux in the device or the sloshing behavior of the ferrofluid [45].

- **Perform non-equilibrium molecular dynamics (NEMD) simulations to capture the dynamic magnetization of the ferromagnetic nano-particles and microscopic**

structures of the ferrofluid. As the ferrofluid in the energy harvester undergoes sloshing motion under external mechanical excitations, it is also expected that the fluid motion would significantly alter the aggregation behavior of the nano-particles, thereby affecting the effective magnetization of the ferrofluid and the performance of the energy harvester. Therefore, a systematic molecular level study on ferrofluid systems containing both small and large particles under the influence of both magnetic field and shear flow is carried out. The computational model involves long-range dipolar interaction as well as short-range repulsive interaction of the nano-particles. The factors investigated include solvent friction coefficients, particle size, magnetic field strength and direction, and shear rate.

1.5 Dissertation Outline

The rest of the dissertation is organized as follows. Chapter 2 covers the first 3 objectives of the dissertation, presenting a magneto-ferro-hydrodynamic finite element model along with experimental validation and computational analysis. Chapter 3 presents the parametric study and performance analysis of the energy harvester, which is the fourth objective. Chapter 4 presents the molecular dynamics simulations and analysis on the dynamic magnetization and microscopic behavior of the ferrofluid, which is the fifth objective. Finally, Chapter 5 presents the conclusions of this dissertation.

Chapter 2

Continuum Level Modeling and Implementation

In the literature, continuum level computational models have been developed for studying ferrofluids in various applications (e.g. normal-field instability [46], spin-up flow [47, 48], ferrofluid pump [49], magnetic drug targeting [50], interfacial deformation and jetting [51], ferrofluid droplet or rising bubble in ferrofluid [52–55], sloshing [56], etc.). Recently, Kim [32] carried out a numerical analysis on a different ferrofluid based energy harvester. However, some of these models are for applications without ferrofluid-gas interface [47–50] or with a uniform magnetic field [46, 52, 53], and some are overly-simplified by using wedge-shaped ferrofluid sloshing motion [32], or invariant magnetic field [54, 56]. Refs. [51, 55] solved the magnetic field with analytical or measured magnetic scalar potential boundary condition generated by permanent magnets, but did not incorporate magnets explicitly in the model. While fulfilling their own purposes, such models are insufficient for computational analysis of our energy harvester.

As such, in this chapter, we present a comprehensive finite element (FE) model for fully coupled computational analysis of a ferrofluid based energy harvester. Note that while

the model is developed for the ferrofluid based energy harvester, it is a general purpose model which can be applied to simulate any system containing free surface ferrofluid flow under the influence of an externally applied magnetic field.

This model solves the coupled magnetic scalar potential equation and Navier-Stokes equations for the dynamic behavior of the magnetic field and fluid motion. The Volume of Fluid (VOF) method is employed to track the liquid-gas interface. The sharp surface tension force model (SSF) is employed along with the height function method to capture the influence of surface tension. The computational model is validated against experimental results for various configurations of the system. The validated model is then employed to study the underlying mechanisms that determine the electromotive force of the energy harvester. Furthermore, computational analysis is performed to test the effect of several modeling aspects, such as three-dimensional effect, surface tension and type of the ferrofluid-magnetic field coupling, on the accuracy of the model prediction.

2.1 Experimental Setup

The experimental setup follows the work of Alazemi et al. [29, 30] as shown in Fig. 2.1a. The setup consists of a $12.7\times12.7\times12.7$ cm^3 cubic plastic tank filled with 2.5 cm deep ferrofluid EFH3 (Ferrotec Corp.) and placed inside a copper coil of 1000 turns. The ferrofluid EFH3 has a density of 1420 kg/m^3, a viscosity of 12 mPa·s, and an initial magnetic susceptibility of 3.52. The surface tension coefficient of the light hydrocarbon carrier fluid is 24.15 mN/m [47]. Unlike the device used in Refs. [29, 30], in the current setup, the ferromagnetic core is discarded to eliminate its interference with the magnetic field. The copper coil is wound directly around the plastic tank. Two bar-shaped permanent magnets with dimensions of $30.48\times2.45\times1.27$ cm^3 and a remanent magnetic flux density of 0.38 T are placed at a distance of 4 cm from the nearest tank inner wall with their

longitudinal axes directed perpendicular to the plane of sloshing. As shown in Fig. 2.1b, we consider four configurations of the energy harvester. The magnets are placed on either side of the tank in the first two configurations, with their centers 2.5 cm above the ferrofluid surface, and are placed above and under the tank in the other configurations. The north poles of the magnets are aligned in the same direction in Configs. (1) and (3), whereas facing each other in Configs. (2) and (4). For all 4 configurations, both horizontal and vertical coil windings are tested and denoted as "H" and "V", respectively. The tank and magnets are fixed on a thick plastic plate supported by four plastic pillars. The plastic pillars are erected to create sufficient distance between the tank and the shaker's mounting table, thereby serving to minimize eddy currents.

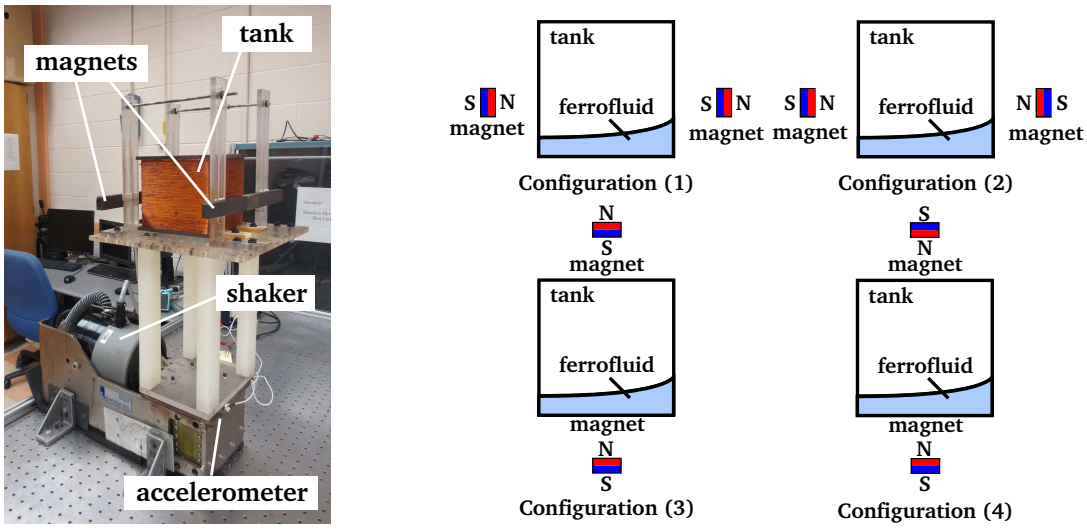

Figure 2.1: (a) Experimental setup. (b) Schematic diagrams showing the 4 configurations of the ferrofluid based energy harvester.

As shown in Fig. 2.1a, the setup is fixed on a mounting table connected to an electrodynamic shaker (Model ET-140, Labworks Inc.), which provides an external harmonic excitation to the tank. The acceleration of the tank is measured using an accelerometer. A dSPACE ControlDesk system (dSPACE Inc.) is used to compare the experimental tank ac-

celeration amplitude with the prescribed value 0.5 m/s^2 and adjust the output excitation of the shaker accordingly. The resulting electromotive force is also measured by the dSPACE system from the copper coil. When the experiment starts at a certain base excitation frequency, the sloshing dynamics and the resulting electromotive force go through a transient stage and eventually reach their steady-state values after a sufficiently long time. The root-mean-square (RMS) electromotive force value is then computed for each frequency, as explained in Sec. 2.2.1.1. Variation of the electromotive force with the base excitation frequency is then obtained using a quasi-static frequency sweep containing the first modal frequency.

2.2 Continuum Level Modeling and Implementation

2.2.1 Governing equations

Several assumptions are adopted in modeling the coupled magneto-ferro-hydrodynamic system depicted in Fig. 2.1a. First, in the experimental setup, the sloshing motion of the fluid is mainly two-dimensional. The sloshing plane is defined as the xy plane and the direction perpendicular to the sloshing plane as the z direction. Since the bar magnets have a much larger dimension in the z direction than their cross-sectional dimensions, the magnetic flux density distribution is considered to be uniform along the z direction. Thus, the ferrofluid based electromagnetic energy harvester is represented by the two-dimensional (2-D) system shown in Fig. 2.2. Second, as described further in Sec. 2.2.1.1, the ferrofluid is considered to be superparamagnetic and magnetization of the ferrofluid is linearly proportional to the magnetic field before reaches its saturation value. Third, the ferrofluid is considered to be an incompressible viscous fluid with non-negligible surface tension. The governing equations of the magneto-ferro-hydrodynamic system are described next.

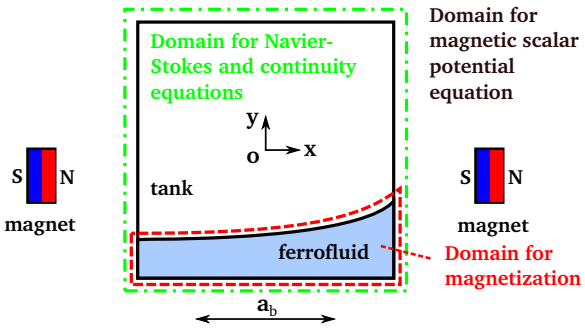

Figure 2.2: Schematic diagram showing the computational domains for different governing equations. The entire spatial domain, which is set to be 10 times the size of the tank and magnets, is governed by the magnetic scalar potential equation. The domain enclosed by red dashed lines is subject to magnetization. The domain inside the tank (enclosed by green dash-dot lines) is governed by the Navier-Stokes and continuity equations.

2.2.1.1 Magnetic scalar potential equation for magnetic analysis

In the external magnetic field applied by the magnets, the sloshing of the ferrofluid creates a time-varying magnetization in the fluid, producing a time-varying magnetic field and electric field. We compute the electromotive force induced by the time-varying magnetic field assuming open-circuit conditions. This, combined with the fact that both the ferrofluid and air are non-conducting fluids, guarantees that there is no electric current passing through the system. With no electric current and the low operating frequencies of the energy harvester (1-7 Hz), the magnetic field induced by the electric field is negligible. Under such conditions, Maxwell's equations for magnetodynamics are given as [57]

$$\nabla \cdot \mathbf{B} = 0 \tag{2.1}$$

$$\nabla \times \mathbf{H} = \mathbf{0} \tag{2.2}$$

$$\nabla \times \mathbf{E} = -\frac{\partial \mathbf{B}}{\partial t} \tag{2.3}$$

where $\mathbf{B}$ is the magnetic flux density, $\mathbf{H}$ the magnetic field, $\mathbf{E}$ the electric field, and t the time. Note that, since the curl of $\mathbf{H}$ is zero, $\mathbf{H}$ can be expressed as the gradient of the

magnetic scalar potential ψ as

$$\mathbf{H} = -\nabla\psi. \tag{2.4}$$

The constitutive equations are given by

$$\mathbf{B} = \mu_0\mathbf{H} \qquad \text{in the air} \tag{2.5}$$

$$\mathbf{B} = \mu_0(\mathbf{H} + \mathbf{M}) \qquad \text{in the ferrofluid} \tag{2.6}$$

$$\mathbf{B} = \mu_0\mathbf{H} + \mathbf{B}_0 \qquad \text{in the magnets} \tag{2.7}$$

where $\mathbf{M}$ is the magnetization, $\mathbf{B}_0$ the remanent magnetic flux density, and μ_0 the permeability of free space. Equation (2.7) is a good approximation for commonly used permanent magnets, such as ferrite, Samarium-Cobalt, and Neodymium-Iron-Boron magnets, the differential permeabilities of which are very close to μ_0 [57].

When the external $\mathbf{H}$ is applied, a ferrofluid particle aligns its magnetic moment with the field either by a rotation of the whole particle, a process called Brownian relaxation, or by a change of the direction of the magnetic moment inside the particle, the so-called Néel relaxation [58]. Both relaxation processes are characterized by respective relaxation times τ_B and τ_N that produce a phase-delay between $\mathbf{H}$ and $\mathbf{M}$. When $\tau_N \gg \tau_B$, the magnetization and rotation of magnetic particles follow the magnetization relaxation equation and spin equation [58]. However, since in this work, the order of relaxation time (microseconds) is much lower than the period of fluid oscillation (seconds), the ferrofluid sample can be regarded as superparamagnetic. In such a case, when the magnitude of $\mathbf{H}$ increases over a threshold value, all the magnetic particles align with direction of $\mathbf{H}$ and magnetization reaches its saturation value. On the other hand, when $\mathbf{H}$ is small, the following linear relation exists between $\mathbf{M}$ and $\mathbf{H}$:

$$\mathbf{M} = \chi\mathbf{H} \tag{2.8}$$

where χ is the magnetic susceptibility.

Combining Eqs. (2.1, 2.4-2.8), we obtain a single set of governing equation in terms of ψ

$$\nabla \cdot \left[(1+\chi)\nabla\psi - \frac{1}{\mu_0}\mathbf{B}_0 \right] = 0 \tag{2.9}$$

where the values of χ and $\mathbf{B}_0$ vary sharply at the interface between ferrofluid and air, magnets and air, respectively. In this way, the continuity of tangential component of $\mathbf{H}$ and normal component of $\mathbf{B}$ is satisfied automatically. The boundary conditions for the entire computational domain are

$$\frac{\partial\psi}{\partial\mathbf{n}} = \mathbf{0} \qquad \text{on the boundary of the entire computational domain} \tag{2.10}$$

$$\psi = 0 \qquad \text{at the center of the top boundary} \tag{2.11}$$

where $\mathbf{n}$ is the outward unit normal vector of the boundary. While the physical domain of the magnetic field is infinitely large, the computational domain must be limited to a finite size. To determine the proper size of the computational domain, domain sizes that are 5, 8, 10, 15 and 20 times as large as the rectangular space occupied by the tank and magnets are used to calculate ψ. It is found that the result has converged for the 10-time-large domain. The norm difference in ψ between the 10-time-large and 20-time-large domains is within 1.5%. Thus the 10-time-large domain is taken to be the computational domain for all subsequent calculations.

In the dynamic computational analysis, the time-varying magnetic scalar potential ψ is computed by solving Eq. (2.9) at each time step of the ferrofluid motion. Once ψ in the entire domain and the magnetization $\mathbf{M}$ in the ferrofluid are obtained at each time step, the electromotive force can be obtained using the integral form of Eq. (2.3), i.e. Faraday's

law of induction in this work. For one turn of coil [57],

$$\varepsilon = -\frac{d\Phi_B}{dt} \tag{2.12}$$

where ε is the electromotive force, Φ_B the magnetic flux. Both horizontal and vertical coil windings are considered. For N_{turns} horizontal turns of coil uniformly wound around the tank, ε is obtained from Eq. (2.12) as

$$\varepsilon = -\frac{d}{dt}\left[\frac{N_{turns}}{H_t}\int_{-H_t/2}^{H_t/2}\left(\int_{-W_t/2}^{W_t/2}\int_{-L_t/2}^{L_t/2} B_y dxdz\right)dy\right] = -\frac{N_{turns}W_t}{H_t}\frac{d}{dt}\left(\int_{\Omega_t} B_y d\Omega\right) \tag{2.13}$$

where L_t, H_t, and W_t are the length, height, and width of the tank, respectively. Ω_t is the 2-D domain in the xy plane inside the tank, and B_y the y-component of $\mathbf{B}$. Using the central difference scheme for the time derivative, ε at a time step $t^{n+1/2}$ is calculated as

$$\varepsilon^{n+1/2} \approx -\frac{N_{turns}W_t}{H_t(t^{n+1}-t^n)}\left[\left(\int_{\Omega_t} B_y d\Omega\right)^{n+1} - \left(\int_{\Omega_t} B_y d\Omega\right)^{n}\right] \tag{2.14}$$

and

$$\int_{\Omega_t} B_y d\Omega = \mu_0 \int_{\Omega_t} (H_y + M_y)\, d\Omega = \mu_0 \int_{-L_t/2}^{L_t/2} (\psi_{-H_t/2} - \psi_{H_t/2}) dx + \mu_0 \int_{\Omega_t} M_y d\Omega \tag{2.15}$$

where H_y and M_y are the y-component of $\mathbf{H}$ and $\mathbf{M}$, respectively.

For N_{turns} vertical uniform turns, ε is calculated by

$$\varepsilon^{n+1/2} \approx -\frac{N_{turns}W_t}{L_t(t^{n+1}-t^n)}\left[\left(\int_{\Omega_t} B_x d\Omega\right)^{n+1} - \left(\int_{\Omega_t} B_x d\Omega\right)^{n}\right] \tag{2.16}$$

with

$$\int_{\Omega_t} B_x d\Omega = \mu_0 \int_{-H_t/2}^{H_t/2} (\psi_{-L_t/2} - \psi_{L_t/2}) dy + \mu_0 \int_{\Omega_t} M_x d\Omega \tag{2.17}$$

where H_x and M_x are the x-component of $\mathbf{H}$ and $\mathbf{M}$, respectively.

After the system reaches the steady state, the root-mean-square (RMS) value of electromotive force at each excitation angular frequency ω is calculated by

$$\varepsilon^{rms}(\omega) = \sqrt{\frac{1}{t^{N_2} - t^{N_1}} \sum_{n=N_1}^{N_2-1} [(\varepsilon^{n+1/2})^2 (t^{n+1} - t^n)]} \tag{2.18}$$

where N_1 and N_2 are the start and end time step index of the sample region for RMS value calculation, respectively. For each frequency, the sample region is different. N_1 and N_2 satisfy

$$t^{N_1} = \frac{2\pi N_{cycle1}}{\omega}, \qquad t^{N_2} = \frac{2\pi N_{cycle2}}{\omega} \tag{2.19}$$

where N_{cycle1} and N_{cycle2} are the start and end excitation cycle index of the sample region, respectively. N_{cycle1} and N_{cycle2} are taken as 3 and 12 for all simulations, respectively. For experiments, 10 excitation cycles are used for the sample region following the initial fixed $t^{N_1} = 20$ seconds. In all the following sections, the rms superscript on ε is omitted for simplicity.

2.2.1.2 Navier-Stokes equations for fluid dynamics in the tank

Both the ferrofluid and air in the tank are described by the Navier-Stokes and continuity equations for incompressible flow [58, 59]. These are:

$$\rho \left(\frac{\partial \mathbf{V}}{\partial t} + \mathbf{V} \cdot \nabla \mathbf{V} \right) = -\nabla P + \nabla \cdot \eta [\nabla \mathbf{V} + (\nabla \mathbf{V})^T] + \mu_0 \mathbf{M} \cdot \nabla \mathbf{H} - \rho \mathbf{g} + \mathbf{f}_b - \sigma \kappa \nabla H(f) \tag{2.20}$$

$$\nabla \cdot \mathbf{V} = 0 \tag{2.21}$$

where $\mathbf{V}$ is the velocity, P the pressure, ρ the density, η the shear viscosity, and $\mathbf{g}$ the gravitational acceleration. Here, ρ and η are constant in each phase but jump at the liquid-gas interface. The term $\mu_0 \mathbf{M} \cdot \nabla \mathbf{H}$ is the magnetic body force due to magnetization of the ferrofluid. The term $-\sigma\kappa\nabla H(f)$ is the surface tension force applied on the liquid-gas interface, where σ is the surface tension coefficient, κ the local curvature, f the volume fraction taken by the liquid, and $H(f)$ a Heaviside step function of f. Assuming the base excitation acceleration $\mathbf{a}_b$ is a harmonic function given by $\mathbf{a}_b = -\mathbf{a}_0 \cos(\omega t)$, the inertial force $\mathbf{f}_b$ on the fluid due to the external base excitation can be written as

$$\mathbf{f}_b = -\rho \mathbf{a}_b = \rho \mathbf{a}_0 \cos(\omega t) \tag{2.22}$$

where $\mathbf{a}_0$ is the amplitude of the base acceleration and ω is its angular frequency. Finally, the boundary conditions on Eqs. (2.20, 2.21) are given by

$$\mathbf{V} = \mathbf{0} \qquad \text{on the boundary of the tank} \tag{2.23}$$

$$P = 0 \qquad \text{at the center of the tank top edge.} \tag{2.24}$$

2.2.2 Finite element formulation and implementation

Having defined all the governing equations necessary to model the dynamics of the system, a finite element (FE) model is formulated and implemented in our in-house code written in C++. In the FE model, the magnetic field distribution is obtained by solving the magnetic scalar potential equation using the Galerkin method. The velocity field of the fluid is obtained by solving the Navier-Stokes and continuity equations using the streamline-upwind/Petrov-Galerkin (SUPG) and pressure-stabilizing/Petrov-Galerkin (PSPG) methods. The Volume of Fluid (VOF) method is employed to track the liquid-gas interface. The sharp surface tension force model (SSF) is employed along with the height

function method to capture the influence of surface tension. This section contains the details of the formulation and implementation of the FE model. The FE model results in a system of algebraic equations. Approximate values of the unknowns can be calculated at finite number of discrete points over the computational domain.

2.2.2.1 Magnetic field

The Galerkin Method of Weighted Residuals [60] is applied to obtain the weak form of the magnetic scalar potential equation. Multiplying Eq. (2.9) by the variation of ψ, i.e. $\delta\psi$, and integrating it in the entire domain give

$$\int_{\Omega} \delta\psi \nabla \cdot \left[(1+\chi)\nabla\psi - \frac{1}{\mu_0}\mathbf{B}_0 \right] d\Omega = 0 \tag{2.25}$$

Separating the air, liquid and magnet regions of the domain, and applying the Green's formula, Eq. (2.25) can be rewritten as

$$\int_{\Omega} \nabla\delta\psi \cdot \nabla\psi d\Omega + \int_{\Omega_{liq}} \nabla\delta\psi \cdot \chi\nabla\psi d\Omega - \int_{\Omega_{mag}} \nabla\delta\psi \cdot \frac{1}{\mu_0}\mathbf{B}_0 d\Omega - \int_{\Gamma} \delta\psi \frac{\partial\psi}{\partial\mathbf{n}} d\Gamma = 0 \tag{2.26}$$

where Ω is the entire domain of magnetics, Ω_{liq} the domain of elements containing ferrofluid, Ω_{mag} the domain of magnets, and Γ the boundary of the entire domain. Equation (2.26) is the weak form of the governing equation. The domain of magnetodynamics is then divided into a mesh of quadratic quadrilateral elements. Note that, χ is discontinuous across the liquid-gas interface ($\chi = 0$ in the air). Since the liquid-gas interface moves constantly during sloshing, typically, the elements that intersect the liquid-gas interface are partially filled with ferrofluid. For these elements, the second term given in Eq. (2.26) should be rewritten as the integral of an averaged value $\bar{\chi}$, i.e. $\int_{\Omega^e_{interface}} \nabla\delta\psi \cdot \bar{\chi}\nabla\psi d\Omega$, where $\Omega^e_{interface}$ denotes a transition element e at the liquid-gas interface. To calculate

$\bar{\chi}$ for the transition elements, two interpolation schemes, namely the weighted arithmetic mean interpolation (WAM) and weighted harmonic mean interpolation (WHM) schemes, are investigated. The WAM and WHM interpolation schemes were used to interpolate dielectric permittivity of different dielectric fluids over their interface [61]. Using WAM, the effective permeability in the transition element is obtained as

$$\bar{\mu} = \mu_1 f + \mu_2(1 - f) \tag{2.27}$$

and using WHM,

$$\frac{1}{\bar{\mu}} = \frac{f}{\mu_1} + \frac{1 - f}{\mu_2} \tag{2.28}$$

where the subscripts 1 and 2 represent ferrofluid and air, respectively, and f is the volume fraction of ferrofluid in the transition element. Note that, in the dynamic analysis, the liquid-gas interface is tracked and f is computed for the transition elements by using the Volume of Fluid method which is described in details in Sec. 2.2.2.3. The numerical performances of the two interpolation schemes are tested in the current ferrofluid energy harvester model. It is found that WHM gives better agreement between computed electromotive forces and experimental results. Similar finding is also described in Ref. [61]. Therefore, WHM is adopted for the calculation of $\bar{\chi}$. Substituting $\bar{\mu} = \mu_0(1 + \bar{\chi})$, $\mu_1 = \mu_0(1 + \chi_1)$, and $\mu_2 = \mu_0$ into Eq. (2.28) gives

$$\bar{\chi} = \frac{f\chi_1}{1 + (1 - f)\chi_1} \tag{2.29}$$

Solving Eq. (2.26) with (2.29) for ψ requires approximation of the unknown quantities within each element using the Lagrange interpolation

$$\psi(x, y) = \sum_{k=1}^{n_{en}} N_k(x, y)\psi_k \tag{2.30}$$

where n_{en} is the number of nodes in an element, $N_k(x, y)$ is the shape function associated with node k in the element, and ψ_k is the value of ψ at node k. For quadratic elements, nodes are on the vertices and edges of the elements. The partial derivatives of ψ are expressed as

$$\frac{\partial \psi(x,y)}{\partial x} = \sum_{k=1}^{n_{en}} \frac{\partial N_k(x,y)}{\partial x}\psi_k, \qquad \frac{\partial \psi(x,y)}{\partial y} = \sum_{k=1}^{n_{en}} \frac{\partial N_k(x,y)}{\partial y}\psi_k \tag{2.31}$$

As the same Lagrange interpolation is used for $\delta\psi$, the weighting function $\delta\psi$ in the weak form can be equivalently expressed using the shape functions of the elements. For each element, the integrals in Eq. (2.26) are then evaluated using numerical integration and expressed in the form of discretized element equations in terms of the unknown nodal ψ_k, $k = 1, 2, ..., n_{en}$. The global system, which is a linear system of algebraic equations in this case, can be obtained by assembling all the element equations as

$$\mathbf{K}\boldsymbol{\psi} = \mathbf{f} \tag{2.32}$$

where $\boldsymbol{\psi}$ is the global vector of the unknown nodal ψ at all nodes. The matrix $\mathbf{K}$ is obtained from the first and second integrals in Eq. (2.26), whereas $\mathbf{f}$ from the third integral and the natural boundary condition. After applying the essential boundary condition Eq. (2.11), the linear system can be solved and all the unknown nodal ψ can be obtained.

$\boldsymbol{\psi}$ obtained from the solution of Eq. (2.32) can only result in averaged or smeared value $\bar{\mathbf{H}}$ in the transition elements. However, $\mathbf{H}_1$ and $\mathbf{M}_1$ are required in the transition elements for electromotive force and magnetic body force calculation. Since $\mathbf{M}_2 = \mathbf{0}$, and $\bar{\mathbf{M}} = f\mathbf{M}_1 + (1-f)\mathbf{M}_2 = f\mathbf{M}_1$, we obtain

$$\mathbf{M}_1 = \frac{\bar{\mathbf{M}}}{f} = \frac{\chi_1}{1 + (1-f)\chi_1}\bar{\mathbf{H}} \tag{2.33}$$

Also from $\mathbf{M}_1 = \chi_1 \mathbf{H}_1$, we have

$$\mathbf{H}_1 = \frac{\mathbf{M}_1}{\chi_1} = \frac{1}{1 + (1-f)\chi_1} \bar{\mathbf{H}} \tag{2.34}$$

2.2.2.2 Sloshing dynamics

We obtain the weak form of the Navier-Stokes equations and continuity equation by using the streamline-upwind/Petrov-Galerkin (SUPG) and pressure-stabilizing/Petrov-Galerkin (PSPG) methods as [62]

$$\begin{aligned} &\int_\Omega \mathbf{w} \cdot \left[\rho \left(\frac{\partial \mathbf{V}}{\partial t} + \mathbf{V} \cdot \nabla \mathbf{V} \right) - \mathbf{f} \right] d\Omega + \int_\Omega \boldsymbol{\epsilon}(\mathbf{w}) : \mathbf{T} d\Omega + \int_\Omega q \nabla \cdot \mathbf{V} d\Omega \\ &+ \sum_{e=1}^{n_e} \int_{\Omega^e} \left(\tau_{SUPG} \mathbf{V} \cdot \nabla \mathbf{w} + \tau_{PSPG} \frac{1}{\rho} \nabla q \right) \cdot \left[\rho \left(\frac{\partial \mathbf{V}}{\partial t} + \mathbf{V} \cdot \nabla \mathbf{V} \right) - \nabla \cdot \mathbf{T} - \mathbf{f} \right] d\Omega \\ &+ \sum_{e=1}^{n_e} \int_{\Omega^e} \tau_{LSIC} \nabla \cdot \mathbf{w} \rho \nabla \cdot \mathbf{V} d\Omega = \int_\Gamma \mathbf{w} \cdot \mathbf{t} d\Gamma \end{aligned} \tag{2.35}$$

where

$$\mathbf{T} = -P\mathbf{I} + \eta[\nabla \mathbf{V} + (\nabla \mathbf{V})^T] \tag{2.36}$$

$$\mathbf{f} = \mu_0 \mathbf{M} \cdot \nabla \mathbf{H} - \rho \mathbf{g} + \rho \mathbf{a_0} \cos(\omega t) - \sigma \kappa \nabla H(f) \tag{2.37}$$

$\mathbf{w}$ and q denote weighting functions for velocity $\mathbf{V}$ and pressure P, respectively. Other variables include $\mathbf{T}$-stress tensor, $\boldsymbol{\epsilon}$-strain tensor, $\mathbf{f}$-body force, $\mathbf{t}$-surface traction on the boundary, τ_{SUPG}-SUPG stabilization parameter, τ_{PSPG}-PSPG stabilization parameter, and τ_{LSIC}-least-squares on incompressibility constant (LSIC) stabilization parameter. The av-

eraged ferrofluid density and viscosity in transition elements are defined as

$$\bar{\rho} = f\rho_1 + (1-f)\rho_2 \tag{2.38}$$

$$\bar{\eta} = f\eta_1 + (1-f)\eta_2 \tag{2.39}$$

The two element-level integrals in the formulation are the SUPG+PSPG stabilization terms for the momentum equation and least-squares stabilization term for the continuity equation, respectively. The coefficients are given as [62]

$$\tau_{SUPG} = \left[\left(\frac{2}{\Delta t} \right)^2 + \left(\frac{2|\mathbf{V}|}{h_e} \right)^2 + \left(\frac{4\nu}{h_e^2} \right)^2 \right]^{-\frac{1}{2}} \tag{2.40}$$

$$\tau_{PSPG} = \tau_{SUPG} \tag{2.41}$$

$$\tau_{LSIC} = \frac{h_e}{2}|\mathbf{V}|z(Re_e) \tag{2.42}$$

where ν-kinematic viscosity, h_e-element length, Re_e-element Reynolds number. h_e and Re_e are defined as

$$h_e = 2|\mathbf{V}| \left(\sum_{k=1}^{n_{en}} |\mathbf{V} \cdot \nabla N_k| \right)^{-1} \tag{2.43}$$

$$Re_e = \frac{|\mathbf{V}|h_e}{2\nu} \tag{2.44}$$

The function $z(Re_e)$ is defined as

$$z(Re_e) = \begin{cases} Re_e/3, & Re_e \leq 3 \\ 1, & Re_e > 3 \end{cases} \tag{2.45}$$

The finite element discretization of the weak form of the Navier-Stokes equations follows a similar procedure as described for the magnetic analysis. Linear elements are

used to solve the Navier-Stokes and continuity equations. The quadratic elements inside the tank for magnetic analysis are converted to linear elements for sloshing dynamics analysis by taking only the vertices (neglecting the edge nodes). In this way, the magnetic and sloshing dynamics analyses share the same mesh in the tank. After the standard FE discretization, the weak form can be rewritten in a matrix form similar to that obtained in Ref. [63]:

$$(\mathbf{M}+\mathbf{M}_s)\mathbf{a}+[\mathbf{C}(\mathbf{v})+\mathbf{C}_s(\mathbf{v})]\mathbf{v}+(\mathbf{D}-\mathbf{D}_s+\mathbf{B}_c)\mathbf{v}-[\mathbf{G}-\mathbf{G}_s]\mathbf{p}=\mathbf{f}+\mathbf{f}_s \quad (2.46)$$

$$\mathbf{G}^T\mathbf{v}+\mathbf{M}_p\mathbf{a}+\mathbf{C}_p(\mathbf{v})\mathbf{v}-\mathbf{D}_p\mathbf{v}+\mathbf{G}_p\mathbf{p}=\mathbf{f}_p \quad (2.47)$$

where $\mathbf{v}$, $\mathbf{a}$ and $\mathbf{p}$ are the vectors of unknown nodal values of velocity, acceleration and pressure, respectively. The matrices $\mathbf{M}$, $\mathbf{C}(\mathbf{v})$, $\mathbf{D}$ and $\mathbf{G}$ are derived from mass, convective, viscous and pressure terms, respectively. $\mathbf{f}$ is related to the body forces and natural boundary conditions. The subscripts s and p represent terms derived from SUPG stabilization terms and PSPG stabilization terms, respectively. $\mathbf{B}_c$ is obtained from the least-squares stabilization term.

In the dynamic analysis, the predictor-corrector algorithm is used to solve for unknown variables at time t_{n+1} from t_n [64]. The first step is to calculate the predicted values $\mathbf{v}_{n+1}^{(0)}$, $\mathbf{p}_{n+1}^{(0)}$ using values from t_n and set $\mathbf{a}_{n+1}^{(0)}$, $\dot{\mathbf{p}}_{n+1}^{(0)}$ zero. At the $(i+1)$th iteration, the weak form is written in an incremental form and $\Delta\mathbf{a}^{(i)}$ and $\Delta\mathbf{p}^{(i)}$ are calculated. When $\Delta\mathbf{a}^{(i)}$, $\Delta\mathbf{p}^{(i)}$ are obtained, predicted values are updated accordingly. Since the acceleration is zero at the first iteration, at least 2 iterations are required to take into consideration the effect of mass matrix.

2.2.2.3 Liquid-gas interface model

The Volume of Fluid (VOF) method [65] is used to capture the liquid-gas interface. A fixed mesh system is adopted so that no re-meshing is required. The fluids on either side of the interface are marked by volume fraction f (or fractional volume, color function). The VOF method is based on a transport equation of f

$$\frac{\partial f}{\partial t} + \mathbf{V} \cdot \nabla f = 0 \tag{2.48}$$

where f is defined such that it is 1 at any point occupied by liquid and 0 elsewhere. If the flow field is incompressible, i.e. $\nabla \cdot \mathbf{V} = 0$, Eq. (2.48) can be rewritten as

$$\frac{\partial f}{\partial t} + \nabla \cdot (\mathbf{V} f) = 0 \tag{2.49}$$

While ∇f is physically singular across the moving boundary, it becomes finite in the numerical solution. The phenomenon is known as "false numerical diffusion". One of the schemes to suppress the numerical smearing is the volume flux based scheme. Integration of the transport equation and discretization by an explicit scheme give [66]

$$f_{i,j}^{n+1} = f_{i,j}^{n} + \frac{\Delta t}{\Delta x}(F_{i-1/2,j}^{n} - F_{i+1/2,j}^{n}) + \frac{\Delta t}{\Delta y}(G_{i,j-1/2}^{n} - G_{i,j+1/2}^{n}) \tag{2.50}$$

where i and j denote the column and row indices of an element, respectively. $F_{i-1/2,j} = (fu)_{i-1/2,j}$ denotes the flux across the left edge of element (i, j) and $G_{i,j-1/2} = (fv)_{i,j-1/2}$ the flux across the bottom edge, etc. The geometric interpretation of fluxes is shown in Fig. 2.3. The averaged value of f would then represent the fractional volume taken by liquid in one element.

The simplest way to determine the interface position in an element is the simple

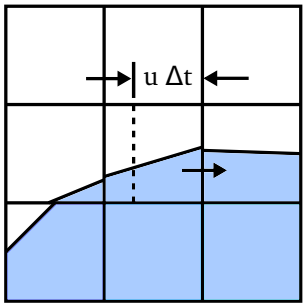

Figure 2.3: The liquid to the right of the dotted line crosses the right element edge. In VOF/PLIC, the outflow volume can be determined after the interface is reconstructed.

line interface calculation (SLIC) [65]. A more accurate method is to construct the interface with piecewise linear segments by using the interface normal direction and the value of f. The method is known as the piecewise linear interface calculation (PLIC) method [66–70]. In the method, the normal vector of the interface $\mathbf{m}$ is estimated by

$$\mathbf{m} = \nabla f \tag{2.51}$$

In numerical implementation, taking a 3×3 block centered at element (i, j), $\mathbf{m}_{i,j}$ is computed through averaging the values of $\mathbf{m}$ at the corners of element (i, j). For example at position $(i + 1/2, j + 1/2)$, which is the top right corner of element (i, j), we use the following formulae similar to Ref. [71]

$$m_{x,i+1/2,j+1/2} = \frac{(f_{i+1,j} - f_{i,j})\Delta y_j + (f_{i+1,j+1} - f_{i,j+1})\Delta y_{j+1}}{2\Delta y_{j+1/2}\Delta x_{i+1/2}} \tag{2.52}$$

$$m_{y,i+1/2,j+1/2} = \frac{(f_{i,j+1} - f_{i,j})\Delta x_i + (f_{i+1,j+1} - f_{i+1,j})\Delta x_{i+1}}{2\Delta x_{i+1/2}\Delta y_{j+1/2}} \tag{2.53}$$

where Δx_i and Δy_j are the length and width of element (i, j). $\Delta x_{i+1/2}$ and $\Delta y_{j+1/2}$ are defined as $\Delta x_{i+1/2} = \frac{1}{2}(\Delta x_i + \Delta x_{i+1})$ and $\Delta y_{j+1/2} = \frac{1}{2}(\Delta y_j + \Delta y_{j+1})$. The required

element-centered value is the average of vertex values

$$\mathbf{m}_{i,j} = \frac{1}{4}(\mathbf{m}_{i+1/2,j+1/2} + \mathbf{m}_{i+1/2,j-1/2} + \mathbf{m}_{i-1/2,j+1/2} + \mathbf{m}_{i-1/2,j-1/2}) \tag{2.54}$$

When the element (i, j) is at the boundary or corner, a 2×3, 3×2 or 2×2 block is used depending on the element location.

When the interface normal vector $\mathbf{m}$ and volume fraction f are known, the position of the linear interface segment inside every transition element can be found [68]. We first rotate the coordinate system in each transition element to make the normal vector $\mathbf{m}$ point to the right or top right direction as in Fig. 2.4.

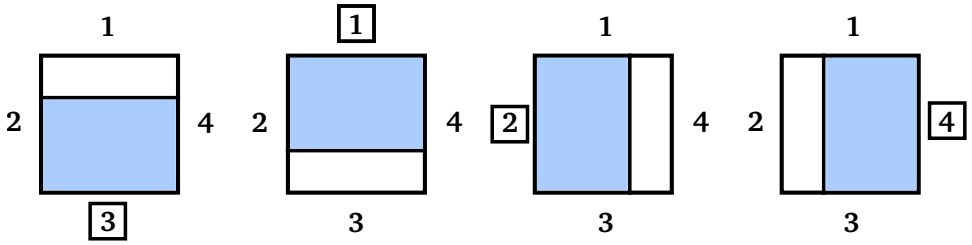

(a)

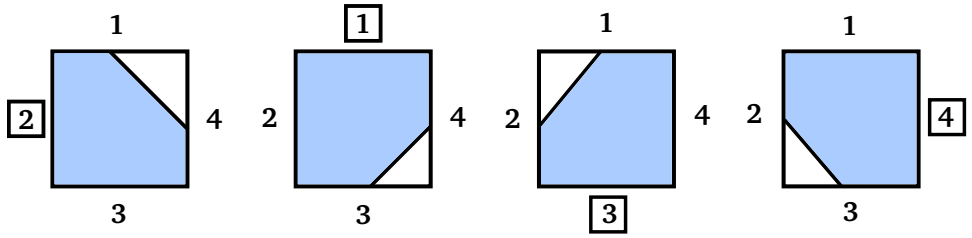

(b)

Figure 2.4: Elements to be rotated in order to have the interface normal vector $\mathbf{m}$ pointing to the (a) right direction or (b) top right direction. The numbers put in the squares demonstrate the new start edge of the elements. The new elements have the 1st edge on the left.

The cases in Fig. 2.4a are trivial. The interface position for the cases in Fig. 2.4b can be obtained as follows. Figure 2.5 shows a rectangular element having an interface line with a normal vector $\mathbf{m}$. Assuming the components of $\mathbf{m}$, m_x and m_y, are both positive

after the coordinate transformation, a general equation for the straight interface line is

$$m_x x + m_y y = \alpha_m \tag{2.55}$$

where α_m is related to the distance between the line and the origin. The liquid area below the interface line within the rectangular element can be written as

$$S = \frac{\alpha_m^2}{2m_x m_y}\left[1 - H(\alpha_m - m_x\Delta x)\left(\frac{\alpha_m - m_x\Delta x}{\alpha_m}\right)^2 - H(\alpha_m - m_y\Delta y)\left(\frac{\alpha_m - m_y\Delta y}{\alpha_m}\right)^2\right] \tag{2.56}$$

where $\alpha_m^2/2m_x m_y$ is the area of triangle AEH. If point E is to the right of B, the area of the small triangle BEF should be subtracted, which explains the 2nd term. Since triangle BEF is geometrically similar to triangle AEH, there is

$$\frac{\text{Area of BEF}}{\text{Area of AEH}} = \left(\frac{\alpha_m/m_x - \Delta x}{\alpha_m/m_x}\right)^2 = \left(\frac{\alpha_m - m_x\Delta x}{\alpha_m}\right)^2 \tag{2.57}$$

Similarly, the 3rd term is the area of the triangle DGH subtracted when point H lies above D. As the liquid area in one element is the multiplication of the total area A and volume fraction f, the position of the linear interface segment depends solely on α_m when f and $\mathbf{m}$ are known. Between any two closest critical volume fractions, Eq. (2.56) is a determined polynomial function of α_m whose roots can be solved analytically. Let f_w denote the edge wet ratio, which is the ratio of the wet region length on one edge to the total length of the edge. The correct solution should be able to give four reasonable f_w values which satisfy $0 \leq f_w \leq 1$.

The detailed formulas to calculate α_m and f_w are derived for all cases in Fig. 2.6 as follows.

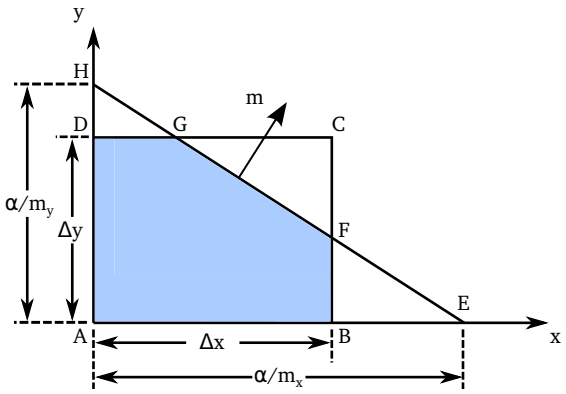

Figure 2.5: Polygon ABFGD is the liquid portion in one element. The location of the interface is determined by the volume fraction f and interface normal vector $\mathbf{m}$.

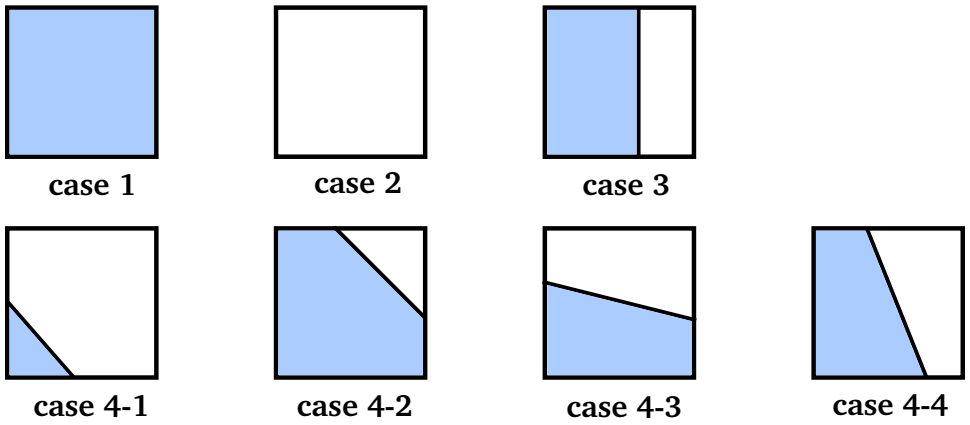

Figure 2.6: Elements are divided into 4 categories to calculate edge wet ratios based on the volume fraction, interface normal vector components and distance between the interface and the origin.

(1) When $f = 1$, $f_{w1} = f_{w2} = f_{w3} = f_{w4} = 1$

(2) When $f = 0$, $f_{w1} = f_{w2} = f_{w3} = f_{w4} = 0$

(3) When $0 < f < 1$ and $m_y = 0$ (which means the interface is parallel to edge 1), $f_{w1} = 1, \quad f_{w2} = f_{w4} = f, \quad f_{w3} = 0$

(4) When $0 < f < 1$, and $m_x > 0$ and $m_y > 0$

(4-1) Suppose $\alpha_m/m_x \leq \Delta x$ and $\alpha_m/m_y \leq \Delta y$. Then Eq. (2.56) becomes $Af =$

$\frac{\alpha_m^2}{2m_x m_y}$, and we have

$$\alpha_m = (2Afm_x m_y)^{1/2} \tag{2.58}$$

$$f_{w1} = \frac{\alpha_m}{m_y \Delta y}, \quad f_{w2} = \frac{\alpha_m}{m_x \Delta x}, \quad f_{w3} = f_{w4} = 0 \tag{2.59}$$

Check if $\alpha_m/m_x \leq \Delta x$, $\alpha_m/m_y \leq \Delta y$, $f_{w1} \leq 1$, $f_{w2} \leq 1$ are satisfied.

(4-2) Suppose $\alpha_m/m_x > \Delta x$ and $\alpha_m/m_y > \Delta y$

$$Af = \frac{\alpha_m^2}{2m_x m_y}\left[1 - \left(\frac{\alpha_m - m_x\Delta x}{\alpha_m}\right)^2 - \left(\frac{\alpha_m - m_y\Delta y}{\alpha_m}\right)^2\right] \tag{2.60}$$

$$Af = \frac{1}{2m_x m_y}\left[\alpha_m^2 - (\alpha_m - m_x\Delta x)^2 - (\alpha_m - m_y\Delta y)^2\right] \tag{2.61}$$

$$-\frac{1}{2m_x m_y}\alpha_m^2 + \frac{m_x\Delta x + m_y\Delta y}{m_x m_y}\alpha_m - \frac{m_x^2\Delta x^2 + m_y^2\Delta y^2}{2m_x m_y} - Af = 0 \tag{2.62}$$

Let

$$a = -\frac{1}{2m_x m_y}, \quad b = \frac{m_x\Delta x + m_y\Delta y}{m_x m_y}, \quad c = -\frac{m_x^2\Delta x^2 + m_y^2\Delta y^2}{2m_x m_y} - Af, \quad \Delta = b^2 - 4ac \tag{2.63}$$

Since $\alpha_m > 0$, we have

$$\alpha_m = \frac{-b + \sqrt{\Delta}}{2a} \tag{2.64}$$

Since we also have $BF = \frac{BE}{AE}AH$, then

$$f_{w3} = \frac{\alpha_m/m_x - \Delta x}{\alpha_m/m_x}\frac{\alpha_m/m_y}{\Delta y} = \frac{(\alpha_m/m_x - \Delta x)\, m_x}{m_y\Delta y} \tag{2.65}$$

Similarly,

$$f_{w4} = \frac{(\alpha_m/m_y - \Delta y)\, m_y}{m_x\Delta x} \tag{2.66}$$

Check if $\Delta > 0$, $\alpha_m/m_x > \Delta x$, $\alpha_m/m_y > \Delta y$, $f_{w3} \leq 1$ and $f_{w4} \leq 1$ are satisfied.

(4-3) Suppose $\alpha_m/m_x > \Delta x$ and $\alpha_m/m_y \leq \Delta y$

$$Af = \frac{\alpha_m^2}{2m_x m_y}\left[1 - \left(\frac{\alpha_m - m_x\Delta x}{\alpha_m}\right)^2\right] \tag{2.67}$$

$$\frac{1}{2m_x m_y}[2m_x\Delta x\alpha_m - m_x^2\Delta x^2] = Af \tag{2.68}$$

$$\alpha_m = \frac{2m_x m_y Af + m_x^2\Delta x^2}{2m_x\Delta x} \tag{2.69}$$

$$f_{w1} = \frac{\alpha_m}{m_y\Delta y}, \quad f_{w2} = 1, \quad f_{w3} = \frac{(\alpha_m/m_x - \Delta x)\, m_x}{m_y\Delta y}, \quad f_{w4} = 0 \tag{2.70}$$

check if $\alpha_m/m_x > \Delta x$, $\alpha_m/m_y \leq \Delta y$, $f_{w1} \leq 1$ and $f_{w3} \leq 1$ are satisfied.

(4-4) Suppose $\alpha_m/m_x \leq \Delta x$ and $\alpha_m/m_y > \Delta y$, similar to (4-3)

$$\alpha_m = \frac{2m_x m_y Af + m_y^2\Delta y^2}{2m_y\Delta y} \tag{2.71}$$

$$f_{w1} = 1, \quad f_{w2} = \frac{\alpha_m}{m_x\Delta x}, \quad f_{w3} = 0, \quad f_{w4} = \frac{(\alpha_m/m_y - \Delta y)\, m_y}{m_x\Delta x} \tag{2.72}$$

Check if $\alpha_m/m_x \leq \Delta x$, $\alpha_m/m_y > \Delta y$, $f_{w2} \leq 1$, and $f_{w4} \leq 1$ are satisfied.

After the four edge wet ratios are obtained, each element is assigned an element type according to the shape of the liquid portion as in Fig. 2.7. Cases (3), (4-3), (4-4) are combined into one element type. For case (4-3), we need to rotate the coordinate system again to ensure the edge with a wet ratio of 1 to be the first edge.

Next, using the velocity field and the location of interface in each partially-filled element, new f is determined at the new time step. The advection algorithm is used to evolve f in time. We divided all elements into three categories similar to those given in

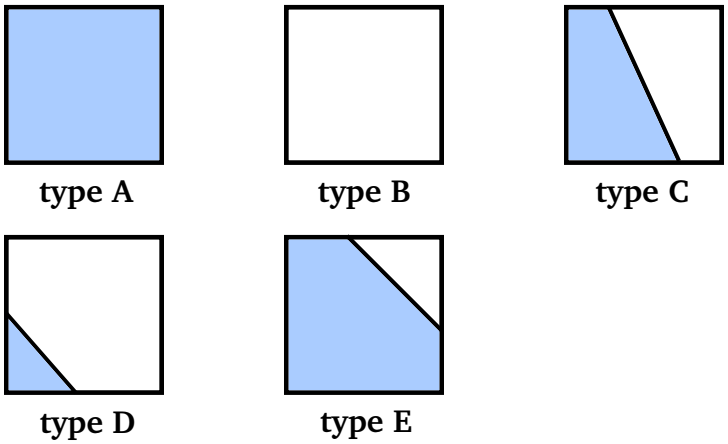

Figure 2.7: Elements are re-divided into 5 types according to the shape of the liquid portion.

Ref. [69]

$$\begin{cases} \text{internal element} & (f = 1, \quad \dot{Q}_{net} = 0) \\ \text{active element} & (0 \leq f \leq 1, \quad \dot{Q}_{net} \neq 0) \\ \text{external element} & (f = 0, \quad \dot{Q}_{net} = 0) \end{cases} \tag{2.73}$$

where $\dot{Q}_{net}$ is the net flux. Only active elements' volume fractions need to be updated. Internal and external elements will keep their volume fractions. The active elements are further categorized into three types, (1) partially-filled elements, (2) full elements with at least one partially-filled or empty neighbor element, and (3) empty elements with at least one partially-filled or full neighbor element. It is important to point out that, for the FE formulation of the Navier-Stokes equations given in Eq. (2.35), the fluid mass is not necessarily conserved in the active elements, i.e. $\nabla \cdot \mathbf{V} \neq 0$. To add the correction, the original transport equation of f Eq. (2.48) is rewritten as

$$\frac{\partial f}{\partial t} + \nabla \cdot (\mathbf{V} f) = f \nabla \cdot \mathbf{V} \tag{2.74}$$

The operator split method for the advection [66] is adopted for Eq. (2.74):

$$f_t + (fu)_x = fu_x \tag{2.75}$$

$$f_t + (fv)_y = fv_y \tag{2.76}$$

For the element (i, j), in order to maintain conservation of f, it is necessary to discretize f implicitly on the right hand side of Eq. (2.75) and explicitly on the right hand side of Eq. (2.76) as [66]

$$\tilde{f}_{i,j} = \frac{f^n_{i,j} + \frac{\Delta t}{\Delta x}(F_{i-1/2,j} - F_{i+1/2,j})}{1 - \frac{\Delta t}{\Delta x}(u_{i+1/2,j} - u_{i-1/2,j})} \tag{2.77}$$

$$f^{n+1}_{i,j} = \tilde{f}_{i,j} + \frac{\Delta t}{\Delta y}(\tilde{G}_{i,j-1/2} - \tilde{G}_{i,j+1/2}) + \tilde{f}_{i,j}\frac{\Delta t}{\Delta y}(v_{i,j+1/2} - v_{i,j-1/2}) \tag{2.78}$$

where the tilde sign indicates the intermediate values of f and fluxes. After $\tilde{f}_{i,j}$ is determined from Eq. (2.77), the intermediate interface is constructed and vertical fluxes are calculated with the intermediate interface location. Then $f^{n+1}_{i,j}$ at the new time level is determined from Eq. (2.78). This procedure can be made second-order accurate simply by alternating the sweep direction at each time step [66].

The procedure for the Volume of Fluid method is as follows. (1) Determine a proper time step. (2) Mark full, empty and partially-filled elements. (3) For full and empty elements, obtain the edge wet ratios directly. For partially-filled elements, estimate the interface normal vector in each element. (4) Compute edge wet ratios of partially-filled elements. (5) Mark internal, external and active elements. (6) Compute $\frac{u_{i+1/2,j} - u_{i-1/2,j}}{\Delta x}$ or $\frac{v_{i,j+1/2} - v_{i,j-1/2}}{\Delta y}$ in all active elements depending on the direction in which the sweep occurs. (7) Compute edge outflow volumes in all active elements and their neighbors in the 1st direction (edge inflow volumes of active elements are set as edge outflow volumes of their neighbor elements). (8) Obtain intermediate volume fractions. (9) Repeat (2-6). (10)

Compute edge outflow volumes in all active elements and their neighbors in the 2nd direction. (11) Obtain volume fractions at new time. (12) Redistribute any volume fraction undershoots or overshoots.

2.2.2.4 Surface tension model

The surface tension term $-\sigma\kappa\nabla H(f)$ in the FE formulation is implemented using the sharp surface tension force model (SSF) [59, 72]. Surface tension forces acting on the interface are transformed into volume forces in partially-filled elements at the gas-liquid interface. In this approach, one single model for the two-phase flow is adequate and the added volume forces will enforce the discontinuous interfacial condition in pressure. While the SSF models described in Refs. [59, 72] were derived in finite difference formulation (FD) with either VOF/reconstructed distance function (RDF), or coupled level set and volume of fluid (CLSVOF) for interface tracking, in this work, we reformulate the model in FE implementation with VOF for interface tracking. Figure 2.8 illustrates the difference. In the FD implementation shown in Fig. 2.8a, Ref. [59] considers an vertical interface between cells (i, j) and $(i + 1, j)$ with liquid on the right and gas on the left, and the surface tension force is obtained as

$$\mathbf{f}^{SSF}_{i+1/2,j} = -\sigma\kappa_{i+1/2,j}\frac{H(\phi)_{i+1,j} - H(\phi)_{i,j}}{\Delta x} \tag{2.79}$$

where ϕ is the level set function, $H(\phi)$ the Heaviside step function, and $\kappa_{i+1/2,j}$ the edge curvature value interpolated from cell centers. In this work as shown in Fig. 2.8b, however, the values of the Heaviside function $H(f)$ are set at element vertices instead of centers, and the surface tension force is calculated as a function of f at the center of the element (i, j) as

$$\mathbf{f}^{SSF}_{i,j} = -\sigma\kappa_{i,j}\nabla H(f)_{i,j} \tag{2.80}$$

where the $\nabla H(f)_{i,j}$ is evaluated with the derivatives of shape functions.

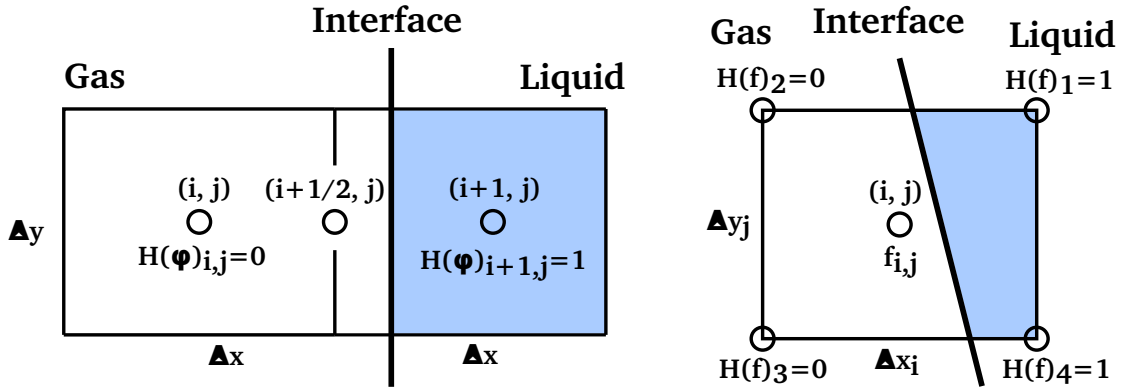

Figure 2.8: Schematic diagrams showing how SSF is evaluated in (a) FD formulation and (b) FE formulation with the interface between gas (left) and liquid (right).

The accuracy of surface tension force depends on the curvature estimation. The height function method [73], in which the curvature is constructed based on sums of volume fractions, has been shown to be able to give second order convergence rate [74]. The height function algorithm is given in the following [73].

1. A 3x7 stencil is employed for 2-D cases. The stencil is centered at the element in which the curvature should be estimated and aligned in the direction of the larger component of the interface normal vector $\mathbf{m}$.

2. Create 3 height functions in the y direction by summing volume fractions of each column

$$h_{i,j} = \sum_{j-3}^{j+3} f_{i,j} \Delta y_j \tag{2.81}$$

3. The curvature is evaluated as

$$\kappa = \frac{h_{xx}}{(1 + h_x^2)^{3/2}} \tag{2.82}$$

where h_x and h_{xx} are estimated with finite difference formulations.

In many cases the stencil does not need to be so high, whereas other cases may require more elements in the y direction in order to obtain an accurate curvature. Thus a local asymmetric stencil is built adapted to the interface geometry shown in Fig. 2.9a: a 1x3, 1x4 and 1x5 stencil for the left, central and right column, respectively. In some cases the direction "best aligned" with $\mathbf{m}$ will not give an curvature value, then the 2nd direction will be tried.

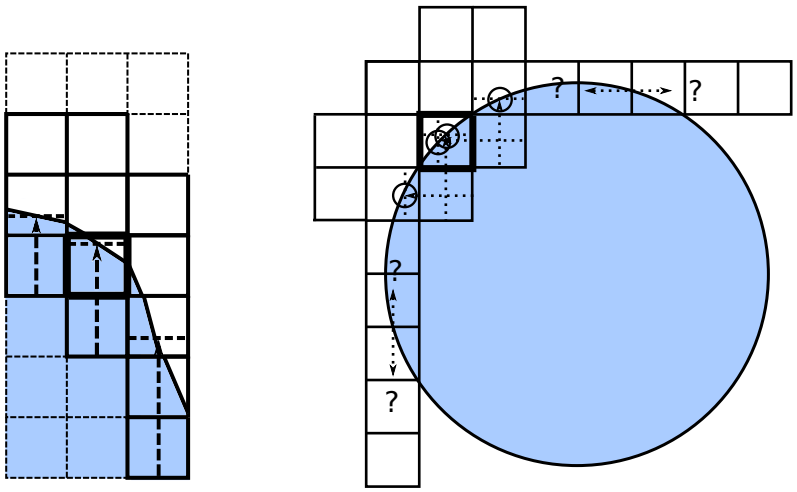

(a) (b)

Figure 2.9: (a) Asymmetric stencils are built independently for each column (solid lines) to estimate the curvature. (b) In this case for both horizontal and vertical stencils, only 2 out of 3 interface positions can be obtained.

Sometimes even for a moderately curved interface, the height functions can not be constructed. As shown in Fig. 2.9b, both the horizontal and vertical estimations fail, even though the mesh is not very coarse as the radius of curvature of the interface is around 4Δ. However, a combination of both stencils can give 4 average interface positions (the circles in Fig. 2.9b). Fitting a parabola through these points and differentiating the analytical function will give an estimate of the curvature. Given an element and n interface positions $[\mathbf{x}_1, ..., \mathbf{x}_n]$, the parabola-fitting procedure is listed below [73].

1. If the number of independent interface positions is smaller than 3, return an error.

Two interface positions $\mathbf{x}_i$ and $\mathbf{x}_j$ are considered independent if $|\mathbf{x}_i - \mathbf{x}_j| \geq \Delta$, which will ensure that the minimization problem is well-conditioned.

2. At the center $\mathbf{o}$ of the reconstructed interface fragment in the element, define an orthonormal coordinate system $R \equiv [\mathbf{o}, \mathbf{i}', \mathbf{m}]$.

3. Compute the transformed coordinates $[\mathbf{x}'_1, ..., \mathbf{x}'_n]$ of the interface positions.

4. Fit a parabola by minimizing

$$F(\mathbf{a}) \equiv \sum_{1 \leq k \leq n} [y'_k - f(\mathbf{a}, x'_k)]^2 \tag{2.83}$$

with

$$f(\mathbf{a}, x) \equiv a_0 x^2 + a_1 x + a_2 \tag{2.84}$$

5. The mean curvature at the origin $\mathbf{o}$ of R is

$$\kappa \equiv \frac{2a_0}{(1 + a_1^2)^{3/2}} \tag{2.85}$$

If the number of independent interface positions given by height-function estimation is less than 3, the centers of the reconstructed interface fragments in each element of the 3x3 stencil will be taken as the new set of interface positions. Then the parabola-fitting procedure will be repeated to obtain the curvature. If enough independent positions can still not be found, the curvature will be simply set as zero.

2.2.2.5 Flow chart

The procedure for the entire FE implementation is shown in the flow chart in Fig. 2.10. The liquid-gas interface tracking, magnetic scalar potential equation, and Navier-

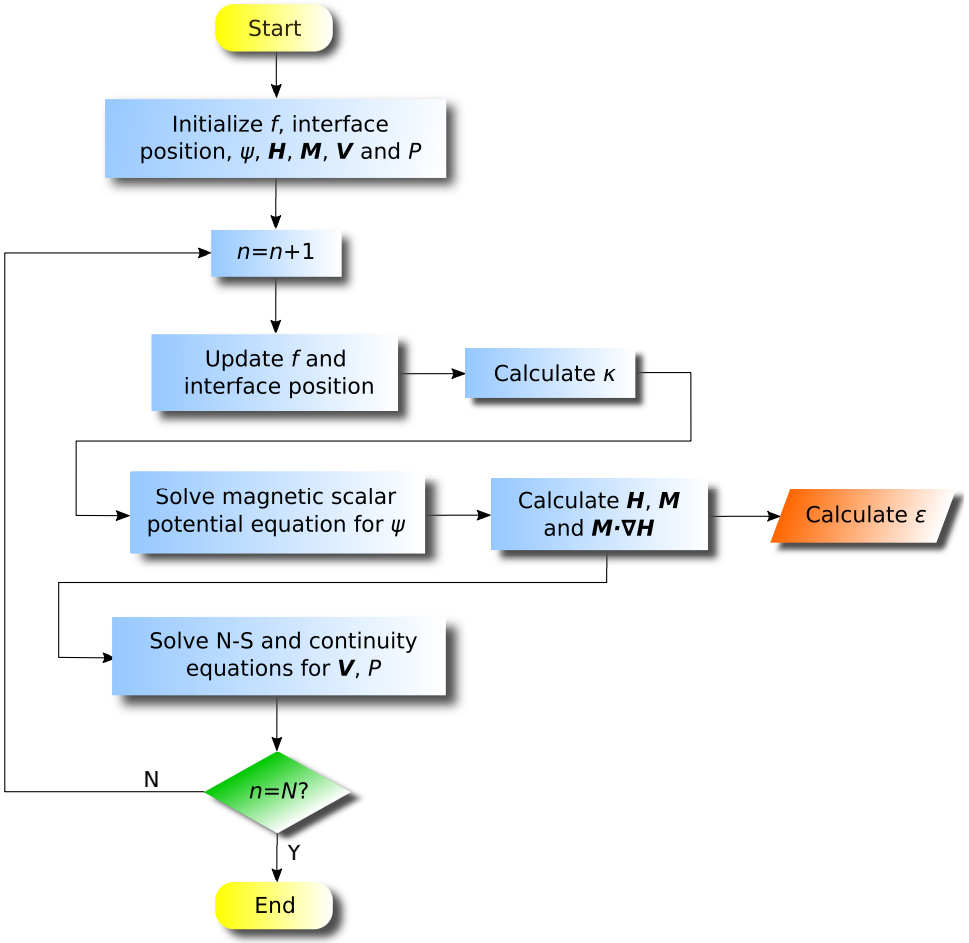

Figure 2.10: Flow chart showing the algorithms of the FE model.

Stokes equations are weakly and sequentially coupled in time. At each time step, first, the volume fraction f is updated at the element centers and nodes based on the previous liquid-gas interface location and velocity field $\mathbf{V}$, and then the interface is reconstructed for the current time step. The interface curvature κ and surface tension force are calculated at partially-filled element centers. Second, ψ and $\mathbf{H}$ are calculated throughout the entire domain based on the new liquid-gas interface. $\mathbf{M}$ and magnetic body force are calculated at the nodes of the elements containing ferrofluid (including partially-filled elements). Then the RMS electromotive force ε is calculated from ψ and $\mathbf{M}$. Third, the Navier-Stokes

equations are solved through a nonlinear iteration to obtain the velocity $\mathbf{V}$ and pressure P fields inside the tank. The procedure is repeated for the next time step until the prescribed simulation time is reached.

2.3 Results and Discussion

2.3.1 Model validation

Before we delve into delineating the influence of the design parameters on the performance of the system, we need to validate the computational model. To this end, we obtain the magnetic and sloshing characteristics of the ferrofluid in the tank using the proposed FE model and compare the results to experimental data and other theoretical or computational results available in the literature.

2.3.1.1 Magnetic flux density distribution

By using the FE formulation of the magnetic scalar potential equation, the magnetic flux density distribution is calculated in a rectangular domain with two permanent magnets as shown in Fig. 2.2. The two permanent magnets are placed 18.16 cm apart and the north poles of the magnets are facing each other. The dimensions of the magnets are $30.48 \times 2.45 \times 1.27$ cm^3. The typical remanent magnetic flux density of a ferrite magnet is 0.38 T [57]. Keep in mind that the FE model is two-dimensional and hence the numerical scheme provides the $\mathbf{B}$ distribution in the xy plane under the assumption that the magnets have an infinite length in the z direction. In the experimental setup, $l_z \gg l_x$ and $l_z \gg l_y$ are ensured and it can be seen in Fig. 2.11a that B_x is almost uniform along $y = 0$ from $z = -7.62$ cm to $z = 7.62$ cm, which indeed illustrates that magnetic analysis can be simplified into a 2-D problem. The calculated and measured B_x values match quite well

as shown in Fig. 2.11b. Thus, the 2-D FE model is sufficient and accurate to capture the magnetic behavior of the energy harvesting system.

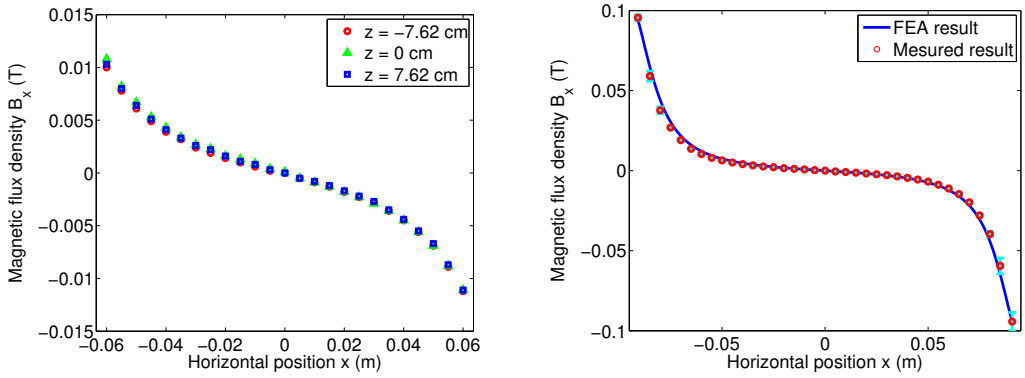

(a) (b)

Figure 2.11: (a) Zoomed experimental results of B_x at $y = 0$ along the x direction from $z = -7.62$ cm to $z = 7.62$ cm between two permanent magnets with north poles facing each other. (b) Comparison of FEA and averaged experimental results of B_x at $y = 0$ along the x direction.

2.3.1.2 Sloshing dynamics

Two sloshing problems are considered to verify the FE implementation of the Navier-Stokes equations, continuity equation and Volume of Fluid (VOF) method used in the FE analysis. First, we consider a case of small-amplitude sloshing in which the same configuration as the one discussed in Ref. [75] is analyzed. The dimensions of the tank are chosen as length L_t = 0.2 m, height H_t = 0.2 m. The depth of liquid D is 0.1 m. The densities of water and air are set as $\rho_1 = 1000$ kg/m^3 and $\rho_2 = 1.29$ kg/m^3, respectively. Inviscid flow is assumed in this case. The excitation has a form of $x_b(t) = A_0 \sin(\omega t)$ with the amplitude $A_0 = 0.186$ mm and frequency $\omega = 0.999\omega_0$. A 100×80 element mesh is used with denser elements arranged near the interface. The prescribed time step Δt is set to be 0.0005 s.

Results of the computational model are compared to the linearized analytical solu-

tion obtained by Faltinsen's [75] in which the wave elevation can be obtained using

$$\xi = \xi_1 + \xi_2 \tag{2.86}$$

where

$$\xi_1 = \frac{A_0}{g}\left(x\omega^2 + \sum_{m=0}^{\infty} C_m \omega \sin k_m x\right)\sin \omega t \tag{2.87}$$

$$\xi_2 = -\frac{A_0}{g}\sum_{m=0}^{\infty} \omega_m \left(C_m + \frac{H_m}{\omega^2}\right)\sin k_m x \sin \omega_m t \tag{2.88}$$

$$k_m = \frac{2m+1}{L_t}\pi \qquad \omega_m^2 = g k_m \tanh k_m D \tag{2.89}$$

$$H_m = \omega^3 \frac{4}{L_t}\frac{(-1)^m}{k_m^2} \qquad C_m = \frac{H_m}{\omega_m^2 - \omega^2} \tag{2.90}$$

where g denotes the gravitational acceleration. The time history of non-dimensional interface elevation at $x = -L_t/2$ is shown in Fig. 2.12a. It is evident that the FE result agrees well with the analytical result.

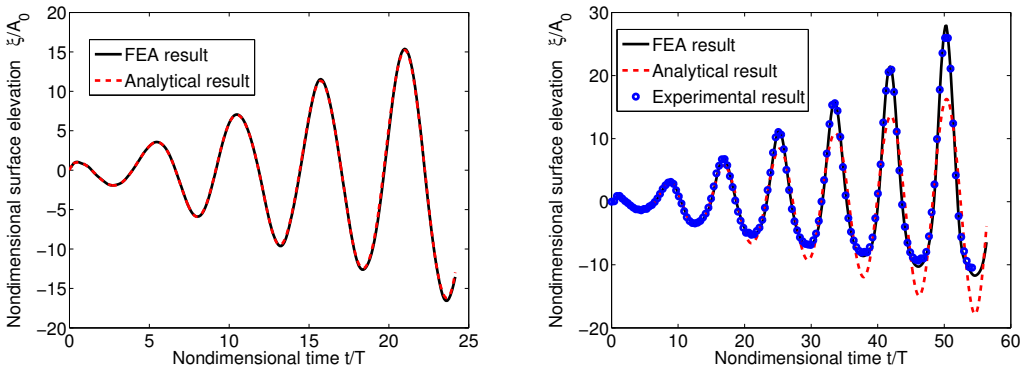

(a) (b)

Figure 2.12: (a) FEA and analytical results of time history of interface elevation at $x = -L_t/2$ for small amplitude sloshing. (b) FEA, experimental [5] and analytical results of time history of interface elevation at $x = 0.265$ m for large amplitude sloshing.

Next, the configuration described in Ref. [5] is adopted for large amplitude slosh-

ing. The tank has a length of 0.57 m, height of 0.3 m and water depth of 0.15 m. The densities and viscosities of water and air are set as $\rho_1 = 1000$ kg/m^3, $\rho_2 = 1.29$ kg/m^3, $\eta_1 = 1$ mPa·s and $\eta_2 = 0.01837$ mPa·s, respectively. The displacement of shaker is $x_b(t) = -A_0 \sin(\omega t)$ with $A_0 = 5$ mm and $\omega = \omega_0$. A 114×70 mesh refined near the interface is used in this case. Time step Δt is taken as 0.001 s. The time history of non-dimensional interface elevation at position 20 mm from the right side wall of the tank is shown in Fig. 2.12b. The result shows that, while the analytical solution fails to capture the nonlinear characteristics of large amplitude sloshing, the numerical result obtained from using the FE model agrees well with the experimental data from Ref. [5].

2.3.1.3 Capillary wave

To verify that the FE implementation can properly capture the surface tension force, the FE result is compared to the analytical solution for a small amplitude damped capillary wave problem between two superposed fluids of identical density and kinematic viscosity [68, 73, 76–78]. The configuration given in Ref. [78] is used in this case. The domain is a $2\pi \times 2\pi$ square box divided vertically in 2 parts. A cosinoidal disturbance $A(t)_{t=0}\cos(x)$ of wavelength $\lambda = 2\pi$ and amplitude $A(t)_{t=0} = A_0 = 0.01\lambda$ is applied to the flat interface between the two fluids. The non-dimensional parameters are given as $\rho_1 = \rho_2 = 1$, $\nu_1 = \nu_2 = 0.064720863$ and $\sigma = 2$. Periodic boundary conditions are used in the x direction and slip conditions in the y direction. The FE simulation is performed with a mesh of 128×128 elements and Δt of 0.003. Results are compared to the analytical solution obtained by Prosperetti [78]

$$A(t) = \frac{4(1-4\beta)\nu^2}{8(1-4\beta)\nu^2 + \omega_0^2} A_0 \text{erfc}\sqrt{\nu t} + \sum_{i=1}^{4} \frac{z_i}{Z_i} \frac{\omega_0^2 A_0}{z_i^2 - \nu} \exp\left[(z_i^2 - \nu)t\right] \text{erfc}(z_i\sqrt{t}) \quad (2.91)$$

where z_i are roots of

$$z^4 - 4\beta\sqrt{\nu}z^3 + 2(1-6\beta)\nu z^2 + 4(1-3\beta)\nu^{3/2}z + (1-4\beta)\nu^2 + \omega_0^2 = 0 \qquad (2.92)$$

and

$$\beta = \frac{\rho_1\rho_2}{(\rho_1+\rho_2)^2} \qquad \omega_0 = \sqrt{\frac{\sigma}{\rho_1+\rho_2}} \qquad Z_i = \prod_{j=1,j\neq i}^{4}(z_j - z_i) \qquad (2.93)$$

Figure 2.13 shows the temporal evolution of the non-dimensional elevation at the center of the interface. The FE result agrees well with the analytical result.

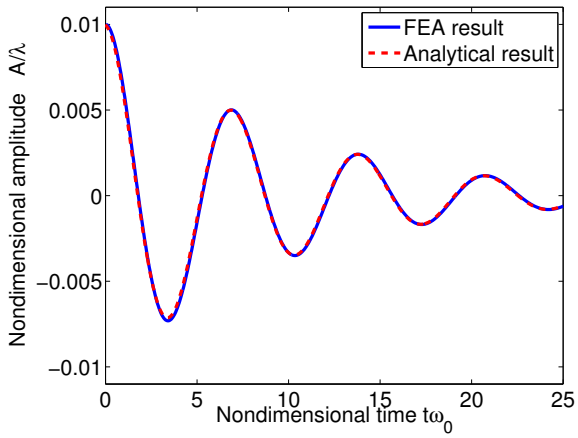

Figure 2.13: FE and analytical results of temporal evolution of the amplitude of a capillary wave.

2.3.2 Numerical results of ferrofluid based energy harvesting

Having individually validated the electromagnetic and sloshing fluid dynamics models in Sec. 2.3.1, in this section, the coupled ferrofluid-electromagnetic model is employed to simulate the transient and steady-state behavior of the ferrofluid energy harvester described in Fig. 2.1a. The numerical results are then compared to experimental results ob-

tained using the experimental setup shown in Fig. 2.1a. The purpose of this investigation lies in three folds: (1) validate the coupled model for the application of ferrofluid energy harvesting, (2) elucidate the underlying mechanisms that determine the electromotive force of the energy harvester, and (3) reveal the significance of several modeling aspects on the accuracy of the model prediction.

As the tank has a wall thickness of 6 mm, and the coil is tightly wound around the tank with a thickness of 2 mm, there is an averaged 7 mm gap between the ferrofluid and coil. In order to compare the experimental and numerical results, this gap needs to be included in the numerical integration region in the xy plane for the electromotive force calculation in Eqs. (2.14-2.17). In addition, the 2-D numerical electromotive force needs to be multiplied by a dimension in the z direction, W_t, to demonstrate the final output of a 3-D energy harvester. In this chapter, W_t is taken as 13.4 cm (the average of the tank dimension 12.7 cm, and the coil dimension 14.1 cm including the tank wall and wire thickness).

In the FE simulation, a quadrilateral mesh of 23632 elements with 80×80 rectangular elements inside the tank is used. The Courant number is set at 0.25. Figure 2.14 illustrates snapshots of the sloshing ferrofluid in the tank together with the magnetic flux lines as computed using the FE model for Config. (1H) and Config. (4V), respectively. It is evident that the original magnetic field is altered by the ferrofluid motion.

2.3.2.1 Experimental validation

Comparison of experimental and numerical results of the electromotive force as a function of excitation frequency for all configurations and windings is shown in Figs. 2.15 through 2.18. The results show that the electromotive force-excitation frequency characteristics of the energy harvester are captured by the simulations. Within the range of frequency sweep considered, there are two peaks of ε. The higher peak occurs at the system's first modal frequency which is around 1.9 Hz whereas the lower peak occurs at around 1.5 Hz.

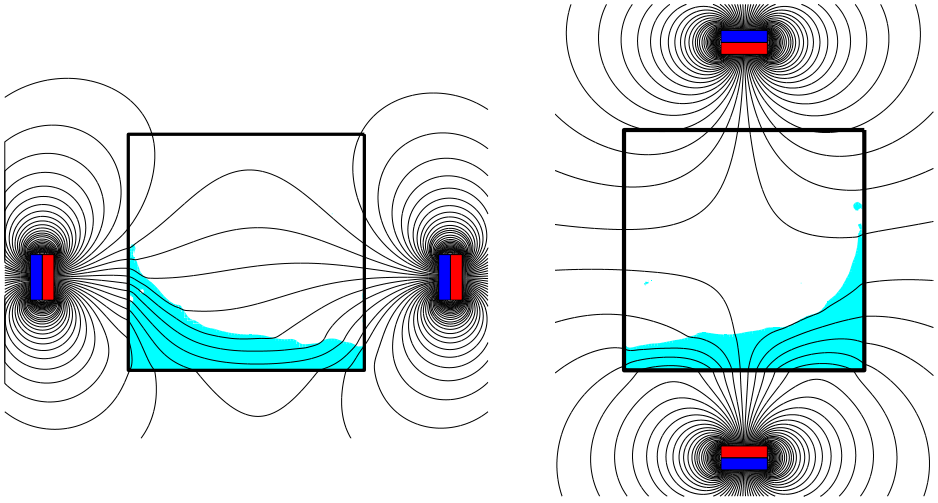

(a) (b)

Figure 2.14: Snapshots of the ferrofluid sloshing and the magnetic flux lines for (a) Config. (1H) and (b) Config. (4V).

The lower peak appears due to an internal resonance between the first and second vibration modes. Internal resonances occur when two or more modal frequencies of the fluid column are commensurate or nearly commensurate. It turns out that, for the design parameters used in the experimental setup, ω_1 is approximately half of ω_2. As such, an internal energy pump is activated between the two modes causing the smaller peak to appear. The internal resonance enables the energy harvester to respond to a fairly wider range of excitation frequencies [29].

While in general the numerical and experimental results are in reasonably good agreement, the numerical results show slight peak shifts and small differences in magnitude as compared to the experimental results. Both the peak shift and the magnitude difference are mainly due to the 2-D model simplification in the FE simulations. The dimension of ferrofluid in reality is not infinite in the z direction. As will be shown later in this section, the discrepancies between the numerical and experimental results are reduced by increasing the size of the tank in the z direction. Even when using the 2-D assumption, the shifts between the peak frequencies are less than 0.1 Hz, and the magnitude differences are

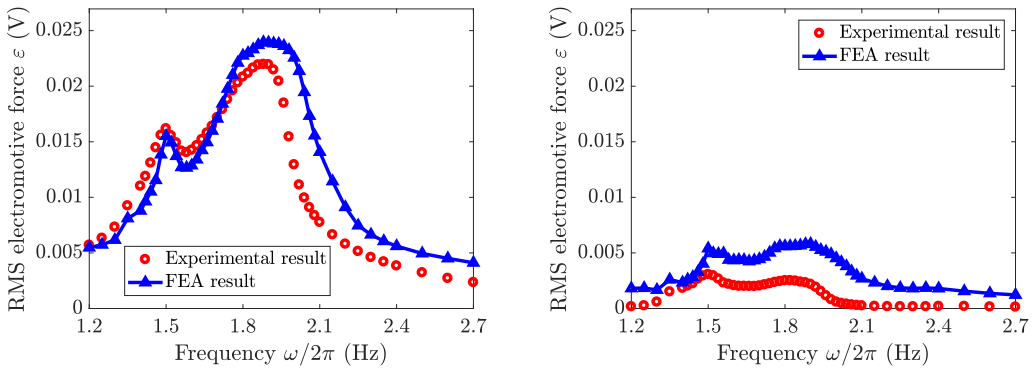

Figure 2.15: Comparison of experimental and FEA results for (a) Config. (1H), (b) Config. (1V).

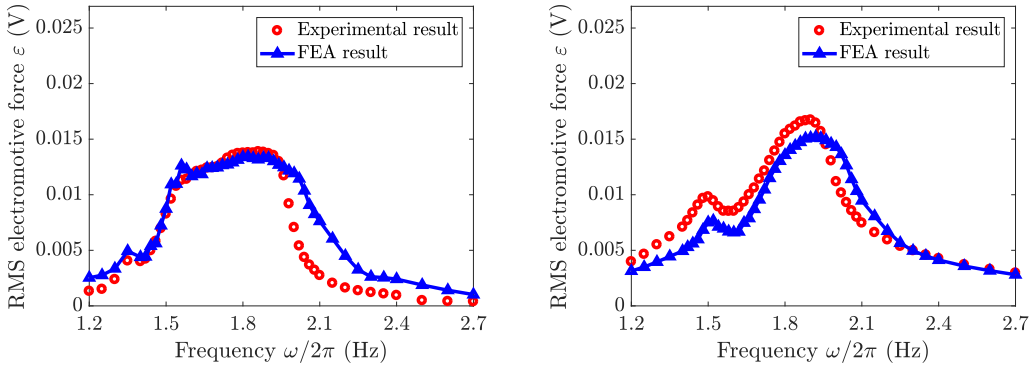

Figure 2.16: Comparison of experimental and FEA results for (a) Config. (2H), (b) Config. (2V).

less than 5 mV for all cases.

2.3.2.2 Influence of harvester's configuration on electromotive force

Comparing results of the eight configurations, it becomes evident that Config. (1H) in Fig. 2.15a produces higher values of the electromotive force, ε. This is due to the fact that, in this configuration, the change of magnetic flux in each sloshing cycle is higher. Note that, in all the test cases, the majority of ferrofluid motion occurs in the lower region of the tank for the given tank length, ferrofluid depth and excitation acceleration. In Config.

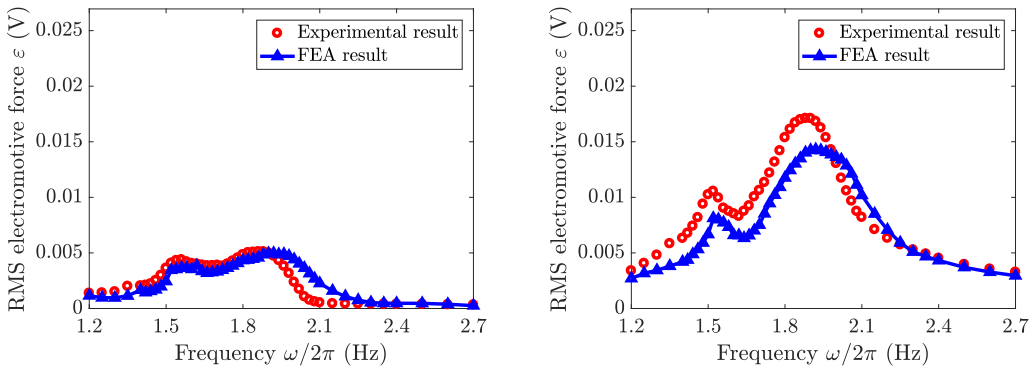

Figure 2.17: Comparison of experimental and FEA results for (a) Config. (3H), (b) Config. (3V).

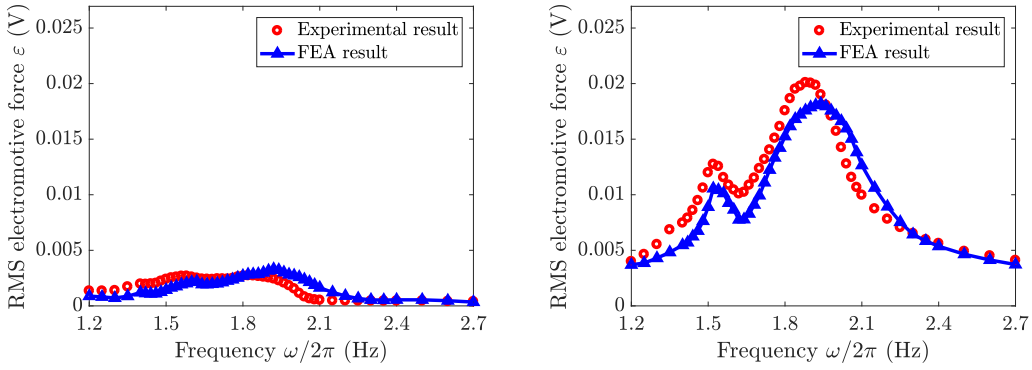

Figure 2.18: Comparison of experimental and FEA results for (a) Config. (4H), (b) Config. (4V).

(1H), the copper coil is wound horizontally, therefore only B_y is of concern. Since the two magnets have opposite poles facing each other, some magnetic field lines coming out of the left north pole go back into the right south pole passing through the tank as shown in Fig. 2.14a. Therefore, H_y is directed downwards in the bottom left region of the tank and upwards in the bottom right region. During an oscillation cycle, when the ferrofluid moves to the left, downward B_y increases in the left region due to the added downward M_y carried by the ferrofluid moving to that region. On the other hand, upward B_y decreases in the right region because the magnetized ferrofluid moves away from that region. The two

effects add up and lead to a net decrease in Φ_{By}.

On the contrary, when the ferrofluid flows back to the right, downward B_y decreases in the left side whereas upward B_y increases in the right side. This leads to a net increase in Φ_{By}. Apparently, in this case, H_y changes direction inside the ferrofluid from left to right, and hence the change of Φ_{By} is large in each cycle which implies that ε is large. However, for Config. (1V), since H_x is rightward almost in the entire tank, the change of Φ_{Bx} due to sloshing is small, resulting in a much lower ε.

Figure 2.18b shows that Config. (4V) also produces high ε. Since the two north poles face each other, magnetic field lines coming out of the north pole go back to the south pole of the same magnet as shown in Fig. 2.14b. As a result, H_x generated by the two magnets adds up and is leftward in the left region of the tank and rightward in the right region. In this case, H_x also goes in opposite directions from left to right inside the ferrofluid. Therefore, in a sloshing cycle, the rate of change in Φ_{Bx} is large. On the contrary for Config. (4H), H_y is upward in the whole bottom region and the change of Φ_{By} is small in a sloshing cycle, leading to lower ε. For similar reasons, Configs. (2V) and (3V) also produce higher ε values compared to Configs. (2H) and (3H). The magnitude of ε, however, depends on the positions of the magnets, tank length, ferrofluid depth, and excitation acceleration.

2.3.2.3 Validity of the 2-D assumption

Next, several modeling aspects are investigated to elucidate their effects on the accuracy of the model prediction. First, as discussed previously, the energy harvester is simplified to a 2-D system in the computational model. In the experimental setup, however, both the tank and the magnets have finite length in the z direction. The 3-D effect becomes more significant when their size in the z direction decreases. To illustrate this, the experiments and numerical analyses are repeated for a smaller tank of $10.16\times10.16\times10.16$ cm^3.

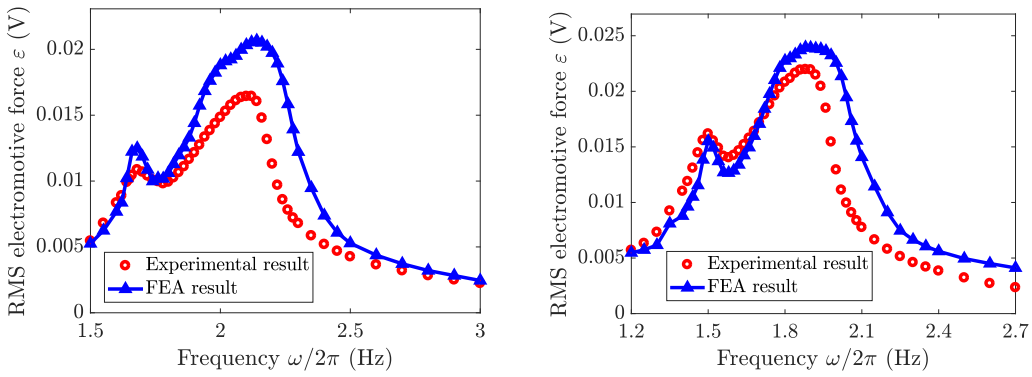

Figure 2.19: Comparison of experimental and FEA results for Config. (1H) with (a) 10.16 cm tank, (b) 12.7 cm tank.

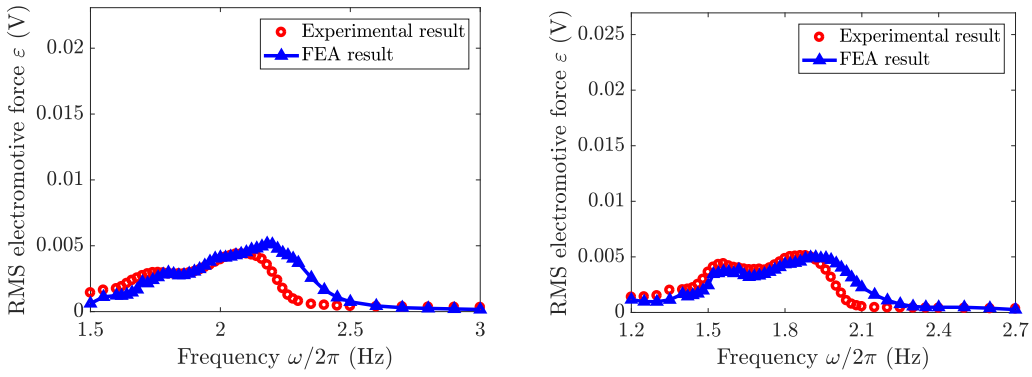

Figure 2.20: Comparison of experimental and FEA results for Config. (3H) with (a) 10.16 cm tank, (b) 12.7 cm tank.

The experimental and numerical results for both 10.16 cm and 12.7 cm tanks are compared in Figs. 2.19 and 2.20. The ferrofluid depth for the 10.16 cm tank is taken as 2 cm to ensure the same ratio of ferrofluid depth to tank length. When comparing Fig. 2.19a and Fig. 2.19b, it becomes evident that the magnitude difference between the experimental and numerical results is smaller for the larger (12.7 cm) tank. Comparison of Figs. 2.20a and 2.20b indicates that the difference in the peak frequency between the experimental and numerical results is also smaller for the larger (12.7 cm) tank. This study reveals that the 3-D effect plays an important role in the accuracy of the numerical results. Therefore, the tank

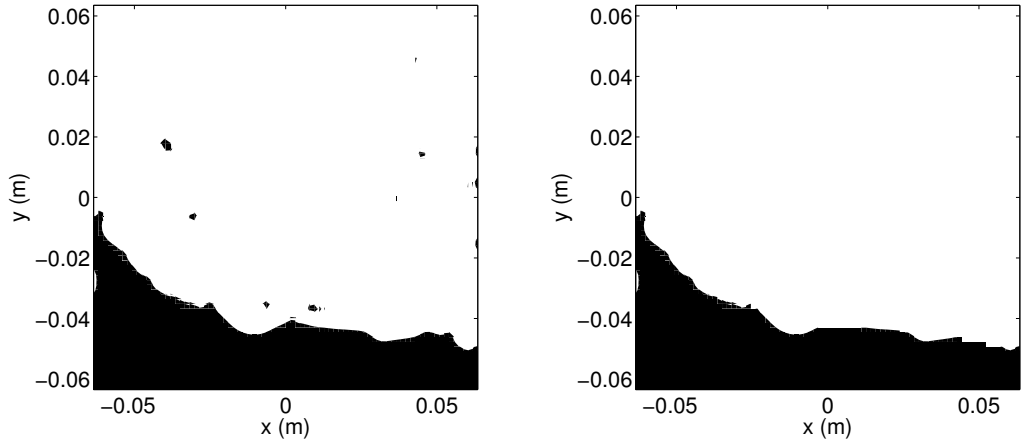

Figure 2.21: Comparison of fluid flow snapshots at $t = 6.62$ s for Config. (1H) with excitation frequency of 1.84 Hz and (a) without surface tension, (b) with surface tension.

size in the z direction must be sufficiently large for the 2-D approximation of the system to be valid.

2.3.2.4 Influence of surface tension

We study the influence of the surface tension of the ferrofluid on the accuracy of the computational model. Extensive numerical results were performed showing that simulations with and without surface tension give no significant difference in the calculation of the electromotive force, ε. Figure 2.21 shows snapshots of the fluid flow at the same instant for the two cases. The bulk of ferrofluid follows the same flow pattern in both cases, which explains why they lead to similar ε. However, without surface tension, the liquid-gas interface is not as smooth and ferrofluid droplets are easily generated and sprinkled in the air. Thus, surface tension should still be considered in the computational model to more faithfully describe the motion of the ferrofluid.

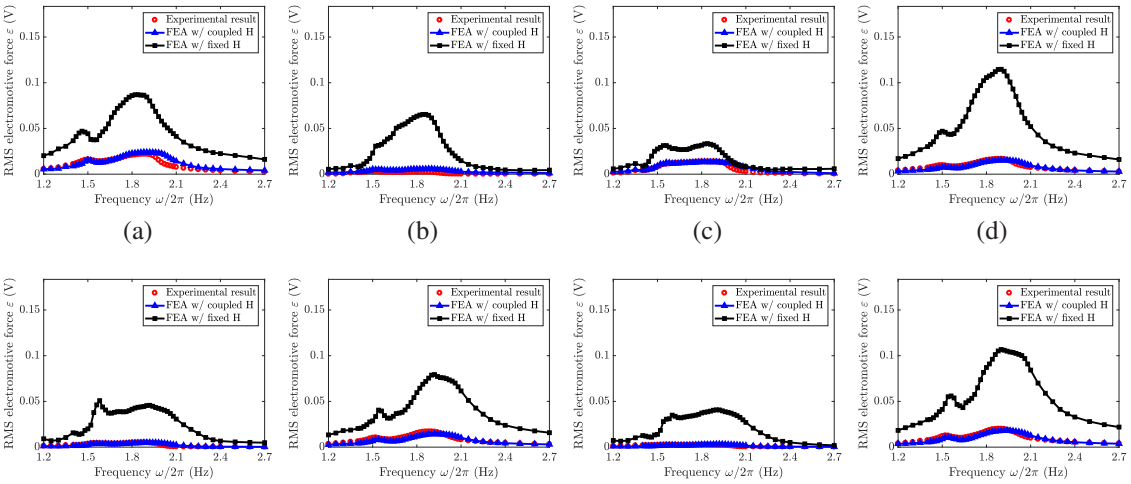

Figure 2.22: Comparison of experimental results, FEA results with coupled H and FEA results with fixed H for (a) Config. (1H), (b) Config. (1V), (c) Config. (2H), (d) Config. (2V), (e) Config. (3H), (f) Config. (3V), (g) Config. (4H), (h) Config. (4V).

2.3.2.5 Dependence of the magnetic field distribution on the fluid motion

If $\mathbf{H}$ can be assumed independent of the ferrofluid motion one can significantly simplify the computational analysis for the energy harvesting application. To test the validity of this assumption, the numerical simulations are repeated for all configurations with an invariant $\mathbf{H}$ field. That is, those simulations use one-way coupling: the magnetic field influences the fluid motion, but not vice versa. Results shown in Fig. 2.22 indicate that the one-way coupling gives much larger electromotive forces than the experimental values. Examining the detailed $\mathbf{H}$ profile in the tank obtained from the two-way coupling scheme, we observe that $\mathbf{H}$ is in fact smaller in the ferrofluid than in the air. This is because the magnetic scalar potential equation require the normal component of $\mathbf{B}$ to be continuous at the liquid-gas interface, and the relation $\mathbf{B} = \mu_0(1 + \chi)\mathbf{H}$ leads to a jump in the magnitude of H_n across the interface, creating a smaller $\mathbf{H}$ magnitude inside the ferrofluid. In the one-way coupling scheme in which $\mathbf{H}$ does not depend on the ferrofluid motion, the magnitude of H_n does not undergo a sudden reduction when getting into the ferrofluid,

which eventually causes larger $\mathbf{B}$ and ε. Therefore, it is evident that the influence of fluid motion on the magnetic field is strong, and two-way coupling is necessary and crucial for the numerical analysis of the energy harvester.

Chapter 3

Performance Analysis of the Energy Harvester

Experimental results showed that the transduction efficiency of the ferrofluid based energy harvester depends on many factors including the magnet placement, tank geometry, ferrofluid depth and excitation amplitude [28–30]. Understanding how these factors affect the energy conversion performance can help the design and optimization of high performance ferrofluid based energy harvesters. While experimental test is a direct approach to measure the effects of these factors on the performance of the device, it is very expensive and limited by the availability of research equipment and materials. Having developed and validated the continuum level computational model presented in Chapter 2, in this chapter, a parametric study is conducted to investigate the effects of device design parameters and material properties on the output electromotive force.

In Chapter 2, a total of eight configurations of the energy harvester - four types of permanent magnet placement combined with a horizontal or vertical coil - are investigated. The results reveal that the two configurations shown in Fig. 3.1, referred to as Config. (1) and Config. (2), give the largest electromotive forces. In Config. (1), the two permanent

magnets are placed on the two sides of the tank with north-south poles directed in the same direction and the coil wound horizontally. In Config. (2), the two magnets are placed above and below the tank with the north poles facing each other and the coil wound vertically. The two configurations are chosen for the performance analysis for two reasons: (1) their high performance compared to other configurations warrants further investigation, and (2) the two configurations have completely different magnet placements, pole alignments and coil windings, indicating the effects of design parameters on the electromotive force may be different.

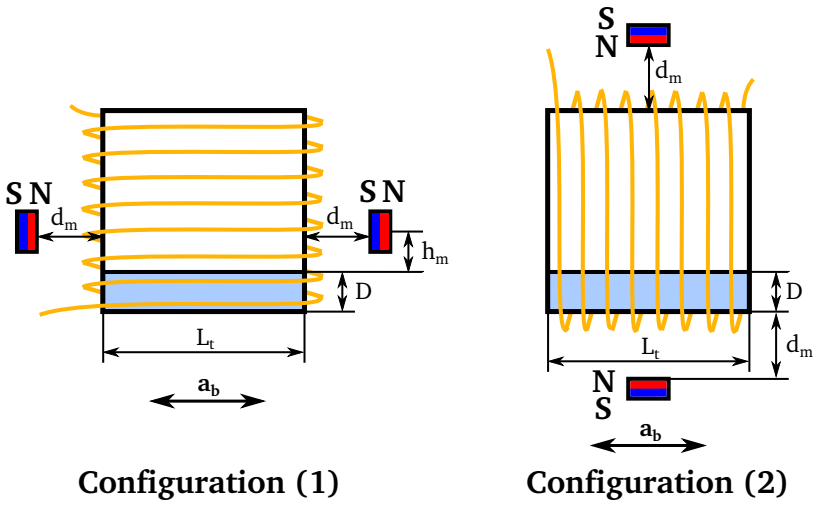

Figure 3.1: Schematic diagrams showing the two configurations of ferrofluid based energy harvesters analyzed in this chapter.

Parameters to be analyzed are divided into two groups: (1) device design parameters and material properties related to the magnetic flux in the tank and ferrofluid, including the tank-magnet distance d_m, the vertical distance from the ferrofluid surface to the magnets h_m, and the ferrofluid susceptibility χ, and (2) device design parameters and material properties related to the sloshing dynamics of the ferrofluid, including the tank length L_t, ferrofluid level D, base excitation amplitude a_0, and ferrofluid material properties such as viscosity η, density ρ, and surface tension coefficient σ. The device's geometric design

Table 3.1: Default values of the design parameters

Parameter	Default value	Parameter	Default value	Parameter	Default value
d_m	4 cm	L_t	12.7 cm	η	12 mPa·s
h_m	2.5 cm	D	2.5 cm	σ	24.15 mN/m
χ	3.52	a_0	0.5 m/s^2	ρ	1420 kg/m^3

parameters are shown in Fig. 3.1. When investigating the effect of a certain parameter, only the parameter of interest is varied and all the other parameters are set at their default values used in the original setup. The default values of the parameters are summarized in Table 3.1. The tank height (y direction) and width (z direction) are kept at 12.7 cm. Note that, unless further explained, the investigated material property values cover their practical ranges for most commercial ferrofluids. In this chapter, to illustrate the effects of these design parameters, the tank wall and coil thickness are neglected, and the numerical integrations in Eqs. (2.14-2.17) are performed only inside the tank. For all simulations, the size of the computational domain is set to be 10 times the size of the tank and magnets. In the numerical study on tank length, the interior mesh varies from 16×80 to 128×80 depending on the size of the tank. In all the other studies, 80×80 rectangular elements are used inside the tank.

3.1 Results and Discussion

3.1.1 Effects of magnetic flux-related parameters

The flux-related design parameters considered in this section are the distance between the magnets and the tank d_m, the vertical distance from the ferrofluid surface to the magnets h_m, and the ferrofluid susceptibility χ. While these parameters all influence ferrofluid sloshing to a certain extent by contributing to the magnetic body force on the right

hand side of the Navier-Stokes equations Eq. (2.20), their effects on the magnetic flux are direct and more important.

3.1.1.1 Distance from tank to magnets d_m

In this section, the distance between the magnets and the tank, d_m, is adjusted to alter the magnetic field in the tank. Simulation results indicate that varying d_m does not change the magnetic field pattern. However, the intensity of $\mathbf{H}$ is directly affected by the variation of d_m. In this study, the maximum and minimum d_m values are set to be 7 cm and 1 cm, respectively.

The effect of tank-magnet distance, d_m, on the electromotive force ε for Config. (1) is shown in Fig. 3.2. Three snapshots of magnetic flux lines and fluid flow in motion are also shown in Fig. 3.3. For each value of d_m the maximum electromotive force occurs at the resonant frequency of the sloshing column which is evident by the large peaks in the frequency response curves shown in Fig. 3.2a. Figure 3.2c shows when d_m is in the range of 4-7 cm, the ε-frequency curves exhibit peaks at similar frequencies. When d_m is reduced below 4 cm, however, the peak starts to shift to lower frequencies. The decrease in the resonant frequency is also shown clearly when comparing the fluid flow snapshots at the same instant (simulation time). When the ferrofluid is already on its way coming back to the right in Fig. 3.3c ($d_m = 7$cm), it just reaches the left highest point in Fig. 3.3b ($d_m = 2$cm).

The shift in the resonance peak at smaller tank-magnet distances results from the stronger magnetic force offsetting the effect of gravitational force on sloshing. Note that, in the absence of the external magnetic field, the analytical solution of the undamped modal frequencies of a small-amplitude sloshing with a slipping contact line is given as [79]

$$\omega_i^2 = \left(g k_i + \frac{\sigma}{\rho} k_i^3 \right) \tanh(k_i D), \qquad k_i = \frac{i\pi}{L_t}, \qquad i = 1, 2, 3... \tag{3.1}$$

where i is the mode number. Since the resonant frequency is intrinsically related to the modal frequency, it is apparent from Eq. (3.1) that the magnitude of g is positively correlated to the resonant frequency. However, when d_m becomes smaller, the magnetic field exerts a larger upward force on the ferrofluid, which leads to a smaller effective gravity and thus a smaller resonant frequency than the original value.

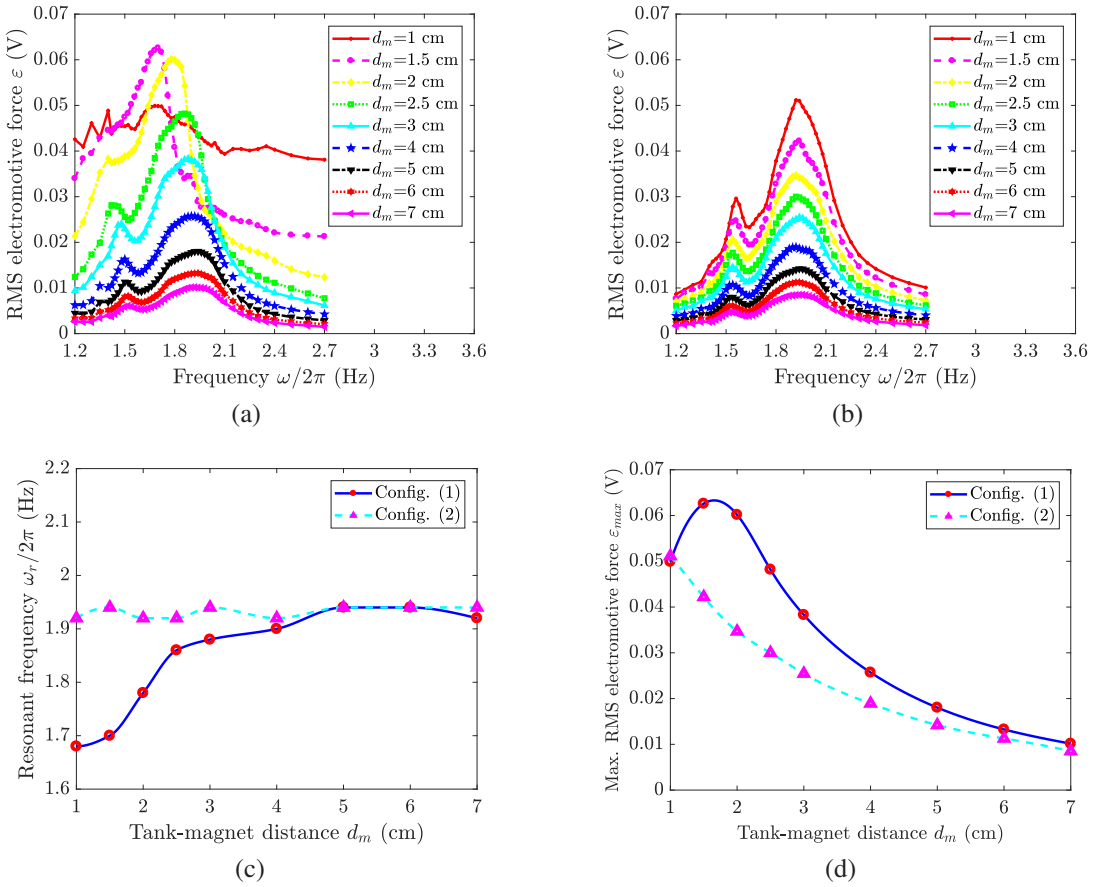

Figure 3.2: Effect of distance from tank to magnets on electromotive force for (a) Config. (1) and (b) Config. (2). Variations of resonant frequency and maximum electromotive force as functions of tank-magnet distance for both configurations are shown in (c) and (d).

Figure 3.2d shows that the maximum electromotive force ε_{max} continuously increases when d_m is reduced from 7 cm to 1.65 cm, but starts to decrease when d_m is reduced below 1.65 cm. The increasing trend in ε_{max} as d_m decreases is due to the increase in $\mathbf{H}$ as the magnets are placed closer to the tank. This is evident by the increasing number

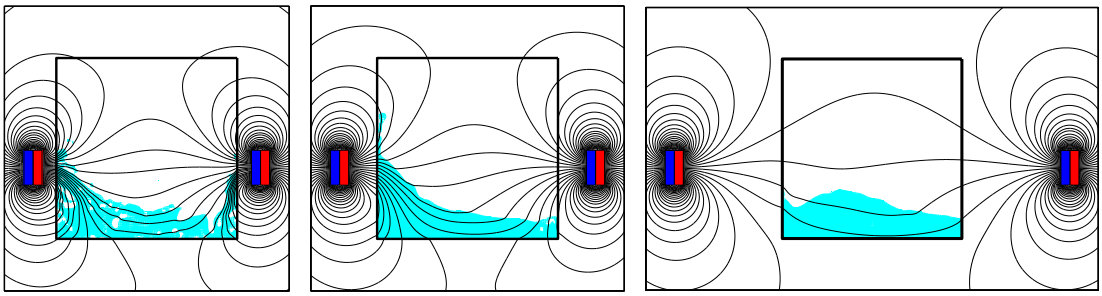

(a) (b) (c)

Figure 3.3: Magnetic flux lines and fluid flow snapshots at $t = 4.85$ s for Config. (1) with base excitation frequency of 1.82 Hz and tank-magnet distance: (a) $d_m = 1$ cm, (b) $d_m = 2$ cm and (c) d_m = 7 cm.

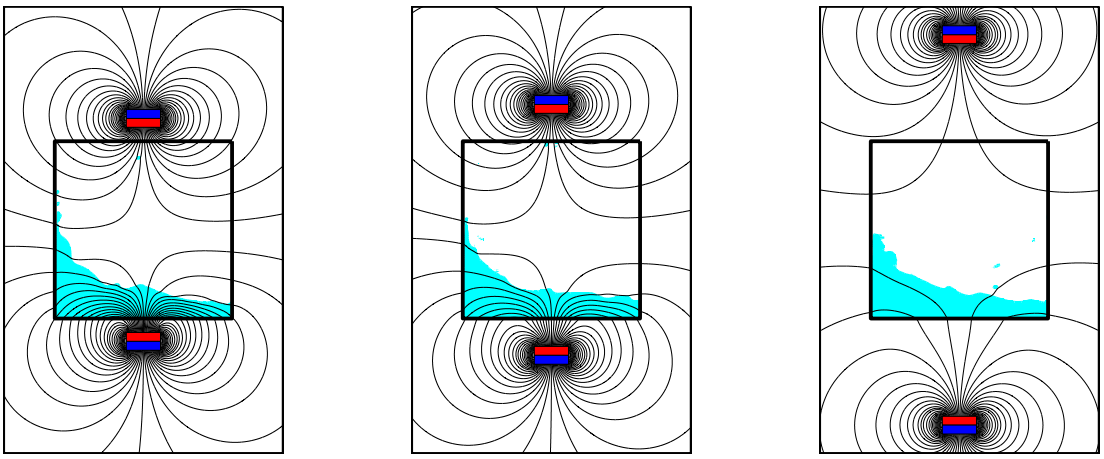

(a) (b) (c)

Figure 3.4: Magnetic flux lines and fluid flow snapshots at $t = 6.04$ s for Config. (2) with base excitation frequency of 1.94 Hz and tank-magnet distance: (a) $d_m = 1$ cm, (b) $d_m = 2$ cm and (c) d_m = 7 cm.

of magnetic flux lines going through the ferrofluid when comparing Figs. 3.3b and 3.3c. A larger $\mathbf{H}$ leads to a larger $\mathbf{M}$ in the ferrofluid, and consequently larger $\mathbf{B}$ and ε. However, when d_m is reduced below 1.65 cm, as shown in Fig. 3.3a, the ferrofluid starts to cling to the side walls of the tank and sloshing becomes more difficult, resulting in a smaller ε.

The effect of d_m on ε and ferrofluid sloshing for Config. (2) is shown in Figs. 3.2 and 3.4, respectively. It is shown in Fig. 3.2d that when d_m reduces, ε_{max} increases

monotonically. When compared to Config. (1), the peak in ε shifts only slightly as shown in Fig. 3.2c. This is consistent with Fig. 3.4 where all the three fluid flow snapshots show similar free surface profiles in spite of the different d_m values. Such behavior can be attributed to the relatively small magnetic force due to the larger distance from the magnets to the ferrofluid surface. Even when d_m reduces to 1 cm, the ferrofluid surface is still at least 2-3 cm away from the bottom magnet and far away from the top magnet. In this case, the magnetic force only plays a small role in the ferrofluid sloshing compared to the gravitational force. Therefore, the increase of $\mathbf{H}$ due to decrease of d_m leads to a monotonically increasing ε_{max} and a small peak shift. The results obtained for both configurations suggest that, to obtain the highest ε, ferrite magnets of the specific size should be placed around 1.65 cm away from the sloshing ferrofluid surface if possible.

3.1.1.2 Vertical distance from ferrofluid surface to magnets h_m

Another way to change the position of the magnets is to move them vertically in Config. (1). The effect of the vertical distance, h_m, from the ferrofluid surface to the magnets on the electromotive force ε is shown in Fig. 3.5. Twelve h_m values were used in the simulations and shown in Figs. 3.5b and 3.5c. Note that only five ε-frequency curves are shown in Fig. 3.5a for clarity. The resonant frequency shift due to the changing h_m is fairly small as shown in Fig. 3.5b since the magnets are at least 4 cm away from the ferrofluid in all cases. Figure 3.5c illustrates that ε_{max} increases as h_m is increased from -4 cm to -2.93 cm, then it decreases as h_m is increased within [-2.93 cm, 0.30 cm]. The trend reverses and ε_{max} increases again as h_m increases from 0.30 cm to 4.28 cm, then decreases again in the range between 4.28 cm and 6 cm.

The reasons for this trend can be explained by inspecting the magnetic flux lines shown in Fig. 3.6. As shown in Fig. 3.6a, when h_m = -3 cm, the y-component of $\mathbf{H}$, H_y, in the left half of the ferrofluid is always positive (pointing upwards), whereas H_y is

always negative in the right half (pointing downwards). This guarantees a monotonically changing B_y when the ferrofluid goes from left to right and vice versa, leading to a large ε. In the case of $h_m = 0$ cm, the magnetic flux lines have a different pattern. Figure 3.6b shows that there are both upward and downward magnetic flux lines passing through the ferrofluid body no matter which direction it sloshes toward. The cancellation between the upward and downward magnetic fluxes lowers ε.

The situation of $h_m = 4$ cm shown in Fig. 3.6c is similar to the $h_m =$ -3 cm case: B_y also changes monotonically with the ferrofluid sloshing from one side to the other since H_y is again unidirectional on either the left or right side. The difference between the two cases lies in that, at $h_m = 4$ cm, the magnetic field **H** going through the moving wave crest is stronger than that in the $h_m =$ -3 cm case. For this reason, ε at $h_m = 4$ cm is higher. Finally, when magnets are far away from the ferrofluid surface, i.e. $h_m <$ -2.93 cm or $h_m >$ 4.28 cm, **H** becomes smaller, leading to a smaller ε. From these results, it can be concluded that in the design process of the energy harvester, the magnets should be placed above the ferrofluid surface at an optimal height determined by the sloshing amplitude.

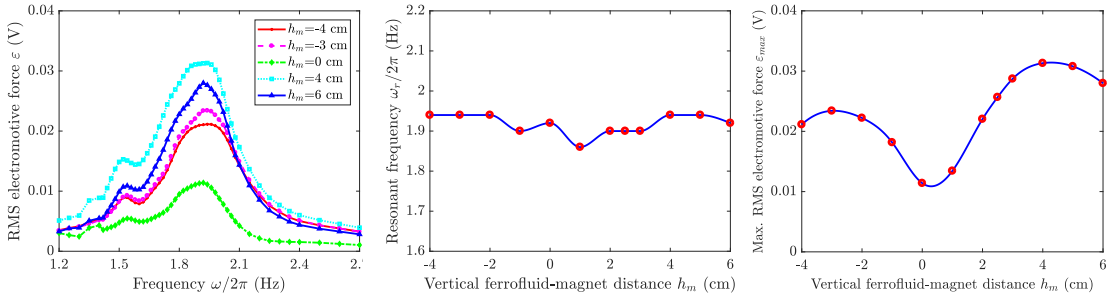

(a) (b) (c)

Figure 3.5: (a) Effect of the vertical distance between the ferrofluid surface and magnets on electromotive force for Config. (1). Variations of resonant frequency and maximum electromotive force as functions of vertical ferrofluid-magnet distance for Config. (1) are shown in (b) and (c).

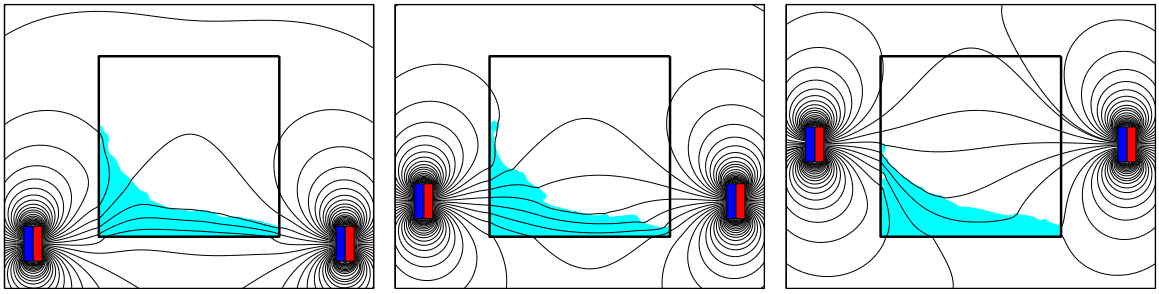

(a) (b) (c)

Figure 3.6: Magnetic flux lines and fluid flow snapshots at $t = 5.60$ s for Config. (1) with base excitation frequency of 1.94 Hz and vertical fluid-magnet distance: (a) h_m = -3 cm, (b) $h_m = 0$ cm and (c) h_m = 4 cm.

3.1.1.3 Magnetic susceptibility χ of the ferrofluid

Another significant parameter affecting the magnetic flux is the magnetic susceptibility, χ, of the ferrofluid. Figure 3.7c shows little resonant frequency shift. Figure 3.7d shows that, increasing χ causes a monotonic increase in ε_{max}. This is expected since ε is proportional to the change of magnetic flux and positively-correlated to the integration of $\mathbf{M}$ in the ferrofluid which is linearly proportional to χ. If $\mathbf{H}$ was assumed to be constant with increasing χ, the ε_{max}-χ relation would be linear. Nonetheless, since this is not the case, the slope of ε_{max} reduces as χ rises. The sub-linear variation of ε_{max} can be understood by the following weak form of the magnetic scalar potential equation Eq. (2.26) combined with Eq. (2.29)

$$\int_{\Omega} \nabla\delta\psi \cdot \nabla\psi d\Omega + \int_{\Omega_{liq}} \nabla\delta\psi \cdot \frac{f\chi}{1+(1-f)\chi} \nabla\psi d\Omega = \int_{\Omega_{mag}} \nabla\delta\psi \cdot \frac{1}{\mu_0}\mathbf{B}_0 d\Omega + \int_{\Gamma} \delta\psi \frac{\partial\psi}{\partial\mathbf{n}} d\Gamma \tag{3.2}$$

Since the right hand side of Eq. (3.2) does not vary with χ, increasing χ results in decreasing of $\nabla\psi$ on the left hand side, i.e. decreasing magnitude of $\mathbf{H}$ according to Eq. (2.4). Therefore, ε_{max}-χ relation should be sub-linear. It is also observed that the saturation value for χ in Config. (2) is around 7.04, much smaller than that in Config. (1).

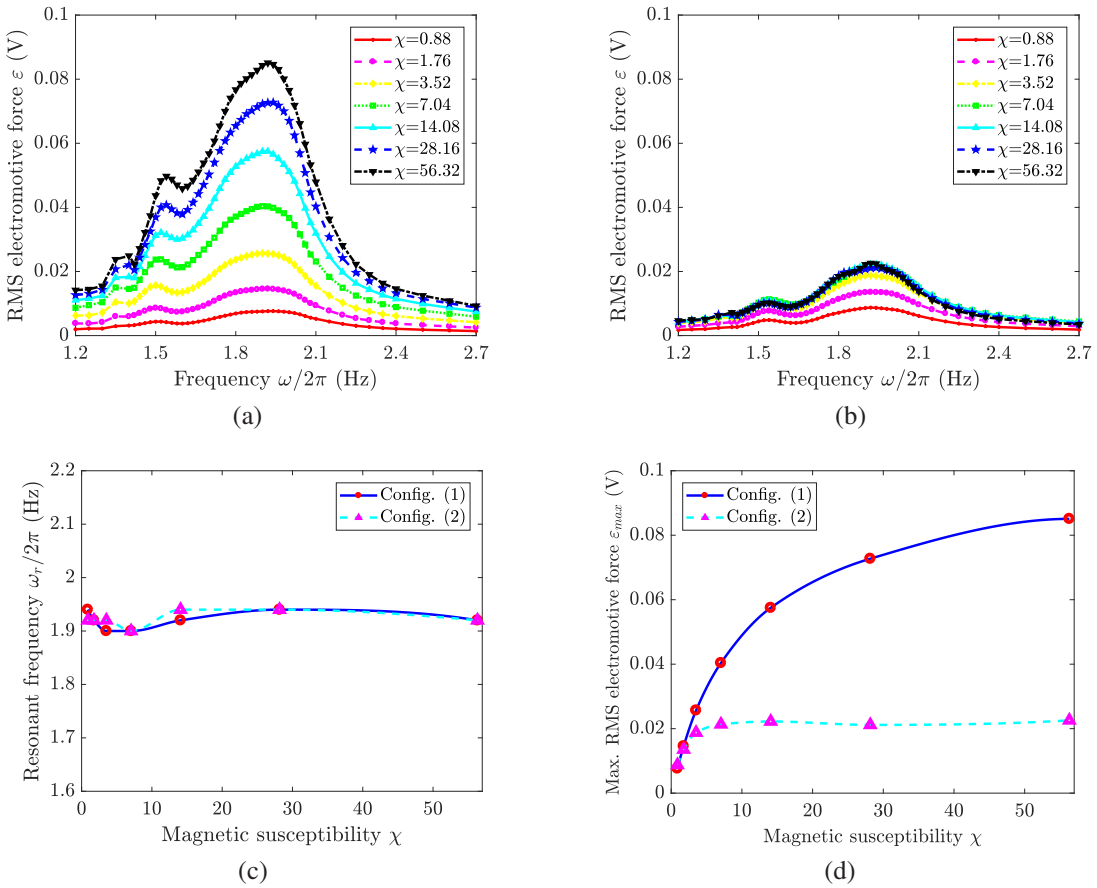

Figure 3.7: Effect of ferrofluid susceptibility on electromotive force for (a) Config. (1) and (b) Config. (2). Variations of resonant frequency and maximum electromotive force as functions of ferrofluid susceptibility for both configurations are shown in (c) and (d).

3.1.2 Effects of sloshing-related parameters

In addition to the parameters altering the magnetic flux, the design parameters that determine the ferrofluid sloshing behavior can also indirectly influence the magnetization distribution. It is obvious that the tank length L_t, ferrofluid level D and base excitation amplitude a_0 can largely affect the sloshing behavior. Furthermore, three ferrofluid material properties, namely the viscosity η, surface tension coefficient σ and density ρ are also important since they are closely related to the viscous force, surface tension, gravity and horizontal excitation force, respectively. These forces either reinforce or compete with the

magnetic force on the right hand side of the Navier-Stokes equations Eq. (2.20), and thus influence the sloshing dynamics of the ferrofluid. Therefore, they are investigated in this section.

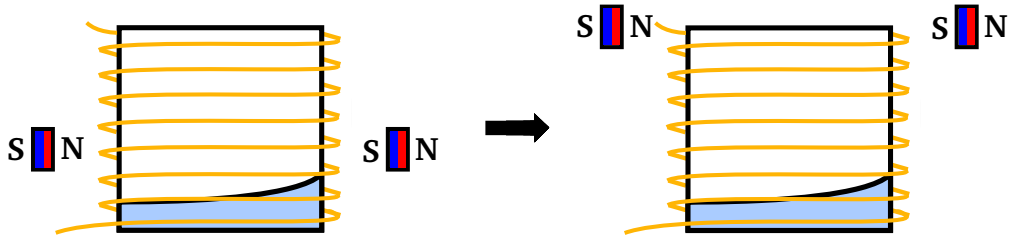

Figure 3.8: Adjusted Config. (1).

The simulation setup for Config. (1) is adjusted in this section for more consistent evaluation of the effects of sloshing-related parameters. When $h_m = 2.5$ cm in the original setup, ferrofluid may slosh over and under the centers of magnets as depicted in Figs. 3.3a and 3.3b. In some cases, therefore, the performance variation would be the result of the combined effects of the magnet position and the sloshing-related parameters. To eliminate the inconsistent magnet position effect from case to case and focus only on the effects of sloshing-related parameters, the two magnets are moved up to $h_m = 10.2$ cm as shown in Fig. 3.8. At that position, the centers of the magnets are aligned with the tank top edge, which ensures a unidirectional H_y along the y direction in the entire tank similar to the situation shown in Fig. 3.6c. For Config. (2), since H_x distribution is always unidirectional along the y direction, no further adjustment of magnet position is made.

3.1.2.1 Tank length L_t

The tank length, L_t, is varied from 2.54 cm to 20.32 cm to investigate its effect on ε. It is observed in Figs. 3.9a and 3.9b that both configurations give very similar resonant frequency and ε_{max} trends. When L_t increases, resonance rapidly shifts to a lower

frequency as shown in Fig. 3.9c. For Config. (1), as shown in Fig. 3.9d, it is observed that the ε_{max}-L_t curve contains three stages: (1) small for $L_t < 5$ cm, (2) increasing rapidly between $L_t > 5$ cm and $L_t < 10$ cm, and (3) increasing slowly after $L_t > 10$ cm. The slope of ε_{max}-L_t curve reflects the combined influence of the sloshing amplitude and the intensity of H_y along the vertical direction. In the first stage, the amplitude of sloshing and $\mathbf{H}$ are both very small, leading to the initial low ε_{max}. Simulation results show that sloshing amplitude increases rapidly for 5 cm $< L_t <$ 10 cm and then the rise slows down with increasing L_t. This behavior determines the characteristics of ε_{max}-L_t slope in the second and third stages.

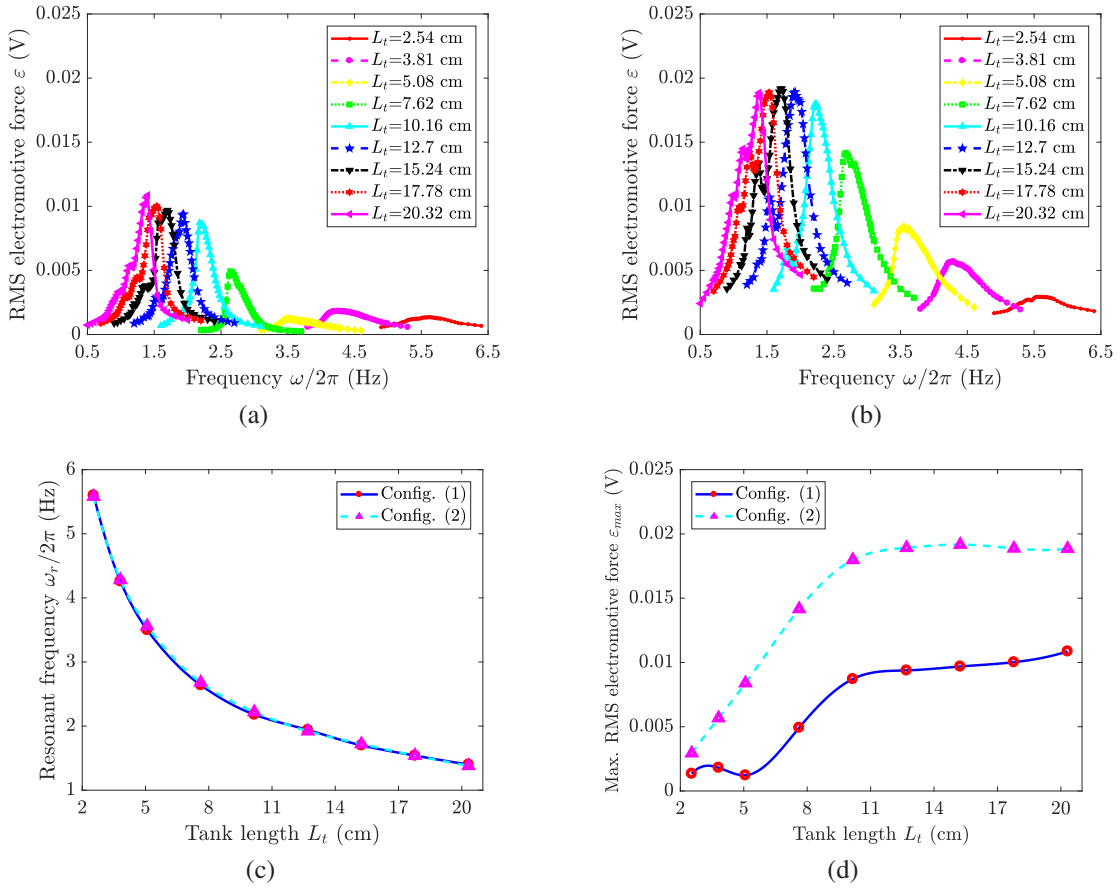

Figure 3.9: Effect of tank length on electromotive force for (a) Config. (1) and (b) Config. (2). Variations of resonant frequency and maximum electromotive force as functions of tank length for both configurations are shown in (c) and (d).

In Config. (2), the ε_{max}-L_t curve exhibits a similar trend as in Config. (1) except for very small L_t. The faster ε_{max} increase in Config. (2) is due to the different magnetic field distribution. At small L_t, ferrofluid surface elevation is very small and it mainly sloshes close to the bottom of the tank given the specific ferrofluid level. This region has high-intensity H_x due to the magnet below the tank. Therefore, when L_t increases, ε_{max} increases steadily in the first and second stages. For both configurations, the optimal tank length is around 10 cm, which can lead to a high ε without greatly increasing the tank size. The resonant frequency can also be adjusted effectively by changing the tank length.

3.1.2.2 Ferrofluid level D

The ferrofluid level in the tank, D, is varied from 1.27 cm to 11.43 cm and its effect on the electromotive force is shown in Fig. 3.10. Nine different values of D for each configuration were studied, but only six of those are shown in Figs. 3.10a and 3.10b for clear illustration. In Config. (1), ε_{max} is very small for small D, but rises quickly to the maximum value 0.082 V at $D = 8.83$ cm, and then decreases. The initial small ε_{max} is caused by the small amount of ferrofluid in the tank, as well as the low $\mathbf{H}$ due to the magnets being faraway from the surface. Subsequently, ε_{max} starts to increase with increasing D since both of the surface elevation and $\mathbf{H}$ increase. Eventually, ε_{max} decreases at large D because sloshing is confined by the remaining small empty space in the tank. This result shows that the ferrofluid level is a crucial factor in optimizing the electromotive force, and the optimal ferrofluid level for Config. (1) is around 9 cm for the energy harvester.

In Config. (2), Fig. 3.10d reveals that ε_{max} bears an almost steady value except when D is either very small or very large. The small values of ε_{max} for the two extreme values of D are due to the small amount of ferrofluid and restricted sloshing in limited empty space, respectively. The steady result is caused by the combination of two factors: the amplitude of sloshing and the distribution of H_x. While the sloshing amplitude reaches its

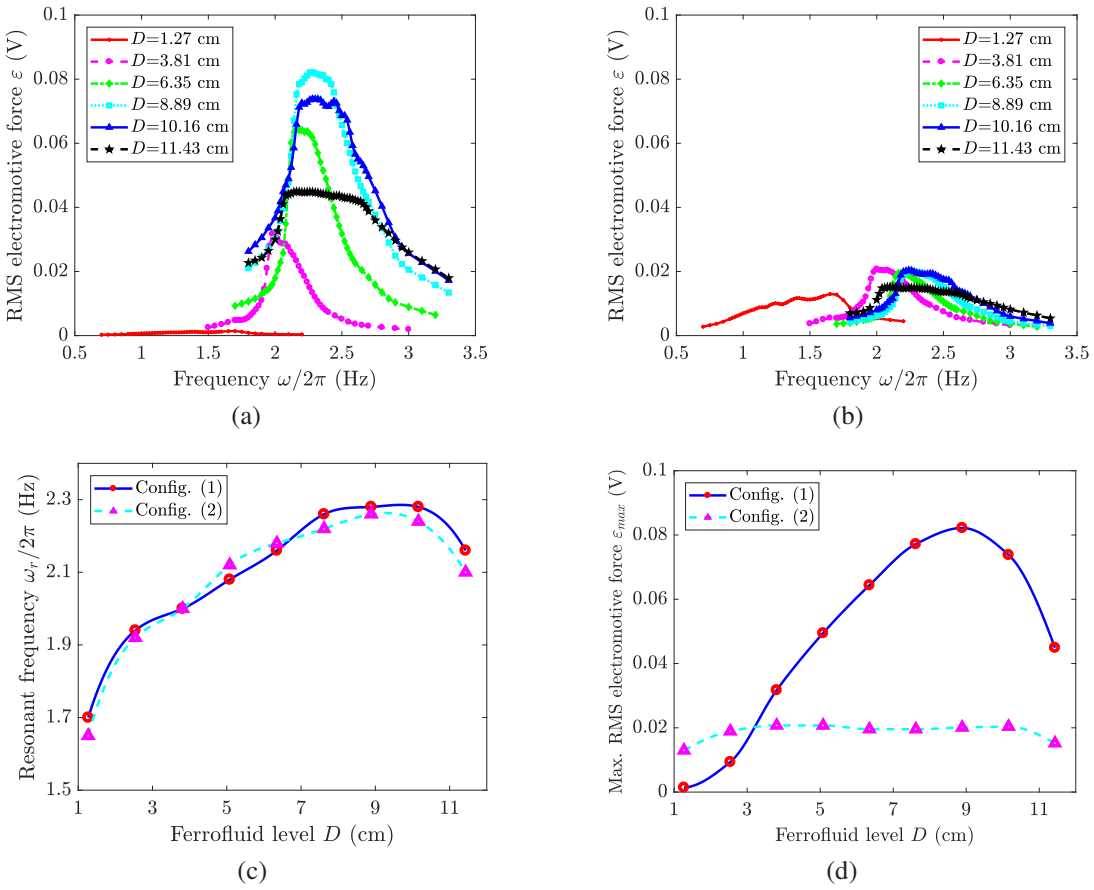

Figure 3.10: Effect of ferrofluid level on electromotive force for (a) Config. (1) and (b) Config. (2). Variations of resonant frequency and maximum electromotive force as functions of ferrofluid level for both configurations are shown in (c) and (d).

maximum value when the tank is around half full, H_x is larger closer to the top and bottom of the tank, and smaller near the vertical center. Therefore, over the entire D range, sloshing and H_x undergo alternate increases and decreases, producing a fairly steady ε. Comparison of Figs. 3.10a and 3.10b demonstrates that the electromotive force is highly sensitive to the placement of magnets. In addition, for both configurations, it is shown in Fig. 3.10c that when D increases, the resonance moves to a higher frequency. At $D = 11.43$ cm, however, the ε-frequency curve greatly bends to the left and the resonance frequency drops. Thus, different from the monotonically increasing resonant frequency obtained from Eq. (3.1), the confinement of sloshing at high D reduces the resonant frequency.

3.1.2.3 Amplitude of the input acceleration a_0

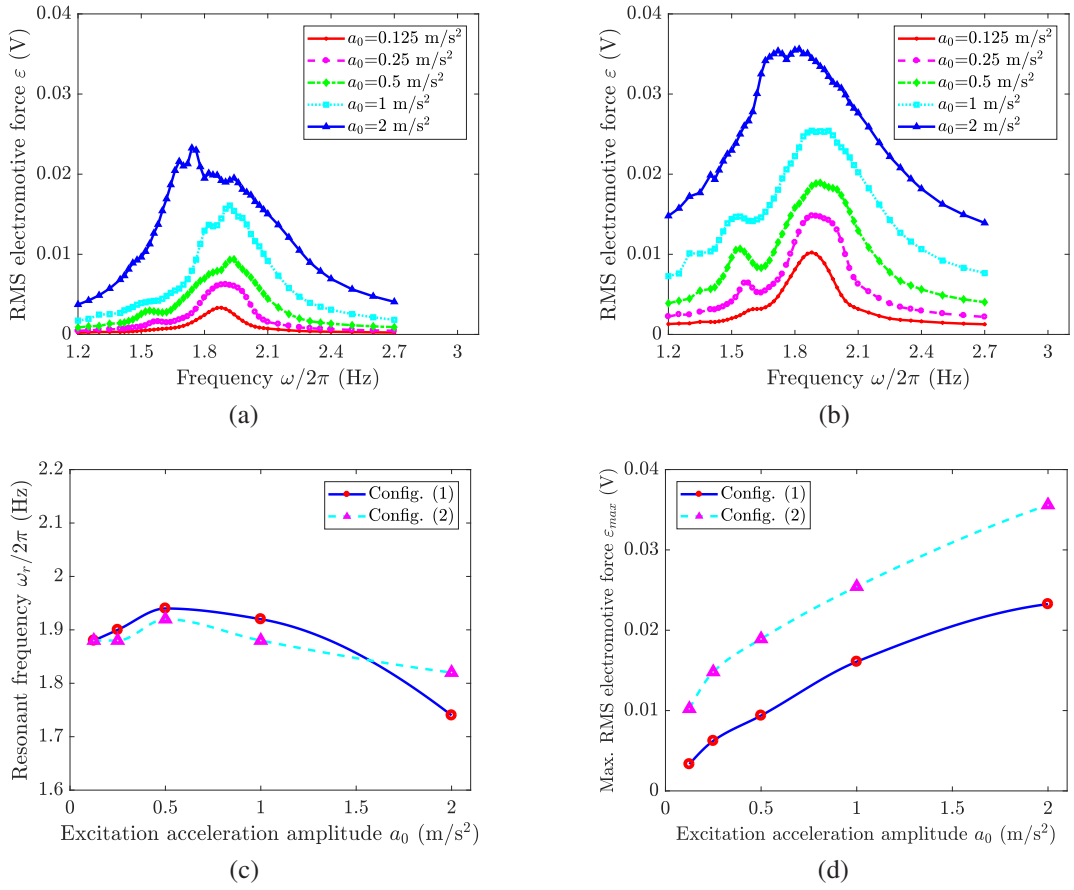

Figure 3.11: Effect of the base acceleration amplitude on the electromotive force for (a) Config. (1) and (b) Config. (2). Variations of resonant frequency and maximum electromotive force as functions of base acceleration amplitude for both configurations are shown in (c) and (d).

The effect of the acceleration amplitude, a_0, on the electromotive force ε is shown in Fig. 3.11. It is evident that, ε_{max} increases monotonically as the acceleration is increased in both configurations. This is due to the fact that, at larger values of a_0, the amplitude of the sloshing motion increases, which leads to a larger change in the magnetic flux during a sloshing cycle and consequently larger ε_{max}. Furthermore, due to the nonlinear softening sloshing behavior of the fluid column, the ε-frequency response curve bends to the left as the amplitude of the excitation increases to 2 m/s^2 as shown in Figs. 3.11a and 3.11b. At

such a large acceleration level, the possibility of wave breaking at high sloshing magnitudes increases and spilling of drops and lumps of ferrofluid interferes with the bulk flow [80, 81]. This has the influence of producing aperiodic responses which are evident in the non-smooth nature of the curves near the peak frequency.

3.1.2.4 Ferrofluid viscosity η

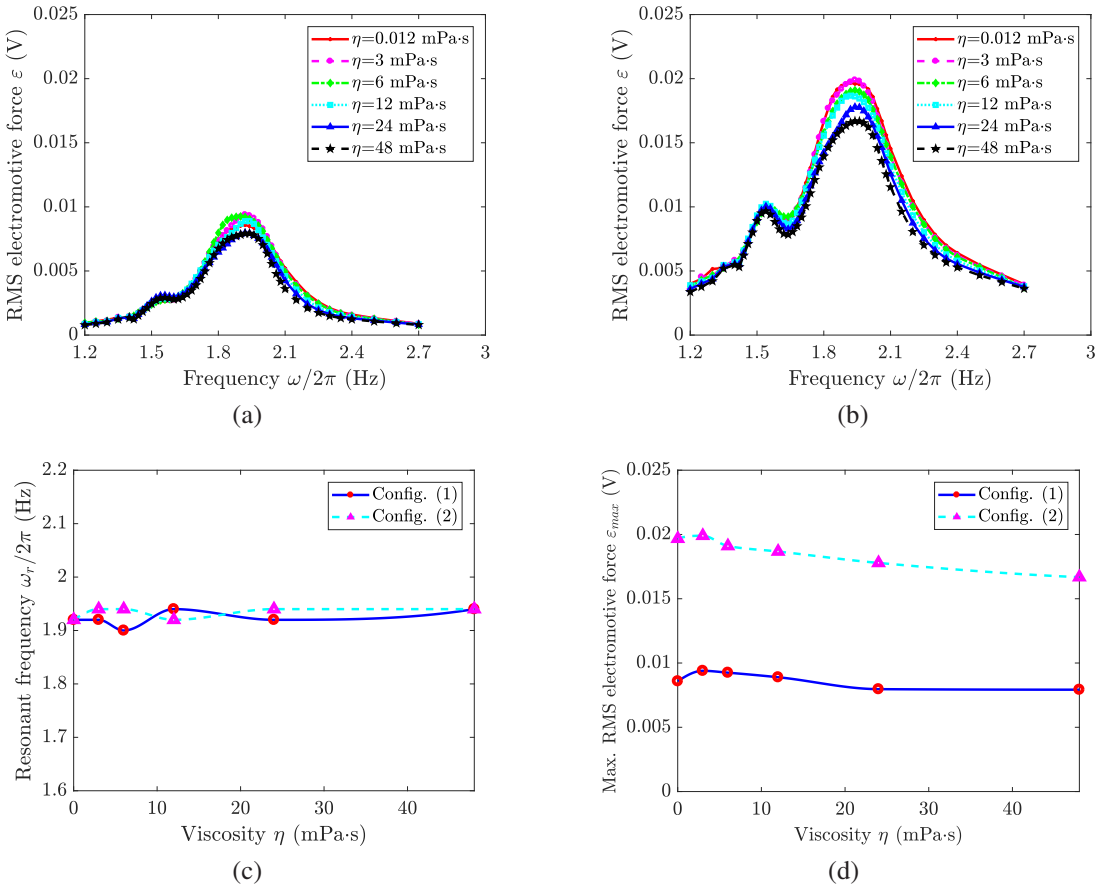

Figure 3.12: Effect of ferrofluid viscosity on electromotive force for (a) Config. (1) and (b) Config. (2). Variations of resonant frequency and maximum electromotive force as functions of ferrofluid viscosity for both configurations are shown in (c) and (d).

The effect of ferrofluid viscosity, η, on the electromotive force ε is shown in Fig. 3.12. Numerical results show that, in the investigated range [0.012 mPa·s, 48 mPa·s], for both configurations, viscosity has little effect on the resonant frequency, but lower viscosity

leads to a slightly higher ε. Higher values of η make the ferrofluid more viscous and, hence, sloshing becomes slightly more difficult. This leads to slightly smaller ε values. Although viscosity of some commercial ferrofluids for sealing applications can go up to thousands of times of the default value of η, high η values would only largely reduce the electromotive force, which is obviously not desired for performance optimization of the energy harvester. Therefore, ferrofluids with extremely high viscosity are not studied here.

3.1.2.5 Surface tension coefficient σ

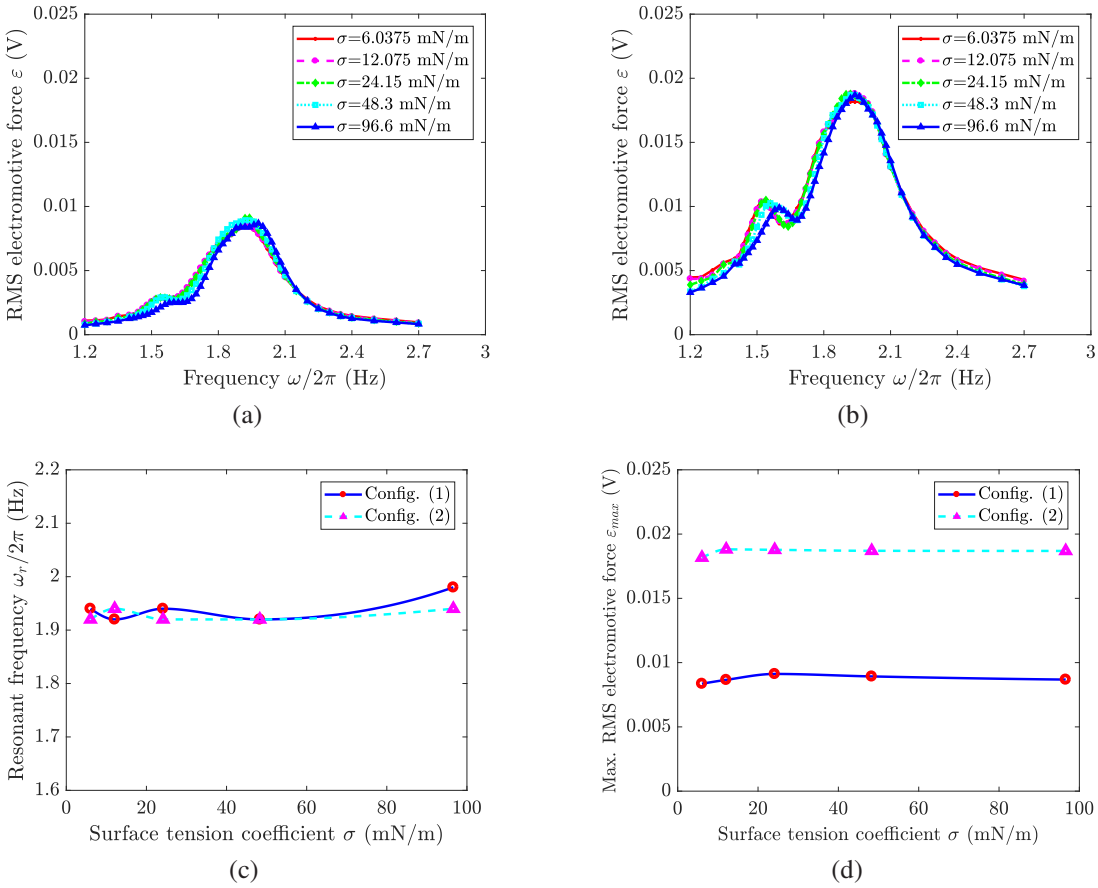

Figure 3.13: Effect of surface tension coefficient on electromotive force for (a) Config. (1) and (b) Config. (2). Variations of resonant frequency and maximum electromotive force as functions of surface tension coefficient for both configurations are shown in (c) and (d).

Figure 3.13 shows that surface tension coefficient, σ, has a negligible influence on

ε in both configurations. When σ increases, the downward surface tension force at the sloshing surface increases, leading to a larger resonant frequency according to Eq. (3.1). This causes the resonance peak to shift slightly to the right.

3.1.2.6 Ferrofluid density ρ

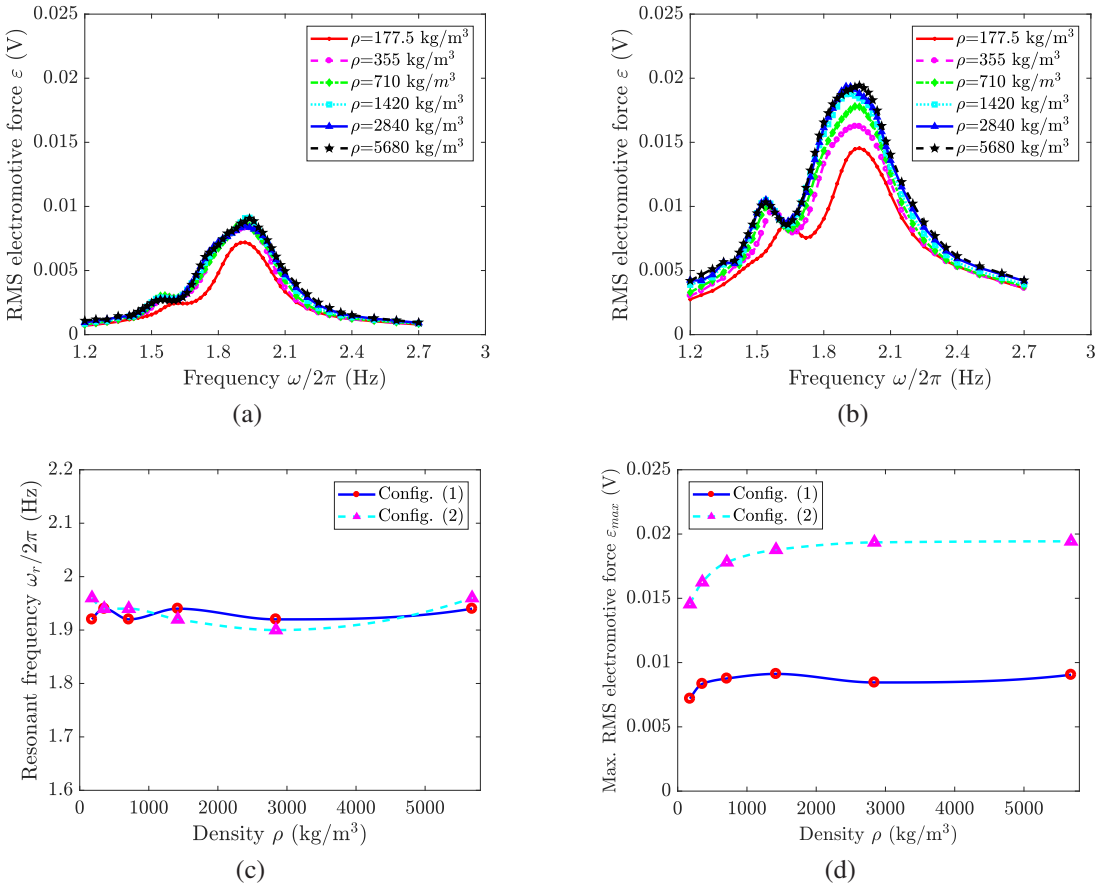

Figure 3.14: Effect of ferrofluid density on electromotive force for (a) Config. (1) and (b) Config. (2). Variations of resonant frequency and maximum electromotive force as functions of ferrofluid density for both configurations are shown in (c) and (d).

The effect of the ferrofluid density, ρ, on ε is investigated in Fig. 3.14. For both configurations, the resonance peak only shifts slightly. At very small values of ρ, the influences of gravity and the excitation force become less prevalent when compared to those of

viscous force, magnetic force and surface tension. The latter three forces slightly suppress the sloshing motion which eventually leads to a smaller ε_{max}.

Chapter 4

Molecular Dynamics Analysis of Magnetization and Microscopic Behavior of Ferrofluid

Ferrofluid is a colloidal suspension of small magnetic, single-domain particles dispersed in a water or organic carrier liquid [58]. To prevent aggregation of the ferromagnetic nanoparticles, particles are stabilized either sterically by being coated with long-chain surfactant or electrostatically by including charged groups. As a result, particles interact with each other by the anisotropic long-range magnetic dipole-dipole potential as well as the electrostatic monopolar interaction or the short-range symmetric potentials. Experiments [82–86], theories [87–96] and simulations [97–112] have revealed that, due to these interactions, various aggregates, such as chains, rings, branched structures and networks, can be formed. This influences the macroscopic properties of ferrofluid, such as the effective viscosity and magnetization.

Continuum level computational analysis of the energy harvester in Chapter 3 reveals that the magnetic susceptibility/magnetization of ferrofluid greatly influences the perfor-

mance of the energy harvester. In addition, since the ferrofluid in the energy harvester undergoes sloshing motion under external mechanical excitations, it is expected that fluid motion would significantly influence the aggregation behavior of the nanoparticles, thereby playing an important role in determining the ferrofluid properties. Therefore, it is critical to understand the relation between the dynamic microstructural behavior of the ferrofluid and its associated macroscopic magnetization.

Magnetic aggregates are also affected by the polydispersity of ferrofluid. Particles in commercially available ferrofluids typically have various sizes, with a mean magnetic core diameter of around 10 nm. Since the dipole moment of a particle is proportional to the magnetic core volume, large particles with a typical size of 15-20 nm have much higher dipole-dipole interaction energy than the thermal energy at room temperature and can aggregate into different structures [100]. In addition, large particles also rotate more easily at low magnetic field strengths compared to smaller particles. They strongly enhance the effective viscosity at small flow velocity gradients and magnetization in weak fields. Therefore, a ferrofluid system having large particles behaves differently from a monodisperse small-particle system in terms of microscopic structures and macroscopic properties [86, 100, 113–115]. In the literature, a polydisperse ferrofluid is typically modeled as a bidisperse system consisting of two fractions of magnetic particles with significantly different diameters.

However, most research studies on the magnetization of ferrofluid systems only dealt with the equilibrium situations [99, 100, 115–117]. Some studies included flow conditions but only considered weakly interacting systems [118, 119], zero magnetic field [120], or single-particle formulation (ignored all dipolar and flow-induced interactions) [121]. To the best of the authors' knowledge, non-equilibrium/dynamic aggregation behavior and associated magnetization of ferrofluid systems with strong dipolar potentials under shear flow conditions have not been studied at the molecular level.

In this chapter, a non-equilibrium molecular dynamics (NEMD) study is performed to obtain an understanding of the dynamic magnetization and microscopic structures of ferrofluid systems containing small and large particles under the influence of both magnetic field and shear flow. The computational model considers both long-range dipolar interaction and short-range repulsive interaction of the ferromagnetic nanoparticles. The factors investigated include solvent friction coefficients, particle size, magnetic field strength and direction, and shear rate.

4.1 Molecular Dynamics Model

A bidisperse ferrofluid system consisting of N spherical particles of two different sizes distributed in a cubic simulation box of dimension L is considered in this model. When the number of particles of either size is set as zero, the system reverts to a monodisperse system. Periodic boundary conditions are assumed along all directions. A ferrofluid particle can be regarded as a single magnetic domain with a diameter σ_i and a permanent dipole moment $\mathbf{m}_i$ fixed at its center. The long-range dipole-dipole potential takes the form [99]

$$U_{ij}^{dip} = \frac{\mu_0}{4\pi}\left[\frac{\mathbf{m}_i \cdot \mathbf{m}_j}{r_{ij}^3} - \frac{3(\mathbf{m}_i \cdot \mathbf{r}_{ij})(\mathbf{m}_j \cdot \mathbf{r}_{ij})}{r_{ij}^5}\right] \tag{4.1}$$

$$r_{ij} = |\mathbf{r}_{ij}| = |\mathbf{r}_i - \mathbf{r}_j| \tag{4.2}$$

where μ_0 is the permeability of free space, $\mathbf{r}_i$ the position vector of particle i, and $\mathbf{r}_{ij}$ the distance vector between two particles i and j. The dipole moment of a magnetic particle is proportional to its magnetic core volume as $m_i = M_d \pi \sigma_i^3/6$, where M_d is the bulk magnetization of the magnetic material and has a value of 4.46 $\times 10^5$ A/m for magnetite. The dipolar potential depends on both the interparticle distance $\mathbf{r}_{ij}$ and the orientations of

the two dipole moments. In addition to the dipolar potential, ferrofluid particles are also subjected to the short-range interaction potential. The potential may depend on whether this specific ferrofluid is sterically or electrically stabilized. In this work, the steric effect of the coating layer is approximated by the Lennard-Jones potential with a cutoff similar to that in Ref. [100]

$$U_{ij}^{lj} = 4\epsilon \left[\left(\frac{\sigma_i + \sigma_j}{2r_{ij}} \right)^{12} - \left(\frac{\sigma_i + \sigma_j}{2r_{ij}} \right)^{6} \right], \quad r_{ij} < r_c \tag{4.3}$$

where ϵ is the potential well depth. The cutoff radius r_c is taken as $2^{-5/6}(\sigma_i + \sigma_j)$, which makes the interaction force purely repulsive and smoothly decrease to zero at r_c.

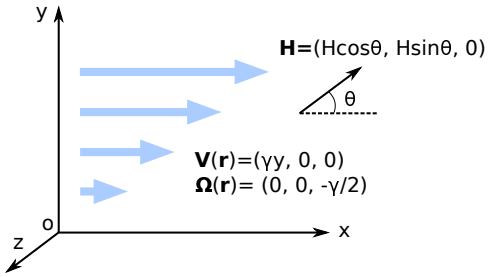

Figure 4.1: Schematic diagram showing the flow field and the magnetic field considered in the ferrofluid system.

The solvent of ferrofluid is not explicitly considered in this model. Instead, it is implicitly included through Langevin dynamics, which mimics the viscous damping and random bumping of the solvent by adding friction and Brownian effects to the equations of motion. Langevin dynamics can also control the system temperature like a thermostat. The system is placed in a flow field $\mathbf{V}(\mathbf{r})$ with a local vorticity $\mathbf{\Omega}(\mathbf{r}) = \frac{1}{2}\nabla \times \mathbf{V}(\mathbf{r})$, and a magnetic field $\mathbf{H} = (H\cos\theta,\, H\sin\theta,\, 0)$ as shown in Fig. 4.1. The flow field is set as a shear flow with a linear velocity profile $\mathbf{V}(\mathbf{r}) = (\gamma y,\, 0,\, 0)$, where γ is the shear rate. The

translational and rotational motions of particles are given as [118]

$$M_i \frac{d\mathbf{v}_i}{dt} = (\mathbf{F}_i^{dip} + \mathbf{F}_i^{lj}) - \Gamma_{Ti}[\mathbf{v}_i - \mathbf{V}(\mathbf{r}_i)] + \boldsymbol{\xi}_{Ti} \tag{4.4}$$

$$\mathbf{I}_i \cdot \frac{d\boldsymbol{\omega}_i}{dt} = \boldsymbol{\tau}_i^{dip} + \mu_0 \mathbf{m}_i \times \mathbf{H} - \Gamma_{Ri}[\boldsymbol{\omega}_i - \boldsymbol{\Omega}(\mathbf{r}_i)] + \boldsymbol{\xi}_{Ri} \tag{4.5}$$

where $\mathbf{v}_i$ and $\boldsymbol{\omega}_i$ are the translational and angular velocities of the particle, M_i and $\mathbf{I}_i$ the mass and moment of inertia tensor, $\mathbf{F}_i^{dip}$, $\mathbf{F}_i^{lj}$ and $\boldsymbol{\tau}_i^{dip}$ the forces and torque acting on the particle, $\boldsymbol{\xi}_{Ti}$ and $\boldsymbol{\xi}_{Ri}$ the uniform random force and torque with zero mean that satisfy the fluctuation/dissipation relations. The two terms $-\Gamma_{Ti}[\mathbf{v}_i - \mathbf{V}(\mathbf{r}_i)]$ and $-\Gamma_{Ri}[\boldsymbol{\omega}_i - \boldsymbol{\Omega}(\mathbf{r}_i)]$ represent the hydrodynamic drag, where Γ_{Ti} and Γ_{Ri} are the translational and rotational friction coefficients. For a sphere of diameter σ, $I = M\sigma^2/10$. When it is placed inside a solvent with viscosity η, the friction coefficients are given by

$$\Gamma_T = 3\pi\eta\sigma, \quad \Gamma_R = \pi\eta\sigma^3. \tag{4.6}$$

Taking the small particle diameter and mass as references, all variables can be written in dimensionless forms as:

$$r^* = \frac{r}{\sigma_s}, \quad M^* = \frac{M}{M_s}, \quad I^* = \frac{I}{M_s\sigma_s^2}, \quad t^* = t\sqrt{\frac{\epsilon}{M_s\sigma_s^2}}, \quad T^* = \frac{k_B T}{\epsilon} \tag{4.7}$$

$$m^* = m\sqrt{\frac{\mu_0}{4\pi\epsilon\sigma_s^3}}, \quad H^* = H\sqrt{\frac{4\pi\mu_0\sigma_s^3}{\epsilon}}, \quad F^* = \frac{F\sigma_s}{\epsilon}, \quad \tau^* = \frac{\tau}{\epsilon} \tag{4.8}$$

$$\Gamma_T^* = \Gamma_T\sqrt{\frac{\sigma_s^2}{M_s\epsilon}}, \quad \Gamma_R^* = \Gamma_R\sqrt{\frac{1}{M_s\sigma_s^2\epsilon}}, \quad \gamma^* = \gamma\sqrt{\frac{M_s\sigma_s^2}{\epsilon}} \tag{4.9}$$

where k_B is the Boltzmann constant and T the temperature. The dipole moment, mass and moment of inertia of large particles can be expressed in terms of those of small particles and their size ratio: $m_l = m_s(\sigma_l/\sigma_s)^3$, $M_l = M_s(\sigma_l/\sigma_s)^3$ and $I_l = I_s(\sigma_l/\sigma_s)^5$, respectively.

Then, Eqs. (4.4, 4.5) can be rewritten in dimensionless form as

$$M_i^* \frac{d\mathbf{v}_i^*}{dt^*} = (\mathbf{F}_i^{dip*} + \mathbf{F}_i^{lj*}) - \Gamma_{Ti}^*[\mathbf{v}_i^* - \mathbf{V}^*(\mathbf{r}_i^*)] + \boldsymbol{\xi}_{Ti}^* \tag{4.10}$$

$$\mathbf{I}_i^* \cdot \frac{d\boldsymbol{\omega}_i^*}{dt^*} = \boldsymbol{\tau}_i^{dip*} + \mathbf{m}_i^* \times \mathbf{H}^* - \Gamma_{Ri}^*[\boldsymbol{\omega}_i^* - \boldsymbol{\Omega}^*(\mathbf{r}_i^*)] + \boldsymbol{\xi}_{Ri}^* \tag{4.11}$$

Despite the difference in sizes and magnetic materials, the behavior of a bidisperse ferrofluid system can be characterized by the following dimensionless parameters: the volume fraction of particles ϕ, the dipolar coupling parameter λ and the Langevin parameter α:

$$\phi_s = \frac{N_s}{V}\frac{\pi\sigma_s^3}{6} = \frac{N_s}{V^*}\frac{\pi}{6}, \quad \phi_l = \frac{N_l}{V}\frac{\pi\sigma_l^3}{6} = \frac{N_l}{V^*}\frac{\pi\sigma_l^{*3}}{6}, \quad \phi = \phi_s + \phi_l \tag{4.12}$$

$$\lambda_s = \frac{\mu_0 m_s^2}{4\pi\sigma_s^3 k_B T} = \frac{m_s^{*2}}{T^*}, \quad \lambda_l = \frac{\mu_0 m_l^2}{4\pi\sigma_l^3 k_B T} = \lambda_s \sigma_l^{*3}, \quad \alpha = \mu_0 \frac{m_s H}{k_B T} = \frac{m_s^* H^*}{T^*} \tag{4.13}$$

where V is the total volume of the system. When ϕ_l varies from 0 to ϕ, the system goes from monodisperse of small particles ($\phi_l = 0$), to bidisperse ($0 < \phi_l < \phi$), and finally to monodisperse of large particles ($\phi_l = \phi$). The dipolar coupling parameter λ relates the minimum dipole-dipole interaction energy of two contacting particles to the thermal energy $k_B T$. If λ is on the order of one or smaller, the dipole-dipole interaction is too weak to cause any particle aggregation. The Langevin parameter α represents the ratio of the field-dipole energy to the thermal energy in the system. For a ferrofluid system at a given temperature, α is simply proportional to the magnetic field magnitude H.

The equilibrium or steady state magnetization is calculated through the sum of dipole moments divided by the system volume and then averaged over a certain period of time after the system establishes equilibrium or steady state

$$\mathbf{M} = \left\langle \frac{1}{V} \sum_{i=1}^{N} \mathbf{m}_i \right\rangle \tag{4.14}$$

where the angle brackets denote the time average.

In our simulations, ferrofluid aggregates are mainly chains and rings. Two particles are considered to be bound when their dipolar potential energy is less than the prescribed threshold $-1.5\lambda_s k_B T[2\sigma_i^*\sigma_j^*/(\sigma_i^*+\sigma_j^*)]^3$, i.e. 75% of the dipolar energy of two contacting and perfectly head-to-tail aligned dipoles [99, 100]. The size of a cluster is defined as the number of particles in that cluster, and the average cluster size is defined as

$$C_{avg} = \left\langle \frac{1}{N_c} \sum_{k=1}^{N_c} C_k \right\rangle \tag{4.15}$$

where k is the cluster index, N_c the number of clusters, and C_k the size of cluster k.

In this work, Eqs. (4.10, 4.11) are implemented in the LAMMPS package [122] and MD simulations are performed to study the bidisperse ferrofluid in the shear flow field. With periodic boundary conditions in all three directions, the dipole-dipole interaction is evaluated by the Ewald summation under metallic boundary condition. To apply a shear flow with a linear velocity profile, the initial orthogonal simulation box is tilted into a triclinic box at the shear strain rate γ and periodically flipped to an equivalent shape in the opposite direction. The root mean square (rms) absolute errors in the dipolar forces for the Ewald summation are fixed at $\Delta F^{dip} \leq 10^{-4} m_s^2 \mu_0/(4\pi\sigma_s^4)$, i.e. $\Delta F^{dip*} \leq 10^{-4} m_s^{*2}$. All simulations are started from initial configurations with particles placed on a simple cubic lattice with random dipole moment orientations.

4.2 Model Validation

Prior to investigating the magnetization and microstructures of ferrofluid systems under shear flow, for validation purpose, MD simulations are first performed for several test cases and the numerical results are compared to those available in the literature.

4.2.1 Equilibrium magnetization of a monodisperse system

The first test case calculates the equilibrium magnetization of a monodisperse system and follows the configuration of Ref. [99]. The simulated system has 1000 particles in a periodic cubic simulation box. Simulations are performed at $T^* = 1$ with $\lambda = 3$. The values of dimensionless friction coefficients do not affect the equilibrium magnetizations and are taken as $\Gamma_T^* = 10$ and $\Gamma_R^* = \Gamma_T^*/3$. The time step is set as $\Delta t^* = 0.002$. The system is equilibrated for 100 dimensionless time period at first and then sampled for another 400 dimensionless time period. The equilibrium magnetizations are estimated from the means of the samples and standard deviations of the means are also calculated and shown as error bars. The computed magnetizations of this work match well with Ref. [99] as shown in Fig. 4.2.

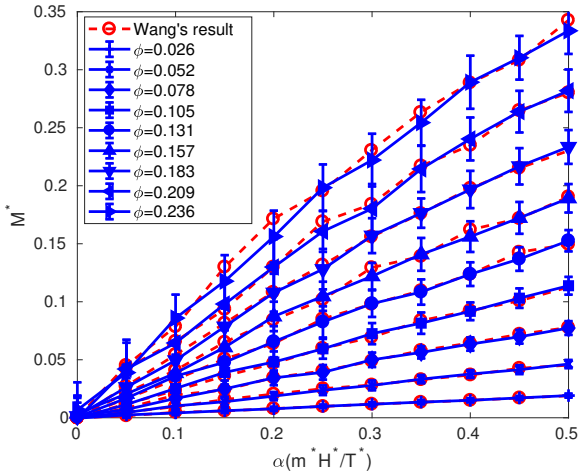

Figure 4.2: Dimensionless magnetization M^* of a monodisperse ferrofluid system as a function of the Langevin parameter α and the volume fraction ϕ with the dipolar coupling parameter $\lambda = 3$.

4.2.2 Equilibrium magnetization of a bidisperse system

The second test case is on the equilibrium magnetization of a bidisperse system [100]. The diameters of the two types of particles are chosen to be 10 nm and 16 nm,

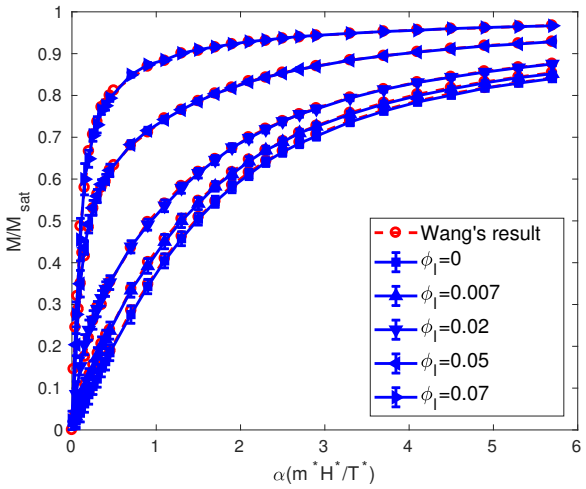

Figure 4.3: Magnetization curves of a bidisperse ferrofluid system as a function of the Langevin parameter α and the volume fraction of large particles ϕ_l with dipolar coupling parameters $\lambda_s = 1.32$ and $\lambda_l = 5.39$. The total volume fraction is fixed as $\phi = 0.07$. M_{sat} is the saturation magnetization.

respectively, which make the dipolar coupling parameters $\lambda_s = 1.32$ for the small particles at room temperature 300 K, and $\lambda_l = 5.39$ for the large ones. The total volume fraction of all particles is fixed at $\phi = 0.07$ and the volume fraction of large particles is varied from 0 to 0.07. Other parameters include: total number of particles set at 1000, temperature $T^* = 1$, and $\Delta t^* = 2 \times 10^{-3}$. Friction coefficients can be chosen arbitrarily and are taken as $\Gamma^*_{Ts} = 10$, $\Gamma^*_{Rs} = 10/3$, $\Gamma^*_{Tl} = 41$ and $\Gamma^*_{Rl} = 35$. The equilibration time is set at $t^* = 600$, and the equilibrium values of the magnetization are calculated for another period of $t^* = 2400$ after equilibration. Comparison of results in this work and Ref. [100] are shown in Fig. 4.3. The numerical results agree well with Ref. [100].

4.2.3 Non-equilibrium magnetization of a monodisperse system in shear flow

In this section, a monodisperse system is subjected to a shear flow $\mathbf{V}(\mathbf{r}) = (\gamma y, 0, 0)$. The dimensionless shear rate is set as $\gamma^* = 0.1$. The magnetic field $\mathbf{H} = (0, H, 0)$

is oriented in the flow gradient direction. For an NEMD simulation, the values of friction coefficients are important, therefore they should be calculated as described in Sec. 4.1. Here for the test case, they are set as the same values as in Ref. [118], i.e. $\Gamma_T^* = 10$ and $\Gamma_R^* = \Gamma_T^*/3$. Simulations are run with 15625 particles at $T^* = 1$. The time step is set as $\Delta t^* = 0.001$. The system is integrated for $t^* = 100$ to reach the stationary state. Steady state magnetizations are then calculated for another $t^* = 500$. The calculated results in this work generally agree with Ref. [118] in Fig. 4.4. The discrepancy is likely due to the difference in simulation methods. Ref. [118] used the reaction field method for long-range interactions, whereas the Ewald summation is used in this work.

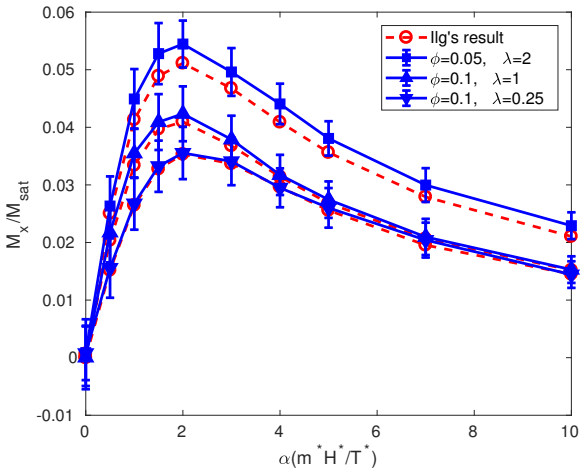

Figure 4.4: Non-equilibrium magnetization of a monodisperse ferrofluid system in shear flow as a function of the Langevin parameter α. The shear rate is set as $\gamma^* = 0.1$.

4.3 Results and Discussion

The test cases demonstrate the feasibility of investigating properties and microscopic behavior of ferrofluid using MD simulations. However, these MD simulations are based on either equilibrium situations or weak dipolar interactions, which are not sufficient for systematically understanding the dynamic properties and behavior of ferrofluid

particles. In this section, non-equilibrium molecular dynamics (NEMD) simulations involving shear flow in both monodisperse and bidisperse ferrofluid systems are performed to investigate these characteristics.

4.3.1 Effects of shear rate and magnetic field strength

The ferrofluid system to be investigated here also consists of two types of magnetite particles with diameters of 10 nm and 16 nm, which give dipolar coupling parameters $\lambda_s = 1.32$ and $\lambda_l = 5.39$ at room temperature 300 K, respectively. The total volume fraction ϕ is set as 0.1. The value of volume fraction ϕ is within the range of common commercial ferrofluids. For investigation purpose, the volume fraction of large particles is chosen to be 0, 0.05 and 0.1.

For equilibrium cases, the values of friction coefficients Γ_T^* and Γ_R^* do not affect the final magnetizations and can be chosen arbitrarily. Under non-equilibrium conditions, however, Γ_T^* and Γ_R^* should be calculated carefully. According to Eqs. (4.6, 4.9)

$$\Gamma_{Ts}^* = 3\pi\eta\sigma_s\sqrt{\frac{\sigma_s^2}{M_s\epsilon}}, \quad \Gamma_{Rs}^* = \pi\eta\sigma_s^3\sqrt{\frac{1}{M_s\sigma_s^2\epsilon}} = \frac{1}{3}\Gamma_{Ts}^*, \quad \Gamma_{Tl}^* = \sigma_l^*\Gamma_{Ts}^*, \quad \Gamma_{Rl}^* = \sigma_l^{*3}\Gamma_{Rs}^*, \tag{4.16}$$

At 300 K, the viscosity of water is around 8.56×10^{-4} Pa·s, which makes Γ_{Ts}^* around 241. The other three coefficients can also be calculated accordingly as $\Gamma_{Rs}^* = 80$, $\Gamma_{Tl}^* = 385$ and $\Gamma_{Rl}^* = 329$. Note that solvents of ferrofluids have a wide range of viscosity. To demonstrate the effect of friction coefficients, simulations are performed first on a monodisperse system of only small particles with $\eta = 8.56 \times 10^{-4}$ Pa·s and $\eta = 8.56 \times 10^{-5}$ Pa·s as shown in Fig. 4.5. The system is in a shear flow $\mathbf{V}(\mathbf{r}) = (\gamma y, 0, 0)$ with a magnetic field $\mathbf{H} = (0, H, 0)$ (see Fig. 4.1). The total number of particles is fixed at 2197 and the temperature

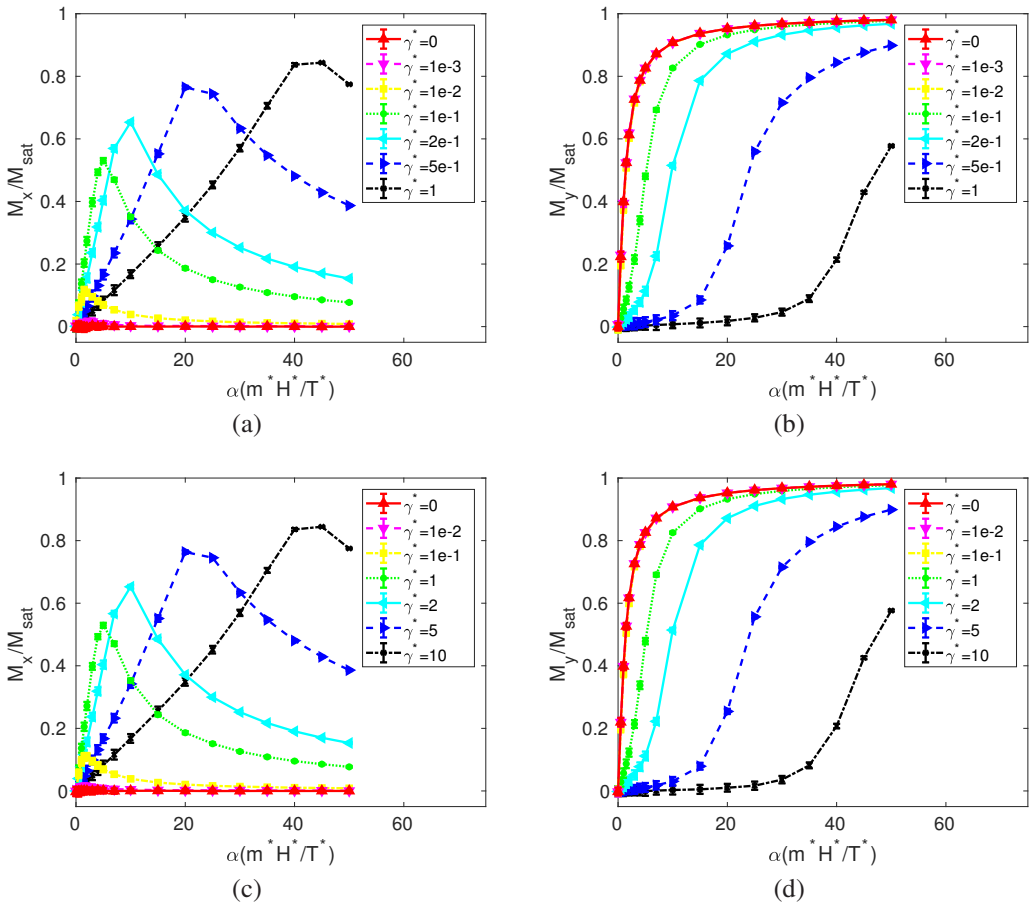

Figure 4.5: Non-equilibrium magnetization curves of a monodisperse ferrofluid system of small particles as a function of the Langevin parameter α and the shear rate γ^* with the volume fraction $\phi_s = 0.1$, the dipolar coupling parameter $\lambda_s = 1.32$, and the solvent viscosity (a-b) $\eta = 8.56 \times 10^{-4}$ Pa·s and (c-d) $\eta = 8.56 \times 10^{-5}$ Pa·s.

set at $T^* = 1$. The dimensionless time step is set as $\Delta t^* = 0.001$ except for the case of $\eta = 8.56 \times 10^{-5}$ Pa·s and $\gamma^* = 10$, where $\Delta t^* = 0.0005$ is used. The system is first integrated for $t^* = 1000$ to reach steady state and the subsequent data are output every 5 dimensionless time period for another $t^* = 1000$ afterwards. The steady state magnetizations are estimated from the means of the samples and the standard deviations of the means are also calculated and shown as error bars.

Figures 4.5a and 4.5b show that when the dimensionless shear rate $\gamma^* = 0$, x directional magnetization M_x is always around zero and y directional magnetization M_y

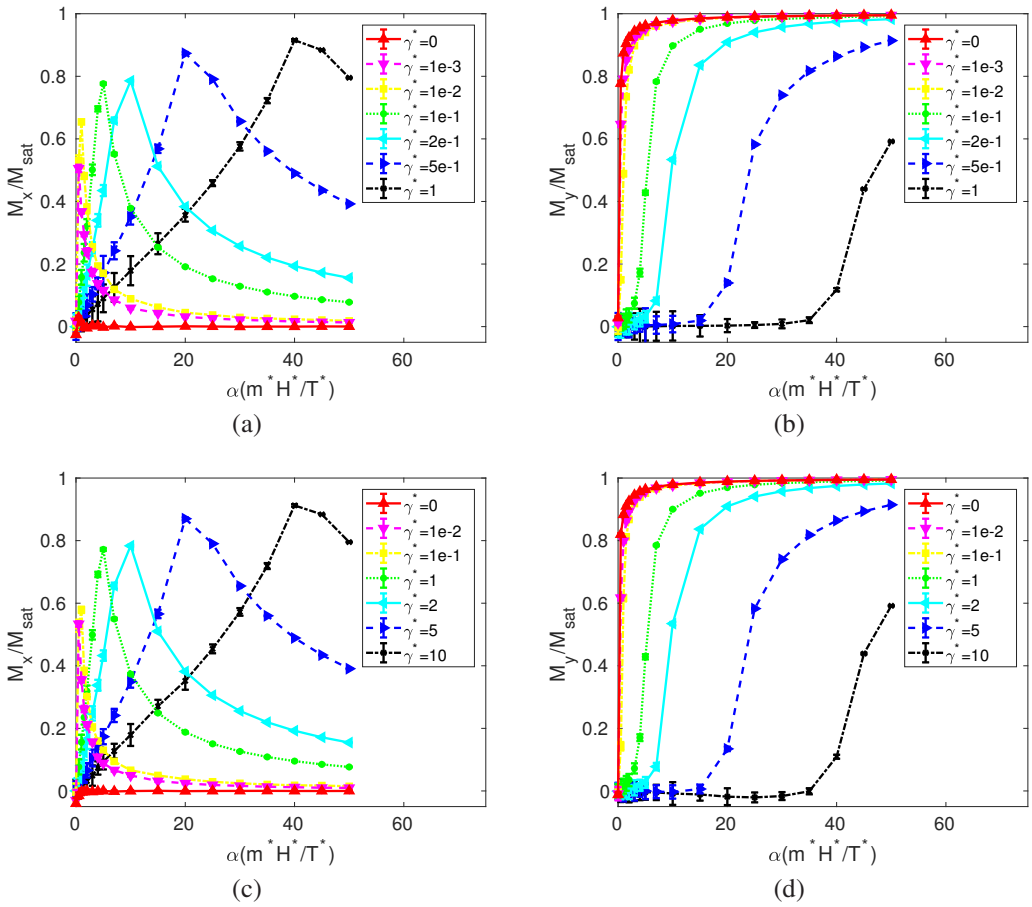

Figure 4.6: Non-equilibrium magnetization curves of a monodisperse ferrofluid system of large particles as a function of the Langevin parameter α and the shear rate γ^* with the volume fraction $\phi_l = 0.1$, the dipolar coupling parameter $\lambda_l = 5.39$, and the solvent viscosity (a-b) $\eta = 8.56 \times 10^{-4}$ Pa·s and (c-d) $\eta = 8.56 \times 10^{-5}$ Pa·s.

increases with α and eventually saturates as shown in the Langevin relation [58]. In the presence of the linear shear flow, M_x rises up first and then reduces with α. With larger γ^*, M_x increases slower but reaches a higher value. At the same γ^*, M_y rises slower than M_x and eventually saturates. Numerical results indicate that this is due to the competition between magnetic field and shear flow. Shear flow makes particles rotate clockwise whereas magnetic field makes them align in the direction of the field (y direction in this case). For a given γ^*, at small α, the dipoles start to align toward $\mathbf{H}$ but with an angle deviation, which means both the x- and y-components of the magnetization, M_x and M_y, are finite. When α

increases, both M_x and M_y increase due to higher magnetization. When α becomes larger, dipoles align more and more in the direction of $\mathbf{H}$, making M_x decrease and M_y increase further until saturation. At a higher shear rate γ^*, dipoles are rotated by the shear flow more and a higher $\mathbf{H}$ is needed to compete with the shear flow, resulting in the M_x-decreasing and M_y-saturating trend beginning later, and the M_x peak going higher. Comparison of Figs. 4.5a-4.5b and 4.5c-4.5d reveals that magnetization curves with $\eta = 8.56 \times 10^{-5}$ Pa·s show identical trends as those with $\eta = 8.56 \times 10^{-4}$ Pa·s at one tenth of γ^*. More simulations also show that $\eta = 8.56 \times 10^{-3}$ Pa·s results in same trends as $\eta = 8.56 \times 10^{-4}$ Pa·s at 10 times of γ^*. These results imply that, for the smaller particles, the product of η and γ is a determining factor of the magnetization curve as a function of α. Since high friction coefficients and high shear rate both limit the time step, simulations can be performed with a properly chosen set of Γ_T^*, Γ_R^* and γ^* which give identical results with a larger time step.

To test if the same phenomenon occurs for large particles, simulations are also performed on a large-particle system with $\eta = 8.56 \times 10^{-4}$ Pa·s and $\eta = 8.56 \times 10^{-5}$ Pa·s. At $\eta = 8.56 \times 10^{-5}$ Pa·s and $\gamma^* = 10$, $\Delta t^* = 0.00025$ is used, whereas $\Delta t^* = 0.001$ is used for all other cases. The system is integrated for $t^* = 2000$ and then sampled for $t^* = 1000$. Figure 4.6 shows that M_x and M_y for a large-particle system have similar trends as those for a small-particle system. However, one difference is M_x starts to respond to $\mathbf{H}$ at a smaller shear rate. Comparison of Figs. 4.6a-4.6b and 4.6c-4.6d also reveals that magnetization curves with $\eta = 8.56 \times 10^{-5}$ Pa·s have similar trends as those with $\eta = 8.56 \times 10^{-4}$ Pa·s at one tenth of γ^*. However, with $\eta = 8.56 \times 10^{-5}$ Pa·s, M_x values at γ^*=1e-2 and γ^*=1e-1, M_y values at $\gamma^* = 10$ are different from those with $\eta = 8.56 \times 10^{-4}$ Pa·s at one tenth of these shear rates. Therefore, for large particles, the physical values of friction coefficients need to calculated according to Eq. (4.16) to obtain the correct magnetization curves. The following simulations will all be conducted with $\eta = 8.56 \times 10^{-4}$ Pa·s.

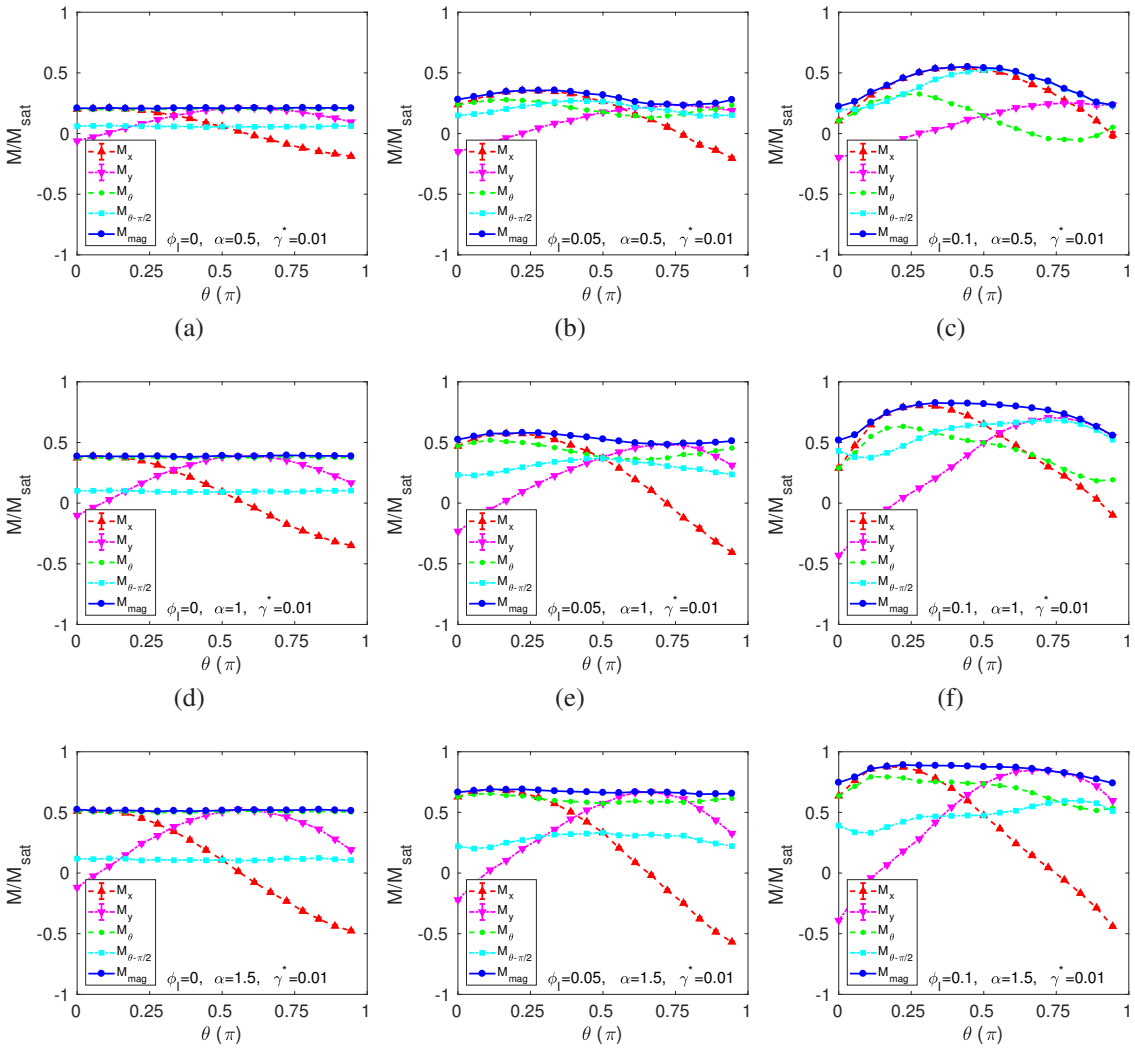

Figure 4.7: Magnetization curves of monodisperse and bidisperse ferrofluid systems as a function of the magnetic field direction θ with total volume fraction $\phi = 0.1$, dipolar coupling parameters $\lambda_s = 1.32$ and $\lambda_l = 5.39$, shear rate $\gamma^* = 0.01$, and solvent viscosity $\eta = 8.56 \times 10^{-4}$ Pa·s. The large particle volume fraction ϕ_l varies from 0 to 0.1 from left to right in each row and the Langevin parameter α increases from 0.5 to 1.5 from top to bottom in each column.

4.3.2 Effect of magnetic field direction

To further study how magnetic field and shear flow influence ferrofluid magnetization, the external magnetic field is applied in different directions. For a magnetic field **H**

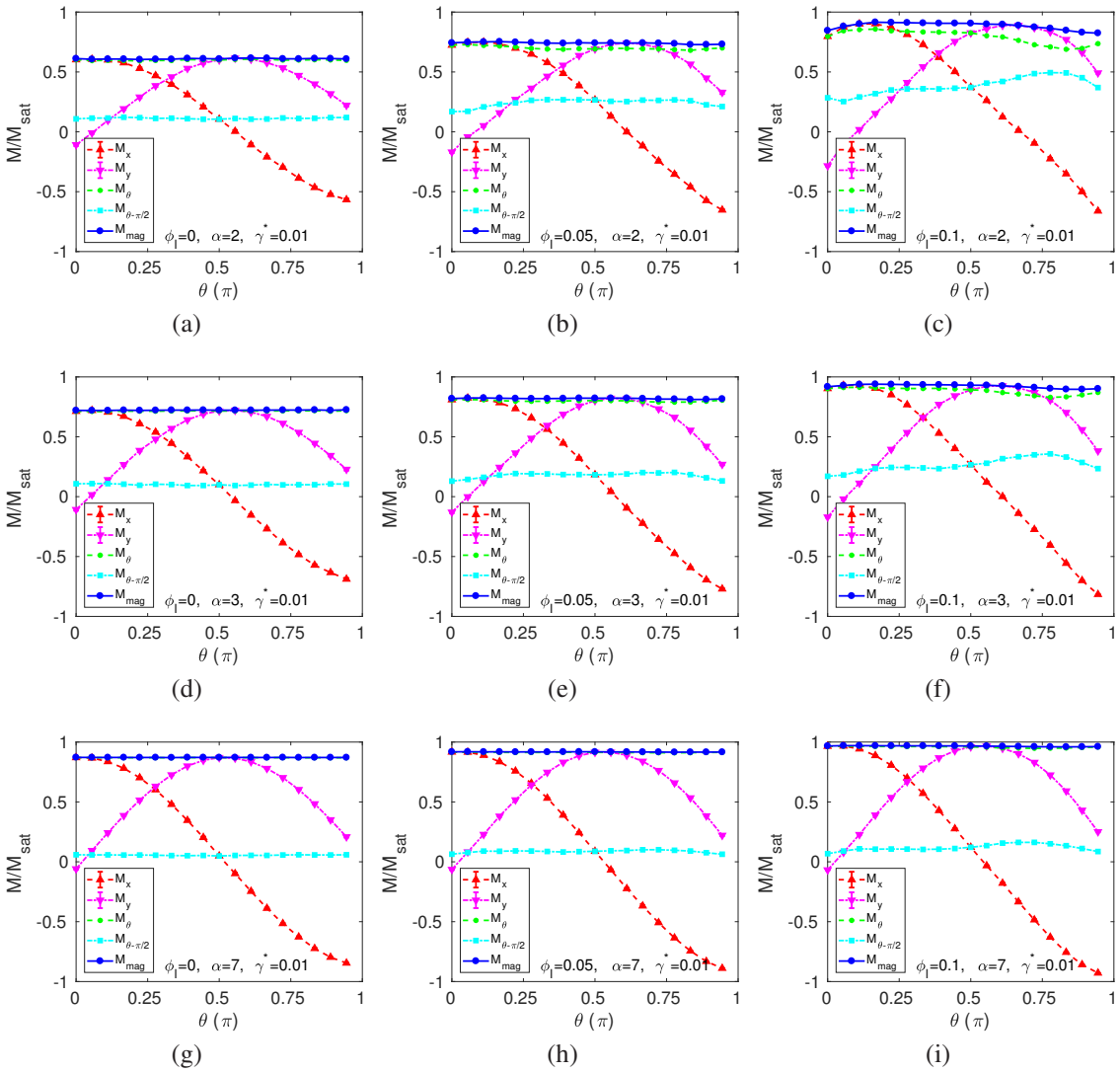

Figure 4.8: Same as Fig. 4.7 except that the Langevin parameter α varies from 2 to 7.

with direction θ as shown in Fig. 4.1, M_θ denotes the component of $\mathbf{M}$ in the θ direction, $M_{\theta-\pi/2}$ the component in the direction perpendicular to θ, and M_{mag} the magnitude of $\mathbf{M}$. θ is taken within the range [0, π) due to the symmetry or antisymmetry of the results in [π, 2π). Based on the convergence study, for $\gamma^* = 0.001$ and $\gamma^* = 0.01$, 5832 particles are used at $\alpha = 0.5$ and $\alpha = 1$ and 2197 particles for higher α. For $\gamma^* = 0.1$ and $\gamma^* = 1$, 1000 particles are considered for all α values. Dimensionless time step, integration period

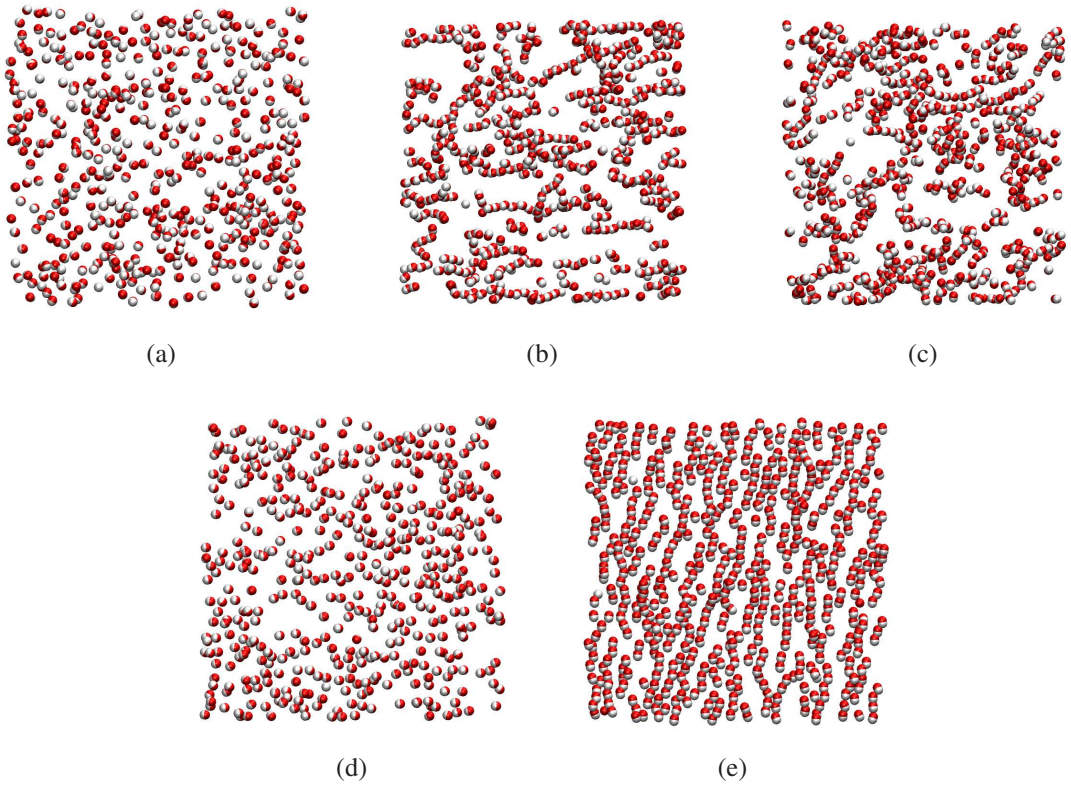

(a) (b) (c)

(d) (e)

Figure 4.9: Snapshots of system slabs with (a) $\phi_l = 0$, $\alpha = 0.5$, $\theta = 20°$, $C_{avg} = 1.010$, (b) $\phi_l = 0.1$, $\alpha = 0.5$, $\theta = 70°$, $C_{avg} = 1.631$, (c) $\phi_l = 0.1$, $\alpha = 0.5$, $\theta = 150°$, $C_{avg} = 1.492$, (d) $\phi_l = 0$, $\alpha = 7$, $\theta = 0°$, $C_{avg} = 1.023$, (e) $\phi_l = 0.1$, $\alpha = 7$, $\theta = 100°$, $C_{avg} = 1.511$. Both systems have 5832 particles. Other parameters are $\lambda_s = 1.32$, $\lambda_l = 5.39$, $\gamma^* = 0.01$, and $\eta = 8.56 \times 10^{-4}$ Pa·s.

before sampling, and sampling period are set at 0.001, 2000 and 1000, respectively. Error bars for M_x and M_y are also estimated based on the data from the sampling period.

The results for $\gamma^* = 0.01$ are given in Figs. 4.7 and 4.8. The first columns in these two figures show that, when the system only consists of small particles ($\phi_l = 0$), M_{mag} maintains a steady value with respect to θ and increases with α. M_θ and $M_{\theta-\pi/2}$ also bear steady values with respect to θ and M_θ is always higher than $M_{\theta-\pi/2}$. These trends demonstrate that magnetization of small particles has no preference in direction under shear flow. M_x and M_y increase and decrease alternatively as dipoles try to align to the direction

of $\mathbf{H}$. Visualization of the ferrofluid system is performed by VMD [123] as shown in Figs. 4.9a and 4.9d. All visualizations are performed for systems of 5832 particles for clear comparison. Each dipole is represented by two spherical particles slightly shifted away from the center of the particle mass in opposite directions along the dipole moment line. Note that only a slab of the simulation box in the z direction is shown in each snapshot for clear demonstration. Due to the lower dipolar interaction, small particles are not able to form chains as shown in both Figs. 4.9a and 4.9d, and the average cluster sizes are only slightly above 1, being 1.010 and 1.023, respectively.

As shown in the third columns, when $\phi_l = 0.1$, i.e., the system only consists of large particles, the magnetization components show clear trends as θ varies, especially when subjected to weak fields. M_{mag}, M_θ and $M_{\theta-\pi/2}$ are no longer near-constant. M_{mag} shows a peak at the maximum M_x value, $(M_x)_{max}$, and a trough at the maximum M_y value, $(M_y)_{max}$. $(M_x)_{max}$ is much larger than $(M_y)_{max}$ when the magnetic field is weak. θ corresponding to $(M_x)_{max}$ for large particles is much larger (nearly $\pi/2$ at $\alpha = 0.5$) than that for small particles, and decreases as α increases. Snapshots of the large-particle system corresponding to the cases of $(M_x)_{max}$ and $(M_y)_{max}$ at $\alpha = 0.5$ are shown in Figs. 4.9b and 4.9c to illustrate the chain structures. At $\theta = 70°$, many chains are formed along the x direction (C_{avg}=1.631), leading to a higher $(M_x)_{max}$. At $\theta = 150°$, chains are not able to form and align in the y direction due to the shear flow which constantly rotates and breaks the chains ($C_{avg} = 1.492$), leading to a lower $(M_y)_{max}$. On the other hand, at higher α, since the magnetic interaction is much stronger than the shear flow effect, dipoles again align in the $\mathbf{H}$ direction with larger magnetization magnitudes. Figure 4.9e reveals that longer chains are formed in the y direction ($C_{avg} = 1.511$). When $\phi_l = 0.05$, the magnetization behavior falls between those of $\phi_l = 0$ and $\phi_l = 0.1$. The transitions can be clearly seen in Figs. 4.7 and 4.8.

Since the magnetization of large particles shows a stronger dependence on θ than

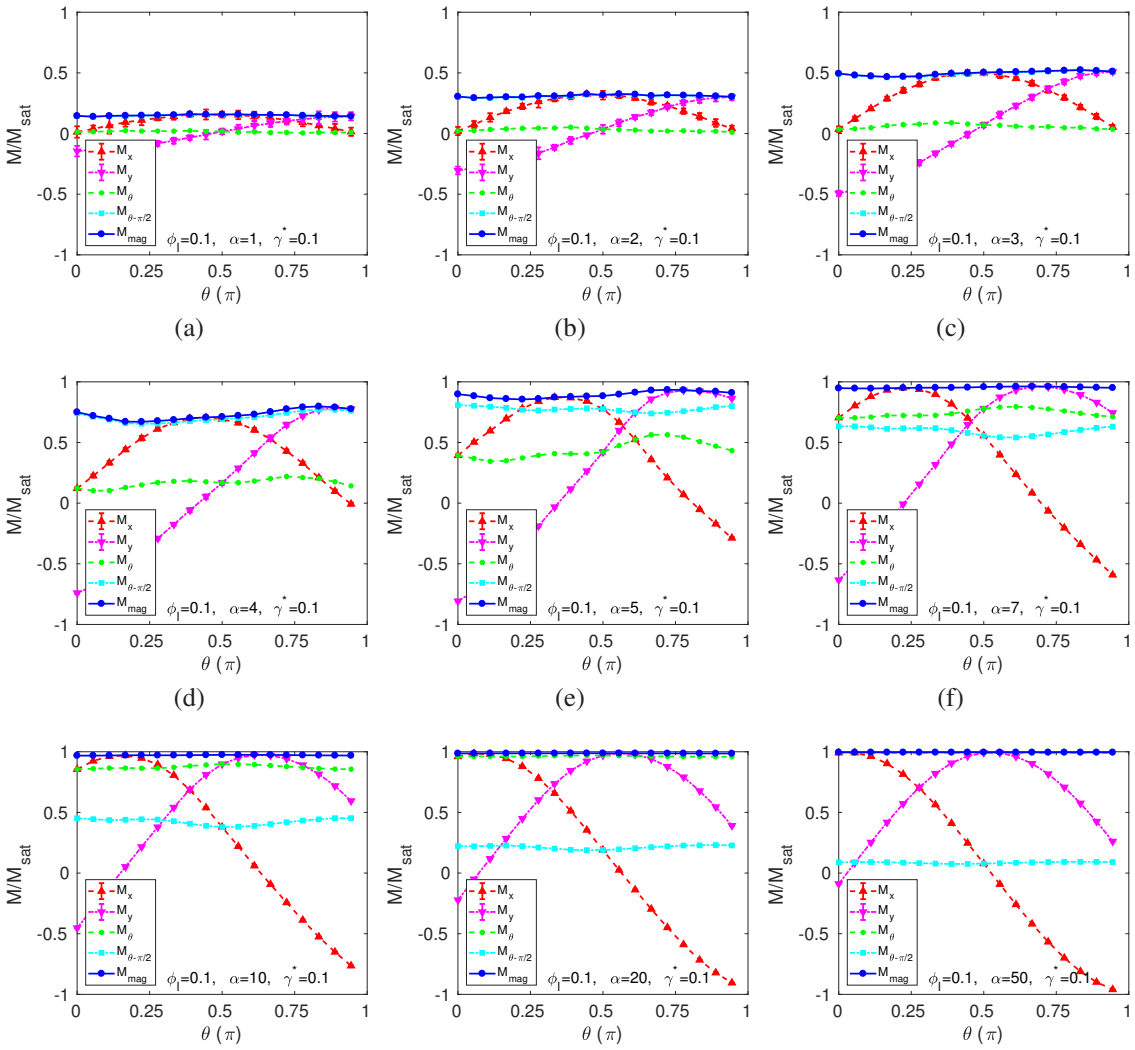

Figure 4.10: Magnetization curves of a monodisperse ferrofluid system as a function of the magnetic field direction θ with large particle volume fraction $\phi_l = 0.1$, dipolar coupling parameter $\lambda_l = 5.39$, shear rate $\gamma^* = 0.1$, and solvent viscosity $\eta = 8.56 \times 10^{-4}$ Pa·s. The Langevin parameter α increases from 1 to 50.

that of small ones, we focus on the results for the large-particle system in this section. Figure 4.10 shows the magnetization curves as functions of the magnetic field direction θ for the large-particle system subjected to a larger shear rate $\gamma^* = 0.1$. The sub-plots show variation of these magnetization curves when α is changed from 1 to 50. In weak fields,

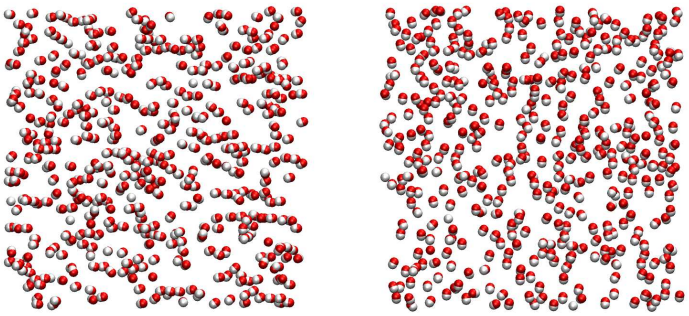

(a) (b)

Figure 4.11: Snapshots of system slabs with (a) $\phi_l = 0.1$, $\alpha = 4$, $\theta = 80°$, $C_{avg} = 1.193$, (b) $\phi_l = 0.1$, $\alpha = 4$, $\theta = 160°$, $C_{avg} = 1.074$. The system has 5832 particles. Other parameters are $\lambda_l = 5.39$, $\gamma^* = 0.1$, and $\eta = 8.56 \times 10^{-4}$ Pa·s.

M_θ is smaller than $M_{\theta-\pi/2}$, as the shear flow exerts a stronger influence than the weak magnetic field. When the magnetic field becomes strong, M_θ is larger than $M_{\theta-\pi/2}$ similar to the results in Fig. 4.8i. Note that with larger γ^*, θ for $(M_x)_{max}$ is larger compared to that in Figs. 4.7 and 4.8 at the same α.. An interesting observation is that in the transition range of $\alpha \in [3, 5]$, $(M_y)_{max}$ is larger than $(M_x)_{max}$, which is contradictory to what is shown in Fig. 4.7c. Snapshots of the nanoparticles for instances of $(M_x)_{max}$ and $(M_y)_{max}$ at $\alpha = 4$ are shown in Fig. 4.11. As the shear flow gradient is larger here, for both cases, the average cluster sizes (1.193 and 1.074) at $\alpha = 4$ are smaller than those (1.631 and 1.492) in Figs. 4.9b and 4.9c at $\alpha = 0.5$. At $\theta = 80°$, due to the effects of both higher shear flow gradient and higher magnetic field compared to those in Fig. 4.9b, chains and dipoles in the chains deviate from the x direction. On the other hand, at $\theta = 160°$, almost all the chains are broken into pieces. In this case, it is observed that dipoles individually all tend to align in the y direction, which makes $(M_y)_{max}$ larger than $(M_x)_{max}$.

Figure 4.12 compares the magnetization curves calculated for different shear rates. The four sub-plots are corresponding to shear rates of four different orders of magnitude: γ^*=0.001, 0.01, 0.1 and 1, respectively. The results again show that θ for $(M_x)_{max}$ is

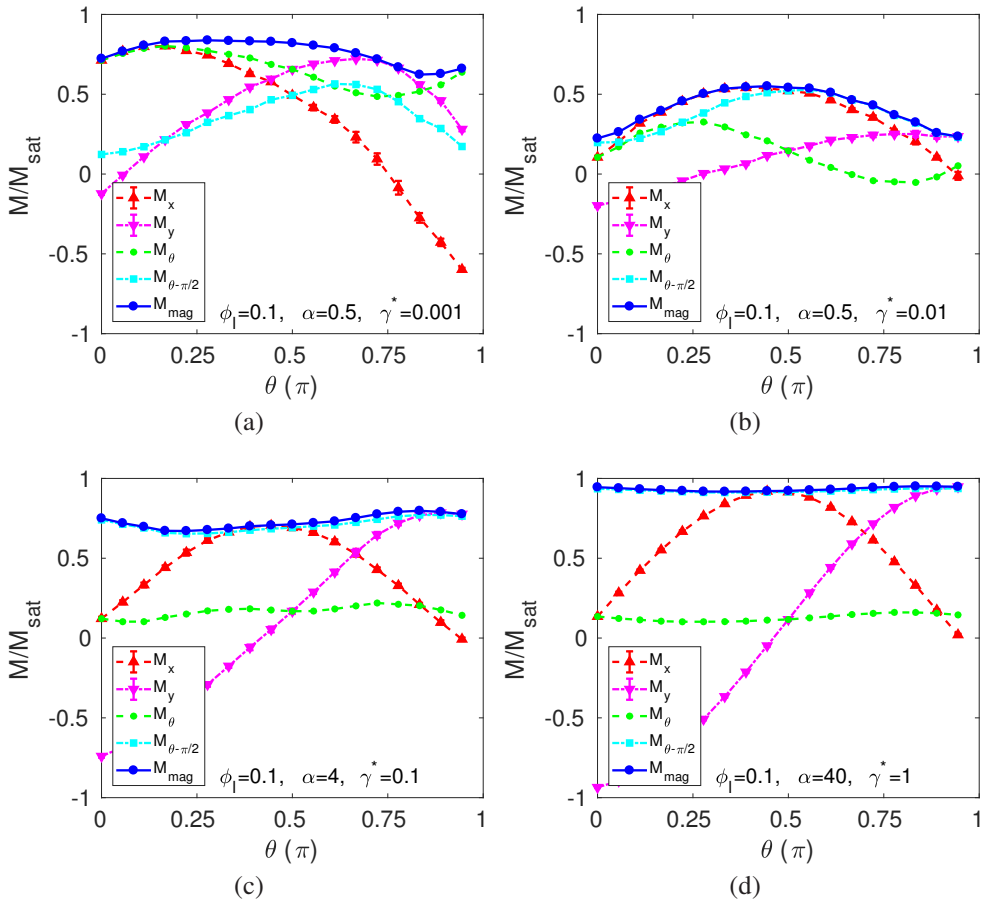

Figure 4.12: Magnetization curves of a monodisperse ferrofluid system as a function of the magnetic field direction θ with large particle volume fraction $\phi_l = 0.1$, dipolar coupling parameter $\lambda_l = 5.39$, and solvent viscosity $\eta = 8.56 \times 10^{-4}$ Pa·s.

positively related to the ratio of shear rate to magnetic field strength, γ^*/α. In addition, at small γ^*, $(M_x)_{max} > (M_y)_{max}$, whereas at large γ^*, $(M_x)_{max} < (M_y)_{max}$. When γ^* is very large, M_θ, $M_{\theta-\pi/2}$ and M_{mag} are almost independent of θ.

Chapter 5

Conclusions

This chapter presents the conclusions of this dissertation. The research presented is focused on computational modeling and performance Analysis of a sloshing ferrofluid based electromagnetic energy harvester. The following sections summarize the findings.

5.1 Continuum Level Modeling and Implementation

A FE model is described and implemented in Chapter 2 for computational analysis of a ferrofluid based electromagnetic energy harvester. The energy harvester consists of a tank partially filled with ferrofluid, a copper coil wound around the tank, and two magnets placed by the tank. The ferrofluid undergoes a sloshing motion due to an external excitation applied at the base of the tank. In the FE model, the magnetic field distribution is obtained by solving the magnetic scalar potential equation using the Galerkin method. The velocity field of the fluid is obtained by solving the Navier-Stokes and continuity equations using the streamline-upwind/Petrov-Galerkin (SUPG) and pressure-stabilizing/Petrov-Galerkin (PSPG) methods. The Volume of Fluid (VOF) method is employed to keep track of the liquid-gas interface. The sharp surface tension force model (SSF) is employed to capture

the influence of surface tension, along with the height function method for interface curvature estimation. The computational model is validated against experimental results for eight different configurations of the energy harvester. The results show that the electromotive force-excitation frequency characteristics of the energy harvester are captured by the model. Numerical and experimental results are in a reasonably good agreement where it is shown that the maximum error in peak frequency and electromotive force is less than 0.1 Hz and 5 mV, respectively.

By using the validated model and numerical results, it is shown that the basic mechanism responsible for the change in magnetic flux in the coils during each sloshing cycle is the magnetization carried by the sloshing ferrofluid. Variation of the magnetization magnitude and its direction depends on the location of the ferrofluid bulk in the external magnetic field. Furthermore, the effects of several modeling aspects on the accuracy of the numerical model are studied. Results show that (i) the 2-D model is a reasonable approximation of the 3-D energy harvester as long as the tank is sufficiently long in the z direction; and (ii) surface tension and the two-way coupling between the magnetic field and fluid flow are important to capture the actual dynamics of the results.

5.2 Performance Analysis of the Energy Harvester

A parametric study and performance analysis of the ferrofluid based electromagnetic energy harvester are performed in Chapter 3. Two magnet configurations with their respective coil windings are investigated. The first configuration (Config. (1)) has magnets on the sides of the tank with same pole alignment and a horizontal coil, whereas the second configuration (Config. (2)) has magnets above and underneath the tank with opposite pole alignment and a vertical coil.

The parametric study and performance analysis reveal that a set of parameters af-

fecting the magnetic flux have a substantial influence on the electromotive force, ε. The influence of these parameters is summarized as follows:

- In most cases, attaining a higher magnetic field by bringing the magnets closer to the tank leads to a larger magnetic flux, and hence, larger ε. However, extremely high magnetic fields force the ferrofluid to cling onto the tank wall, thereby diminishing the amplitude of the sloshing motion, and eventually leading to lower values of ε. In the current study, the optimal distance between the magnets and the ferrofluid sloshing surface is 1.65 cm. In Config. (1), when the magnets are placed higher than the ferrofluid surface, the resonant frequency can also be reduced by moving the magnets closer to the tank.

- The electromotive force, ε, changes significantly when the magnetic field distribution is altered by changing the location of the magnets with respect to the ferrofluid surface. In specific, it is shown that there is an optimal magnet placement which results in maximum ε. For Config. (1), magnets should always be placed in such a way that the magnetic field in the vertical direction H_y stays unidirectional on either side of the tank but has opposite directions on each side. This implies the magnets should be placed above the ferrofluid surface at an optimal height determined by the sloshing amplitude. For Config. (2), H_x should stay unidirectional on either side of the tank but has opposite directions on each side.

- Generally, increasing ferrofluid susceptibility leads to an increase in ε until saturation value is reached. The saturation value is much smaller for Config. (2).

Numerical simulations also demonstrate that the tank length, ferrofluid level, and the amplitude of the base acceleration play important roles in determining ε and resonant frequency. Our specific case shows:

- When the ferrofluid level is 2.5 cm, the optimal tank length is around 10 cm, which keeps a good balance between ε and tank size. Increasing the tank length reduces the resonant frequency.

- When the tank has both the length and height set as 12.7 cm, for Config. (1) the ferrofluid level around 9 cm gives the maximum ε. Config. (2) always gives low ε regardless of the ferrofluid level. For both configurations, the highest resonant frequency also occurs at the ferrofluid level range between 9 and 10cm.

- Increasing base acceleration amplitude also leads to a higher ε. However, the resonant frequency increases initially and decreases in the end.

When varying within their realistic ranges, ferrofluid material properties such as its viscosity, surface tension coefficient, and density have very little effect on ε and resonant frequency. Low viscosity and high density can lead to a slightly higher ε.

5.3 Molecular Dynamics Analysis of Magnetization and Microscopic Behavior of Ferrofluid

The magnetization and microstructures of ferrofluid systems subjected to magnetic field and shear flow are investigated using non-equilibrium molecular dynamics simulations in Chapter 4. Monodisperse and bidisperse ferrofluid systems are considered. The shear flow is in the x-direction and the velocity gradient is along the y-direction. The physical behavior of the ferrofluid systems revealed by the simulation results includes (1) for smaller particles, the product of the solvent viscosity η and shear rate γ is a determining factor of the ferrofluid magnetization curve as a function of magnetic field strength; This rule, however, does not apply to large particles; (2) when subjected to a magnetic field (strong or weak) in

various directions, small particles tend to stay separate from each other and the magnitude of magnetization is almost identical regardless of the direction of magnetic field; (3) when subjected to a weak magnetic field, large particles form chains, and the characteristics of the chain orientation and magnetization depend on the shear rate; and (4) when the magnetic field is strong enough, as the influence of shear flow becomes less significant, large particles always form chains along the magnetic field direction, and magnetization magnitude maintains a steady value with respect to the magnetic field direction.

Appendices

Appendix A Governing Equations for Ferrofluid with Spinning Particles

For continuum level modeling of the ferrofluid based energy harvester in Chapter. 2, governing equations are given assuming magnetic particles in ferrofluid always align in the direction of the external magnetic field. However in reality, with an applied $\mathbf{H}$, a ferrofluid particle can either align its magnetic moment with the field by a rotation of the whole particle, a process called Brownian relaxation, or by a change of the direction of the magnetic moment inside the particle, the so-called Néel relaxation [58]. Both relaxation processes are characterized by respective relaxation times τ_B and τ_N. Either way produces a lag between $\mathbf{H}$ and $\mathbf{M}$. This appendix contains the governing equations for the ferrofluid based energy harvester taking into consideration the spinning ferrofluid particles.

Two assumptions as in Sec. 2.2.1 are adopted in modeling the coupled magneto-ferro-hydrodynamic system in this section: (1) the energy harvester is represented by a 2-D system as in Fig. 2.2; (2) ferrofluid is considered to be an incompressible viscous fluid with non-negligible surface tension. The assumption that ferrofluid is considered to be superparamagnetic in Sec. 2.2.1 is removed.

A.1 Magnetization relaxation equation for ferrofluid particles

The relation between $\mathbf{H}$ and $\mathbf{M}$ for ferrofluid with spinning particles follows the magnetization relaxation equation [58]

$$\frac{\partial \mathbf{M}}{\partial t} + \mathbf{V} \cdot \nabla \mathbf{M} = \boldsymbol{\omega} \times \mathbf{M} - \frac{1}{\tau_{eff}}(\mathbf{M} - \mathbf{M}_{eq}) \tag{1}$$

where $\boldsymbol{\omega}$-spin rate, τ_{eff}-relaxation time. $\mathbf{M}_{eq}$ is the equilibrium magnetization, which is obtained in motionless fluid in a steady magnetic field $\mathbf{H}$. The equilibrium magnetization-

magnetic field relation is the Langevin relation [58].

$$\frac{\mathbf{M}_{eq}}{M_{sat}} = L(\alpha)\frac{\mathbf{H}}{H} = \left[\coth\alpha - \frac{1}{\alpha}\right]\frac{\mathbf{H}}{H} \tag{2}$$

$$M_{sat} = \phi M_d, \qquad \alpha = \frac{\mu_0 M_d H V_c}{k_B T} \tag{3}$$

Let $\mathbf{M}_{eq} = \chi(H)\mathbf{H}$, then

$$\chi(H) = \frac{M_{sat}L(\alpha)}{H} \tag{4}$$

where $\mathbf{M}_d$-domain magnetization, V_c-volume of the magnetic core, α-Langevin parameter. The Brownian relaxation time τ_B scales linearly with the particle volume, while the Néel relation time τ_N grows exponentially with the particle size. Since the actual relaxation process takes place by the one with the shortest relaxation time, the small particles will follow the Néel process while the large ones behave in a Brownian manner. Here the effective relaxation time is given as [48]

$$\frac{1}{\tau_{eff}} = \frac{1}{\tau_B} + \frac{1}{\tau_N}, \quad \tau_B = \frac{3\eta V_h}{k_B T}, \quad \tau_N = \frac{1}{f_0} exp\left(\frac{K_a V_c}{k_B T}\right) \tag{5}$$

where V_h-hydrodynamic particle volume, f_0-characteristic frequency for Néel relaxation, K_a-magnetocrystalline anisotropy constant of magnetic domains. No boundary condition is needed for Magnetization Relaxation Equation.

A.2 Spin equation for ferrofluid particles

The conservation of angular momentum gives the spin equation [58]

$$0 = \mu_0 \mathbf{M} \times \mathbf{H} + 2\zeta(\nabla \times \mathbf{V} - 2\boldsymbol{\omega}) + \eta' \nabla^2 \boldsymbol{\omega} \tag{6}$$

Where ζ-vortex viscosity, η'-shear coefficient of spin viscosity. There are two possibilities for the boundary condition. The "spin-no-slip" boundary condition assumes the particle-wall interaction is so strong that there is no spin on the boundary

$$\boldsymbol{\omega} = \mathbf{0} \tag{7}$$

The "spin-vorticity" boundary condition assumes that antisymmetric stresses vanish at the wall

$$\boldsymbol{\omega} - \frac{1}{2}\nabla \times \mathbf{V} = \mathbf{0} \tag{8}$$

Khushrushahi [48] proved that the "spin-vorticity" boundary condition is not valid. Thus the "spin-no-slip" boundary condition is used. In this work, spin is only in the z direction.

A.3 Navier-Stokes equations for fluid dynamics in the tank

Similar to Sec. 2.2.1.2, the Navier-Stokes equations and continuity equations for ferrofluid with spinning particles are given as [58, 59]

$$\rho\left[\frac{\partial \mathbf{V}}{\partial t} + \mathbf{V}\cdot\nabla\mathbf{V}\right] = -\nabla P + 2\zeta\nabla\times\boldsymbol{\omega} + (\eta+\zeta)\nabla^2\mathbf{V} + \mu_0\mathbf{M}\cdot\nabla\mathbf{H} - \rho\mathbf{g} \\ +\rho\mathbf{a_0}\cos(\omega t) - \sigma\kappa\nabla H(f) \tag{9}$$

$$\nabla\cdot\mathbf{V} = 0 \tag{10}$$

Appendix B Finite Element Formulation and Implementation for Ferrofluid with Spinning Particles

This appendix contains details of the FE formulation and implementation of the ferrofluid based energy harvester taking into consideration the spinning ferrofluid particles. In this FE formulation, the magnetization is obtained by solving the magnetization relaxation equation using the characteristic-Galerkin method. The spin of particles is obtained by solving the spin equation using the Galerkin method. The velocity field of the fluid is obtained by solving the Navier-Stokes and continuity equations using the streamline-upwind/Petrov-Galerkin (SUPG) and pressure-stabilizing/Petrov-Galerkin (PSPG) methods. The FE formulation and implementation of the magnetic scalar potential equation here is similar to those in Sec. 2.2.2.1, except that $\chi\nabla\psi$ in the second term in Eq. (2.26) should be replaced with $-\mathbf{M}$, which is evaluated separately as in Sec. A.1.

B.1 Magnetization relaxation equation

The magnetization relaxation equation Eq. (1) can be projected into the x and y directions as

$$\frac{\partial M_x}{\partial t} + V_x\frac{\partial M_x}{\partial x} + V_y\frac{\partial M_x}{\partial y} = -\omega_z M_y - \frac{1}{\tau_{eff}}(M_x - \chi H_x) \tag{11}$$

$$\frac{\partial M_y}{\partial t} + V_x\frac{\partial M_y}{\partial x} + V_y\frac{\partial M_y}{\partial y} = \omega_z M_x - \frac{1}{\tau_{eff}}(M_y - \chi H_y) \tag{12}$$

Since the magnetization relaxation equation has the form of a transport equation, in this work, the characteristic-Galerkin procedure [124] is applied to derive the weak form.

The equation in the x direction is used to illustrate the derivation of the weak form.

$$\frac{DM_x}{Dt} = -\omega_z M_y - \frac{1}{\tau_{eff}} M_x + \frac{\chi}{\tau_e ff} H_x \tag{13}$$

Let's start from the 1-D case. Assume a particle is at the location x at time t^{n+1}. Then it should be at $x - \delta$ at time t_n due to convection, where $\delta = \bar{u}\Delta t$.

$$\begin{aligned}\frac{1}{\Delta t}(M_x^{n+1} - M_x^n|_{(x-\delta)}) =& \frac{1}{2}\left(-\omega_z M_y - \frac{1}{\tau_{eff}} M_x + \frac{\chi}{\tau_{eff}} H_x\right)^{n+1} \\ &+ \frac{1}{2}\left(-\omega_z M_y - \frac{1}{\tau_{eff}} M_x + \frac{\chi}{\tau_{eff}} H_x\right)_{(x-\delta)}^{n}\end{aligned} \tag{14}$$

From the Taylor expansion we have

$$M_x^n|_{(x-\delta)} = M_x^n - \delta\frac{\partial M_x^n}{\partial x} + \frac{1}{2}\delta^2\frac{\partial^2 M_x^n}{\partial x^2} + O(\Delta t^3) \tag{15}$$

$$H_x^n|_{(x-\delta)} = H_x^n - \delta\frac{\partial H_x^n}{\partial x} + O(\Delta t^2) \tag{16}$$

$$(\omega_z M_y)^n|_{(x-\delta)} = (\omega_z M_y)^n - \delta\frac{\partial(\omega_z M_y)^n}{\partial x} + O(\Delta t^2) \tag{17}$$

One approximation of $\bar{u}$ is as follows

$$\bar{u} = \frac{1}{2}\left(u^{n+1} + u^n|_{(x-\delta)}\right) = u^{n+\frac{1}{2}} - \frac{1}{2}\Delta t u^n\frac{\partial u^n}{\partial x} + O(\Delta t^2) \tag{18}$$

so we get

$$\begin{aligned}\frac{1}{\Delta t}(M_x^{n+1} - M_x^n) =& -u^{n+\frac{1}{2}}\frac{\partial M_x^n}{\partial x} + \frac{1}{2}u^n\Delta t\frac{\partial u^n}{\partial x}\frac{\partial M_x^n}{\partial x} + \frac{1}{2}(u^{n+\frac{1}{2}})^2\Delta t\frac{\partial^2 M_x^n}{\partial x^2} \\ &+ \left(-\omega_z M_y - \frac{1}{\tau_{eff}} M_x + \frac{\chi}{\tau_{eff}} H_x\right)^{n+\frac{1}{2}} \\ &- \frac{1}{2}u^{n+\frac{1}{2}}\Delta t\left(-\frac{\partial(\omega_z M_y)}{\partial x} - \frac{1}{\tau_{eff}}\frac{\partial M_x}{\partial x} + \frac{\chi}{\tau_{eff}}\frac{\partial H_x}{\partial x}\right)^n\end{aligned} \tag{19}$$

If $n+1/2$ terms are replaced with n terms, we get

$$\begin{aligned} M_x^{n+1} - M_x^n = &- \Delta t \left[\frac{\partial (u M_x)}{\partial x} + \omega_z M_y + \frac{1}{\tau_{eff}} M_x - \frac{\chi}{\tau_{eff}} H_x \right]^n \\ &+ \frac{1}{2} \Delta t^2 u^n \frac{\partial}{\partial x} \left[\frac{\partial (u M_x)}{\partial x} + \omega_z M_y + \frac{1}{\tau_{eff}} M_x - \frac{\chi}{\tau_{eff}} H_x \right]^n \end{aligned} \tag{20}$$

For multidimensional problems

$$\begin{aligned} M_x^{n+1} - M_x^n = &- \Delta t \left[\frac{\partial (V_j M_x)}{\partial x_j} + \omega_z M_y + \frac{1}{\tau_{eff}} M_x - \frac{\chi}{\tau_{eff}} H_x \right]^n \\ &+ \frac{1}{2} \Delta t^2 V_i^n \frac{\partial}{\partial x_i} \left[\frac{\partial (V_j M_x)}{\partial x_j} + \omega_z M_y + \frac{1}{\tau_{eff}} M_x - \frac{\chi}{\tau_{eff}} H_x \right]^n \end{aligned} \tag{21}$$

Applying the Galerkin method and Green's formula, the week form can be obtained as

$$\begin{aligned} \int_\Omega \delta M_x \cdot \Delta M_x \cdot d\Omega = &- \Delta t \int_\Omega \delta M_x \left[\frac{\partial (V_j M_x)}{\partial x_j} + \omega_z M_y + \frac{1}{\tau_{eff}} M_x - \frac{\chi}{\tau_{eff}} H_x \right]^n d\Omega \\ &- \frac{1}{2} \Delta t^2 \int_\Omega \frac{\partial}{\partial x_i} (\delta M_x V_i^n) \left[\frac{\partial (V_j M_x)}{\partial x_j} + \omega_z M_y + \frac{1}{\tau_{eff}} M_x - \frac{\chi}{\tau_{eff}} H_x \right]^n d\Omega \end{aligned} \tag{22}$$

The weak form in the y direction is

$$\begin{aligned} \int_\Omega \delta M_y \cdot \Delta M_y \cdot d\Omega = &- \Delta t \int_\Omega \delta M_y \left[\frac{\partial (V_j M_y)}{\partial x_j} - \omega_z M_x + \frac{1}{\tau_{eff}} M_y - \frac{\chi}{\tau_{eff} H_y} \right]^n d\Omega \\ &- \frac{1}{2} \Delta t^2 \int_\Omega \frac{\partial}{\partial x_i} (\delta M_y V_i^n) \left[\frac{\partial (V_j M_y)}{\partial x_j} - \omega_z M_x + \frac{1}{\tau_{eff}} M_y - \frac{\chi}{\tau_{eff} H_y} \right]^n d\Omega \end{aligned} \tag{23}$$

B.2 Spin equation

Projecting Eq. (6) into the z direction leads to

$$-\eta' \nabla^2 \omega_z + 4\zeta \omega_z = \mu_0 (M_x H_y - M_y H_x) + 2\zeta \left(\frac{\partial V_y}{\partial x} - \frac{\partial V_x}{\partial y} \right) \tag{24}$$

Let's look at how the spin equation is derived [58]. From the internal angular momentum balance, we have

$$0 = \rho\mathbf{G} + \nabla \cdot \mathbf{C} + A \tag{25}$$

where G is the body couple exerted by a distant source and ρG is the torque. In this case, $\rho\mathbf{G} = \mu_0\mathbf{M} \times \mathbf{H}$. A is the rate of conversion of external angular momentum to internal angular momentum. Physically, this conversion arises when there is a lack of synchronization between the rate of rotation of a fluid element and the rate of internal spin. The effective rate of rotation of a fluid element is represented by half the vorticity.

$$\frac{1}{2}\boldsymbol{\Omega} = \frac{1}{2}\nabla \times \mathbf{V} \tag{26}$$

Thus, A is expressed as a function of the difference between the vorticity and the spin. Assuming a linear relation, we have

$$\mathbf{A} = 2\zeta(\nabla \times \mathbf{V} - 2\boldsymbol{\omega}) \tag{27}$$

C is the couple stress tensor. It is assumed to be symmetric and has the following expression

$$\mathbf{C} = \lambda'(\nabla \cdot \boldsymbol{\omega})\mathbf{I} + \eta'[\nabla\boldsymbol{\omega} + (\nabla\boldsymbol{\omega})^T] \tag{28}$$

Since $\boldsymbol{\omega}$ has only one component in the z direction, which is only a function of x and y, the first term in the expression of C vanishes.

$$[\mathbf{C}] = \eta' \begin{bmatrix} 0 & 0 & \frac{\partial \omega_z}{\partial x} \\ 0 & 0 & \frac{\partial \omega_z}{\partial y} \\ \frac{\partial \omega_z}{\partial x} & \frac{\partial \omega_z}{\partial y} & 0 \end{bmatrix} \tag{29}$$

$$\nabla \cdot \mathbf{C} = \frac{\partial^2 \omega_z}{\partial x^2} + \frac{\partial^2 \omega_z}{\partial y^2} = \nabla^2 \omega_z \tag{30}$$

Using the Galerkin method, the weak form for the spin equation can be obtained.

$$-\int_{\Omega^e} \delta\omega_z \left(\frac{\partial C_{13}}{\partial x} + \frac{\partial C_{23}}{\partial y} \right) d\Omega = \int_{\Omega^e} \delta\omega_z (\rho G + A) d\Omega \tag{31}$$

$$\int_{\Omega^e} \left(\frac{\partial \delta\omega_z}{\partial x} C_{13} + \frac{\partial \delta\omega_z}{\partial y} C_{23} \right) d\Omega = \int_{\Omega^e} \delta\omega_z (\rho G + A) d\Omega + \int_{\Gamma} \delta\omega_z (C_{13} n_x + C_{23} n_y) d\Gamma \tag{32}$$

Substituting the expressions of C_{13}, C_{23}, ρG and $\mathbf{A}$ into Eq. (32), we have

$$\begin{aligned} &\int_{\Omega^e} \nabla \delta\omega_z \cdot \eta' \cdot \nabla \omega_z \cdot d\Omega + \int_{\Omega^e} \delta\omega_z \cdot 4\zeta \cdot \omega_z \cdot d\Omega \\ &= \int_{\Omega^e} \delta\omega_z \cdot 2\zeta \left(\frac{\partial V_y}{\partial x} - \frac{\partial V_x}{\partial y} \right) d\Omega + \int_{\Omega^e} \mu_0 (M_x H_y - M_y H_x) d\Omega + \int_{\Gamma_e} \eta' \delta\omega_z \cdot \frac{\partial \omega_z}{\partial \mathbf{n}} d\Gamma \end{aligned} \tag{33}$$

B.3 Fluid analysis

The FE formulation and implementation of the Navier-Stokes equations including spin Eq. (9) and continuity equation are described as follows, which also serve as the supplement for Sec. 2.2.2.2 by simply setting $\boldsymbol{\omega}$ and ζ as zero. The derivation of Eq. (9) is briefly shown here [58], which is necessary for the derivation of the weak form. The linear momentum balance leads to the following equation

$$\rho \left(\frac{\partial \mathbf{V}}{\partial t} + \mathbf{V} \cdot \nabla \mathbf{V} \right) = \nabla \cdot \mathbf{T} + \mathbf{f} \tag{34}$$

The body force $\mathbf{f}$ has 3 components which are the three most right terms listed in Eq. (9)

$$\mathbf{f} = -\rho\mathbf{g} + \rho\mathbf{a_0}\cos(\omega t) - \sigma\kappa\nabla H(f) \tag{35}$$

The stress tensor $\mathbf{T}$ has 4 components shown below

$$\mathbf{T} = -P\mathbf{I} + \mathbf{T}_v + \mathbf{T}_a + \mathbf{T}_m \tag{36}$$

where T_v is a symmetric stress tensor related to viscosity

$$\mathbf{T}_v = \lambda(\nabla\cdot\mathbf{V})\mathbf{I} + \eta[\nabla\mathbf{V} + (\nabla\mathbf{V})^T] \tag{37}$$

$$\nabla\cdot\mathbf{T}_v = (\lambda+\eta)\nabla(\nabla\cdot\mathbf{V}) + \eta\nabla^2\mathbf{V} \tag{38}$$

For an incompressible fluid, the term $(\lambda+\eta)\nabla(\nabla\cdot\mathbf{V})$ is zero. $\mathbf{T}_a$ is an antisymmetric tensor existing in non-polar fluids and defined as a function of $\mathbf{A}$. $\mathbf{A}$ is the rate of conversion of external angular momentum to internal angular momentum as in Eq. (27).

$$\mathbf{T}_a = \frac{1}{2}\epsilon\cdot\mathbf{A} = \frac{1}{2}\epsilon_{ij3}\mathbf{e}_i\mathbf{e}_j A = \frac{1}{2}A(\mathbf{e}_1\mathbf{e}_2 - \mathbf{e}_2\mathbf{e}_1) \tag{39}$$

$$\begin{aligned}\nabla\cdot\mathbf{T}_a &= -\frac{1}{2}\nabla\times\mathbf{A} = -\frac{1}{2}\nabla\times 2\zeta(\nabla\times\mathbf{V} - 2\boldsymbol{\omega}) \\ &= -\zeta\nabla\times(\nabla\times\mathbf{V} - 2\boldsymbol{\omega}) = -\zeta\nabla(\nabla\cdot\mathbf{V}) + \zeta\nabla^2\mathbf{V} + 2\zeta\nabla\times\boldsymbol{\omega}\end{aligned} \tag{40}$$

The term $-\zeta\nabla(\nabla\cdot\mathbf{V})$ also vanishes. $\mathbf{T}_m$ is the magnetic stress tensor. For a dilute fluid, there is

$$\nabla\cdot\mathbf{T}_m = \mathbf{f}_m = \mu_0\mathbf{M}\cdot\nabla\mathbf{H} \tag{41}$$

In this work, the magnetic force is considered as a body force and written directly as $\mathbf{f}_m$. Substituting Eqs. (38, 40, 41) into Eq. (34), we obtain the four terms on the right hand side

of Eq. (9)

$$\nabla \cdot \mathbf{T} = -\nabla p + 2\zeta \nabla \times \boldsymbol{\omega} + (\eta + \zeta)\nabla^2 \mathbf{V} + \mu_0 \mathbf{M} \cdot \nabla \mathbf{H} \tag{42}$$

Define a stress tensor

$$\begin{aligned}\mathbf{T}' &= -p\mathbf{I} + \mathbf{T}_v + \mathbf{T}_a \\ &= \begin{bmatrix} -p + 2\eta \frac{\partial V_x}{\partial x} & \eta\left(\frac{\partial V_x}{\partial y} + \frac{\partial V_y}{\partial x}\right) + \zeta\left(\frac{\partial V_y}{\partial x} - \frac{\partial V_x}{\partial y} - 2\omega_z\right) \\ \eta\left(\frac{\partial V_x}{\partial y} + \frac{\partial V_y}{\partial x}\right) - \zeta\left(\frac{\partial V_y}{\partial x} - \frac{\partial V_x}{\partial y} - 2\omega_z\right) & -p + 2\eta\left(\frac{\partial V_y}{\partial y}\right) \end{bmatrix}\end{aligned} \tag{43}$$

and a vector

$$\mathbf{f}' = \mu_0 \mathbf{M} \cdot \nabla \mathbf{H} - \rho \mathbf{g} + \rho \mathbf{a_0} \cos(\omega t) - \sigma \kappa \nabla H(f) \tag{44}$$

There are apostrophes on $\mathbf{T}'$ and $\mathbf{f}'$ as the magnetic force is included in the body force instead of the stress tensor.

The weak form of the Navier-Stokes equations and continuity equation is given by SUPG+PSPG method as [62]

$$\begin{aligned}&\int_\Omega \mathbf{w} \cdot \left[\rho\left(\frac{\partial \mathbf{V}}{\partial t} + \mathbf{V} \cdot \nabla \mathbf{V}\right) - \mathbf{f}'\right] d\Omega + \int_\Omega \epsilon(\mathbf{w}) : \mathbf{T}' d\Omega + \int_\Omega q \nabla \cdot \mathbf{V} d\Omega \\ &+ \sum_{e=1}^{n_e} \int_{\Omega^e} \left(\tau_{SUPG} \mathbf{V} \cdot \nabla \mathbf{w} + \tau_{PSPG} \frac{1}{\rho} \nabla q\right) \cdot \left[\rho\left(\frac{\partial \mathbf{V}}{\partial t} + \mathbf{V} \cdot \nabla \mathbf{V}\right) - \nabla \cdot \mathbf{T}' - \mathbf{f}'\right] d\Omega \\ &+ \sum_{e=1}^{n_e} \int_{\Omega^e} \tau_{LSIC} \nabla \cdot \mathbf{w} \rho \nabla \cdot \mathbf{V} d\Omega = \int_\Gamma \mathbf{w} \cdot \mathbf{t} d\Gamma\end{aligned} \tag{45}$$

$\mathbf{w}$ and q denote weighting functions for velocity $\mathbf{V}$ and pressure P, respectively. Other variables include $\mathbf{T}'$-stress tensor, $\boldsymbol{\epsilon}$-strain tensor, $\mathbf{f}'$-body force, $\mathbf{t}$-surface traction on the boundary, τ_{SUPG}-SUPG stabilization parameter, τ_{PSPG}-PSPG stabilization parameter, and τ_{LSIC}-least-squares on incompressibility constant (LSIC) stabilization parameter. The av-

eraged ferrofluid density and viscosity in transition elements are defined as

$$\bar{\rho} = f\rho_1 + (1-f)\rho_2 \tag{46}$$

$$\bar{\eta} = f\eta_1 + (1-f)\eta_2 \tag{47}$$

The two element-level integrals in the formulation are the SUPG+PSPG stabilization terms for the momentum equation and least-squares stabilization term for the continuity equation, respectively. The coefficients are given as [62]

$$\tau_{SUPG} = \left[\left(\frac{2}{\Delta t} \right)^2 + \left(\frac{2|\mathbf{V}|}{h_e} \right)^2 + \left(\frac{4\nu}{h_e^2} \right)^2 \right]^{-\frac{1}{2}} \tag{48}$$

$$\tau_{PSPG} = \tau_{SUPG} \tag{49}$$

$$\tau_{LSIC} = \frac{h_e}{2}|\mathbf{V}| z(Re_e) \tag{50}$$

where ν-kinematic viscosity, h_e-element length, Re_e-element Reynolds number. h_e and Re_e are defined as

$$h_e = 2|\mathbf{V}| \left(\sum_{k=1}^{n_{en}} |\mathbf{V} \cdot \nabla N_k| \right)^{-1} \tag{51}$$

$$Re_e = \frac{|\mathbf{V}| h_e}{2\nu} \tag{52}$$

The function $z(Re_e)$ is defined as

$$z(Re_e) = \begin{cases} Re_e/3, & Re_e \leq 3 \\ 1, & Re_e > 3 \end{cases} \tag{53}$$

Projecting the weak form of the Navier-Stokes equations in the x direction gives

$$\int_\Omega \left[w_x \rho \left(\frac{\partial V_x}{\partial t} + V_x \frac{\partial V_x}{\partial x} + V_y \frac{\partial V_x}{\partial y} \right) - w_x f_x \right.$$
$$\left. + \frac{\partial w_x}{\partial x}(-p) + 2\eta \frac{\partial w_x}{\partial x}\frac{\partial V_x}{\partial x} + (\eta+\zeta)\frac{\partial w_x}{\partial y}\frac{\partial V_x}{\partial y} + (\eta-\zeta)\frac{\partial w_x}{\partial y}\frac{\partial V_y}{\partial x} + 2\zeta \frac{\partial w_x}{\partial y}\omega_z \right] d\Omega$$
$$+ \sum_{e=1}^{n_e} \int_{\Omega^e} \tau_{SUPG} \left(V_x \frac{\partial w_x}{\partial x} + V_y \frac{\partial w_y}{\partial y} \right) \cdot \left[\rho \left(\frac{\partial V_x}{\partial t} + V_x \frac{\partial V_x}{\partial x} + V_y \frac{\partial V_x}{\partial y} \right) \right.$$
$$\left. - (\eta+\zeta)\nabla^2 V_x - 2\zeta \frac{\partial \omega_z}{\partial y} + \frac{\partial P}{\partial x} - f_x \right] d\Omega$$
$$+ \sum_{e=1}^{n_e} \int_{\Omega^e} \tau_{LSIC} \rho \frac{\partial w_x}{\partial x} \left(\frac{\partial V_x}{\partial x} + \frac{\partial V_y}{\partial y} \right) d\Omega = \int_\Gamma w_x t_x d\Gamma \quad (54)$$

In the y direction

$$\int_\Omega \left[w_y \rho \left(\frac{\partial V_y}{\partial t} + V_x \frac{\partial V_y}{\partial x} + V_y \frac{\partial V_y}{\partial y} \right) - w_y f_y \right.$$
$$\left. + \frac{\partial w_y}{\partial y}(-p) + 2\eta \frac{\partial w_y}{\partial y}\frac{\partial V_y}{\partial y} + (\eta+\zeta)\frac{\partial w_y}{\partial x}\frac{\partial V_y}{\partial x} + (\eta-\zeta)\frac{\partial w_y}{\partial x}\frac{\partial V_x}{\partial y} - 2\zeta \frac{\partial w_y}{\partial x}\omega_z \right] d\Omega$$
$$+ \sum_{e=1}^{n_e} \int_{\Omega^e} \tau_{SUPG} \left(V_x \frac{\partial w_x}{\partial x} + V_y \frac{\partial w_y}{\partial y} \right) \cdot \left[\rho \left(\frac{\partial V_y}{\partial t} + V_x \frac{\partial V_y}{\partial x} + V_y \frac{\partial V_y}{\partial y} \right) \right.$$
$$\left. - (\eta+\zeta)\nabla^2 V_y + 2\zeta \frac{\partial \omega_z}{\partial x} + \frac{\partial P}{\partial y} - f_y \right] d\Omega$$
$$+ \sum_{e=1}^{n_e} \int_{\Omega^e} \tau_{LSIC} \rho \frac{\partial w_y}{\partial y} \left(\frac{\partial V_x}{\partial x} + \frac{\partial V_y}{\partial y} \right) d\Omega = \int_\Gamma w_y t_y d\Gamma \quad (55)$$

The weak form of continuity equation is as follows

$$\int_{\Omega} q\left(\frac{\partial V_x}{\partial x}+\frac{\partial V_y}{\partial y}\right)+\sum_{e=1}^{ne}\int_{\Omega^e}\tau_{PSPG}\frac{\partial q}{\partial x}\cdot\left[\rho\left(\frac{\partial V_x}{\partial t}+V_x\frac{\partial V_x}{\partial x}+V_y\frac{\partial V_x}{\partial y}\right)\right.$$
$$\left.-(\eta+\zeta)\nabla^2 V_x-2\zeta\frac{\partial \omega_z}{\partial y}+\frac{\partial P}{\partial x}-f_x\right]d\Omega$$
$$+\sum_{e=1}^{ne}\int_{\Omega^e}\tau_{PSPG}\frac{\partial q}{\partial y}\cdot\left[\rho\left(\frac{\partial V_y}{\partial t}+V_x\frac{\partial V_y}{\partial x}+V_y\frac{\partial V_y}{\partial y}\right)\right.$$
$$\left.-(\eta+\zeta)\nabla^2 V_y+2\zeta\frac{\partial \omega_z}{\partial x}+\frac{\partial P}{\partial y}-f_y\right]d\Omega=0 \quad (56)$$

$\nabla^2 V_x$ and $\nabla^2 V_y$ are trivial when linear elements are used [64] (p237).

The finite element discretization of the weak form of the Navier-Stokes equations follows a similar procedure as described for the magnetic analysis. Linear elements are used to solve the Navier-Stokes and continuity equations. The quadratic elements inside the tank for magnetic analysis are converted to linear elements for sloshing dynamics analysis by taking only the vertices (neglecting the edge nodes). In this way, the magnetic and sloshing dynamics analyses share the same mesh in the tank. After the standard FE discretization, the weak form can be rewritten in a matrix form similar to that obtained in Ref.

[63]

$$\left(\begin{bmatrix}\mathbf{M}_{11} & 0\\ 0 & \mathbf{M}_{11}\end{bmatrix}+\begin{bmatrix}\mathbf{M}_{s11} & 0\\ 0 & \mathbf{M}_{s11}\end{bmatrix}\right)\begin{bmatrix}\mathbf{a}_x\\ \mathbf{a}_y\end{bmatrix}+\left(\begin{bmatrix}\mathbf{C}_{11} & 0\\ 0 & \mathbf{C}_{11}\end{bmatrix}+\begin{bmatrix}\mathbf{C}_{s11} & 0\\ 0 & \mathbf{C}_{s11}\end{bmatrix}\right)\begin{bmatrix}\mathbf{v}_x\\ \mathbf{v}_y\end{bmatrix}+\left(\begin{bmatrix}\mathbf{D}_{11} & \mathbf{D}_{12}\\ \mathbf{D}_{21} & \mathbf{D}_{22}\end{bmatrix}+\begin{bmatrix}\mathbf{B}_{c11} & \mathbf{B}_{c12}\\ \mathbf{B}_{c21} & \mathbf{B}_{c22}\end{bmatrix}\right)\begin{bmatrix}\mathbf{v}_x\\ \mathbf{v}_y\end{bmatrix}-\left(\begin{bmatrix}\mathbf{G}_1\\ \mathbf{G}_2\end{bmatrix}-\begin{bmatrix}\mathbf{G}_{s1}\\ \mathbf{G}_{s2}\end{bmatrix}\right)\mathbf{p}=\begin{bmatrix}\mathbf{f}_1\\ \mathbf{f}_2\end{bmatrix}+\begin{bmatrix}\mathbf{f}_{s1}\\ \mathbf{f}_{s2}\end{bmatrix} \tag{57}$$

$$\begin{bmatrix}\mathbf{G}_1^T & \mathbf{G}_2^T\end{bmatrix}\begin{bmatrix}\mathbf{v}_x\\ \mathbf{v}_y\end{bmatrix}+\begin{bmatrix}\mathbf{M}_{p1} & \mathbf{M}_{p2}\end{bmatrix}\begin{bmatrix}\mathbf{a}_x\\ \mathbf{a}_y\end{bmatrix}+\begin{bmatrix}\mathbf{C}_{p1} & \mathbf{C}_{p2}\end{bmatrix}\begin{bmatrix}\mathbf{v}_x\\ \mathbf{v}_y\end{bmatrix}+\mathbf{G}_p\mathbf{p}=\mathbf{f}_p \tag{58}$$

where $\mathbf{v}$, $\mathbf{a}$ and $\mathbf{p}$ are the vectors of unknown nodal values of velocity, acceleration and pressure, respectively. The matrices $\mathbf{M}$, $\mathbf{C}(\mathbf{v})$, $\mathbf{D}$ and $\mathbf{G}$ are derived from mass, convective, viscous and pressure terms, respectively. $\mathbf{f}$ is related to the body forces and natural boundary conditions. The subscripts s and p represent terms derived from SUPG stabilization terms and PSPG stabilization terms, respectively. $\mathbf{B}_c$ is obtained from the least-squares stabilization term. The matrices are calculated as follows.

$$\mathbf{M}_{11}=\int \rho\mathbf{N}\mathbf{N}^T d\Omega \tag{59}$$

$$\mathbf{M}_{s11}=\int \tau_{SUPG}\rho\left(v_x\frac{\partial\mathbf{N}}{\partial x}+v_y\frac{\partial\mathbf{N}}{\partial y}\right)\mathbf{N}^T d\Omega \tag{60}$$

$$\mathbf{C}_{11}=\int \rho\mathbf{N}\left(v_x\frac{\partial\mathbf{N}}{\partial x}+v_y\frac{\partial\mathbf{N}}{\partial y}\right)^T d\Omega \tag{61}$$

$$\mathbf{C}_{s11}=\int \tau_{SUPG}\rho\left(v_x\frac{\partial\mathbf{N}}{\partial x}+v_y\frac{\partial\mathbf{N}}{\partial y}\right)\left(v_x\frac{\partial\mathbf{N}}{\partial x}+v_y\frac{\partial\mathbf{N}}{\partial y}\right)^T d\Omega \tag{62}$$

$$\mathbf{D}_{11} = \int \left[2\eta \frac{\partial \mathbf{N}}{\partial x} \frac{\partial \mathbf{N}}{\partial x}^T + (\eta + \zeta) \frac{\partial \mathbf{N}}{\partial y} \frac{\partial \mathbf{N}}{\partial y}^T \right] d\Omega \tag{63}$$

$$\mathbf{D}_{12} = \int (\eta - \zeta) \frac{\partial \mathbf{N}}{\partial y} \frac{\partial \mathbf{N}}{\partial x}^T d\Omega \tag{64}$$

$$\mathbf{D}_{21} = \mathbf{D}_{12}^T \tag{65}$$

$$\mathbf{D}_{22} = \int \left[2\eta \frac{\partial \mathbf{N}}{\partial y} \frac{\partial \mathbf{N}}{\partial y}^T + (\eta + \zeta) \frac{\partial \mathbf{N}}{\partial x} \frac{\partial \mathbf{N}}{\partial x}^T \right] d\Omega \tag{66}$$

$$\mathbf{B}_{c11} = \int \tau_{LSIC} \rho \frac{\partial \mathbf{N}}{\partial x} \frac{\partial \mathbf{N}}{\partial x}^T d\Omega \tag{67}$$

$$\mathbf{B}_{c12} = \int \tau_{LSIC} \rho \frac{\partial \mathbf{N}}{\partial x} \frac{\partial \mathbf{N}}{\partial y}^T d\Omega \tag{68}$$

$$\mathbf{B}_{c21} = \mathbf{B}_{c12}^T \tag{69}$$

$$\mathbf{B}_{c22} = \int \tau_{LSIC} \rho \frac{\partial \mathbf{N}}{\partial y} \frac{\partial \mathbf{N}}{\partial y}^T d\Omega \tag{70}$$

$$\mathbf{G}_1 = \int \frac{\partial \mathbf{N}}{\partial x} \mathbf{N}^T d\Omega \tag{71}$$

$$\mathbf{G}_2 = \int \frac{\partial \mathbf{N}}{\partial y} \mathbf{N}^T d\Omega \tag{72}$$

$$\mathbf{G}_{s1} = \int \tau_{SUPG} \left(v_x \frac{\partial \mathbf{N}}{\partial x} + v_y \frac{\partial \mathbf{N}}{\partial y} \right) \frac{\partial \mathbf{N}}{\partial x}^T d\Omega \tag{73}$$

$$\mathbf{G}_{s2} = \int \tau_{SUPG} \left(v_x \frac{\partial \mathbf{N}}{\partial x} + v_y \frac{\partial \mathbf{N}}{\partial y} \right) \frac{\partial \mathbf{N}}{\partial y}^T d\Omega \tag{74}$$

$$\mathbf{f}_1 = \int \left(\mathbf{N} f_x - 2\zeta \frac{\partial \mathbf{N}}{\partial y} \omega_z \right) d\Omega \tag{75}$$

$$\mathbf{f}_2 = \int \left(\mathbf{N} f_y + 2\zeta \frac{\partial \mathbf{N}}{\partial x} \omega_z \right) d\Omega \tag{76}$$

$$\mathbf{f}_{s1} = \int \tau_{SUPG} \left(v_x \frac{\partial \mathbf{N}}{\partial x} + v_y \frac{\partial \mathbf{N}}{\partial y} \right) \left(f_x + 2\zeta \frac{\partial \omega_z}{\partial y} \right) d\Omega \tag{77}$$

$$\mathbf{f}_{s2} = \int \tau_{SUPG} \left(v_x \frac{\partial \mathbf{N}}{\partial x} + v_y \frac{\partial \mathbf{N}}{\partial y} \right) \left(f_y - 2\zeta \frac{\partial \omega_z}{\partial x} \right) d\Omega \tag{78}$$

$$\mathbf{M}_{p1} = \int \tau_{PSPG} \rho \frac{\partial \mathbf{N}}{\partial x} \mathbf{N}^T d\Omega \tag{79}$$

$$\mathbf{M}_{p2} = \int \tau_{PSPG} \rho \frac{\partial \mathbf{N}}{\partial y} \mathbf{N}^T d\Omega \tag{80}$$

$$\mathbf{C}_{p1} = \int \tau_{PSPG} \rho \frac{\partial \mathbf{N}}{\partial x} \left(v_x \frac{\partial \mathbf{N}}{\partial x} + v_y \frac{\partial \mathbf{N}}{\partial y} \right)^T d\Omega \tag{81}$$

$$\mathbf{C}_{p2} = \int \tau_{PSPG} \rho \frac{\partial \mathbf{N}}{\partial y} \left(v_x \frac{\partial \mathbf{N}}{\partial x} + v_y \frac{\partial \mathbf{N}}{\partial y} \right)^T d\Omega \tag{82}$$

$$\mathbf{G}_p = \int \tau_{PSPG} \left(\frac{\partial \mathbf{N}}{\partial x} \frac{\partial \mathbf{N}}{\partial x}^T + \frac{\partial \mathbf{N}}{\partial y} \frac{\partial \mathbf{N}}{\partial y}^T \right) d\Omega \tag{83}$$

$$\mathbf{f}_p = \int \tau_{PSPG} \left(\frac{\partial \mathbf{N}}{\partial x} f_x + \frac{\partial \mathbf{N}}{\partial y} f_y + 2\zeta \frac{\partial \mathbf{N}}{\partial x} \frac{\partial \omega_z}{\partial y} - 2\zeta \frac{\partial \mathbf{N}}{\partial y} \frac{\partial \omega_z}{\partial x} \right) d\Omega \tag{84}$$

The matrix form can be written in a more concise way as [63] (p16)

$$(\mathbf{M} + \mathbf{M}_s)\mathbf{a} + [\mathbf{C}(\mathbf{v}) + \mathbf{C}_s(\mathbf{v})]\mathbf{v} + (\mathbf{D} + \mathbf{B}_c)\mathbf{v} - [\mathbf{G} - \mathbf{G}_s]\mathbf{p} = \mathbf{f} + \mathbf{f}_s \tag{85}$$

$$\mathbf{G}^T\mathbf{v} + \mathbf{M}_p\mathbf{a} + \mathbf{C}_p(\mathbf{v})\mathbf{v} + \mathbf{G}_p\mathbf{p} = \mathbf{f}_p \tag{86}$$

In the dynamic analysis, the predictor-corrector algorithm is used to solve for unknown variables at time t_{n+1} from t_n [64]. The first step is to calculate the predicted values

$\mathbf{v}_{n+1}^{(0)}$, $\mathbf{p}_{n+1}^{(0)}$ using values from t_n and set $\mathbf{a}_{n+1}^{(0)}$, $\dot{\mathbf{p}}_{n+1}^{(0)}$ zero.

$$\mathbf{v}_{n+1}^{(0)} = \mathbf{v}_n + \Delta t(1-\beta)\mathbf{a}_n \tag{87}$$

$$\mathbf{a}_{n+1}^{(0)} = 0 \tag{88}$$

$$\mathbf{p}_{n+1}^{(0)} = \mathbf{p}_n + \Delta t(1-\beta)\dot{\mathbf{p}}_n \tag{89}$$

$$\dot{\mathbf{p}}_{n+1}^{(0)} = 0 \tag{90}$$

The predicted values are corrected in these ways,

$$\mathbf{v}^{(i+1)} = \mathbf{v}^{(i)} + \beta\Delta t\Delta\mathbf{a}^{(i)} \tag{91}$$

$$\mathbf{a}^{(i+1)} = \mathbf{a}^{(i)} + \Delta\mathbf{a}^{(i)} \tag{92}$$

$$\mathbf{p}^{(i+1)} = \mathbf{p}^{(i)} + \Delta\mathbf{p}^{(i)} \tag{93}$$

$$\dot{\mathbf{p}}^{(i+1)} = \dot{\mathbf{p}}^{(i)} + (\Delta\mathbf{p}^{(i)})/(\beta\Delta t) \tag{94}$$

At (i+1)th iteration, Eqs. (85, 86) lead to the following equations.

$$\begin{aligned}(\mathbf{M}+\mathbf{M}_s)\mathbf{a}^{(i+1)} + [\mathbf{C}(\mathbf{v}^{(i+1)}) + \mathbf{C}_s(\mathbf{v}^{(i+1)})]\mathbf{v}^{(i+1)} \\ +(\mathbf{D}+\mathbf{B}_c)\mathbf{v}^{(i+1)} - [\mathbf{G}-\mathbf{G}_s]\mathbf{p}^{(i+1)} = \mathbf{f}^{(i+1)} + \mathbf{f}_s^{(i+1)}\end{aligned} \tag{95}$$

$$\mathbf{G}^T\mathbf{v}^{(i+1)} + \mathbf{M}_p\mathbf{a}^{(i+1)} + \mathbf{C}_p(\mathbf{v}^{(i+1)})\mathbf{v}^{(i+1)} + \mathbf{G}_p\mathbf{p}^{(i+1)} = \mathbf{f}_p^{(i+1)} \tag{96}$$

According to Taylor series, the 2nd term in Eq. (95) can be written as

$$\begin{aligned}[\mathbf{C}^{(i+1)} + \mathbf{C}_s^{(i+1)}]\mathbf{v}^{(i+1)} &\approx (\mathbf{C}^{(i)} + \mathbf{C}_s^{(i)})\mathbf{v}^{(i)} + \frac{d[(\mathbf{C}^{(i)} + \mathbf{C}_s^{(i)})\mathbf{v}^{(i)}]}{d\mathbf{v}^{(i)}}\Delta\mathbf{v}^{(i)} \\ &= (\mathbf{C}^{(i)} + \mathbf{C}_s^{(i)})\mathbf{v}^{(i)} + \frac{d[(\mathbf{C}^{(i)} + \mathbf{C}_s^{(i)})\mathbf{v}^{(i)}]}{d\mathbf{v}^{(i)}}\beta\Delta t\Delta\mathbf{a}^{(i)}\end{aligned} \tag{97}$$

In the same way, the 3rd term in Eq. (96) can be written as

$$\mathbf{C}_p^{(i+1)}\mathbf{v}^{(i+1)} = \mathbf{C}_p^{(i)}\mathbf{v}^{(i)} + \frac{d(\mathbf{C}_p^{(i)}\mathbf{v}^{(i)})}{d\mathbf{v}^{(i)}}\beta\Delta t\Delta\mathbf{a}^{(i)} \tag{98}$$

When written in an incremental form, the weak form takes the following format. Since the acceleration is zero at the first iteration, at least 2 iterations (I=2) are required to take into consideration the effect of mass matrix [64] (p17).

$$\mathbf{M}'\Delta\mathbf{a}^{(i)} - \mathbf{G}'\Delta\mathbf{p}^{(i)} = \mathbf{R}^{(i+1)} \tag{99}$$

$$\mathbf{H}'\Delta\mathbf{a}^{(i)} + \mathbf{G}_p\Delta\mathbf{p}^{(i)} = \mathbf{Q}^{(i+1)} \tag{100}$$

where

$$\begin{aligned}\mathbf{R}^{(i+1)} =& \mathbf{f}^{(i+1)} + \mathbf{f}_s^{(i+1)} - [\ (\mathbf{M}+\mathbf{M}_s)\mathbf{a}^{(i)} + (\mathbf{C}^{(i)} + \mathbf{C}_s^{(i)})\mathbf{v}^{(i)} \\ &+ (\mathbf{D}+\mathbf{B}_c)\mathbf{v}^{(i)} - (\mathbf{G}-\mathbf{G}_s)\mathbf{p}^{(i)}\ ]\end{aligned} \tag{101}$$

$$\mathbf{Q}^{(i+1)} = F_p^{(i+1)} - (\mathbf{G}^T\mathbf{v}^{(i)} + \mathbf{M}_p\mathbf{a}^{(i)} + \mathbf{C}_p^{(i)}\mathbf{v}^{(i)} + \mathbf{G}_p\mathbf{p}^{(i)}) \tag{102}$$

$$\mathbf{M}'^{(i+1)} = \mathbf{M} + \mathbf{M}_s + \beta\Delta t\left[\frac{d(\mathbf{C}^{(i)}\mathbf{v}^{(i)})}{d\mathbf{v}^{(i)}} + \frac{d(\mathbf{C}_s^{(i)}\mathbf{v}^{(i)})}{d\mathbf{v}^{(i)}} + \mathbf{D} + \mathbf{B}_c\right] \tag{103}$$

$$\mathbf{G}' = \mathbf{G} - \mathbf{G}_s \tag{104}$$

$$\mathbf{H}'^{(i+1)} = \mathbf{M}_p + \beta\Delta t\left[\frac{d(\mathbf{C}_p^{(i)}\mathbf{v}^{(i)})}{d\mathbf{v}^{(i)}} + \mathbf{G}^T\right] \tag{105}$$

Now let's look at the how to calculate the nonlinear term $\frac{d(\mathbf{C}\mathbf{v})}{d\mathbf{v}}$

$$\mathbf{C}\mathbf{v} = \begin{bmatrix}\mathbf{C}_{11} & 0\\ 0 & \mathbf{C}_{11}\end{bmatrix}\begin{bmatrix}\mathbf{v}_x\\ \mathbf{v}_y\end{bmatrix} = \begin{bmatrix}\mathbf{C}_{11}\mathbf{v}_x\\ \mathbf{C}_{11}\mathbf{v}_y\end{bmatrix} \tag{106}$$

So

$$\frac{d(\mathbf{C}\mathbf{v})}{d\mathbf{v}} = \begin{bmatrix} \frac{d(\mathbf{C}_{11}\mathbf{v}_x)}{d\mathbf{v}_x} & \frac{d(\mathbf{C}_{11}\mathbf{v}_x)}{d\mathbf{v}_y} \\ \frac{d(\mathbf{C}_{11}\mathbf{v}_y)}{d\mathbf{v}_x} & \frac{d(\mathbf{C}_{11}\mathbf{v}_y)}{d\mathbf{v}_y} \end{bmatrix} \tag{107}$$

From Eq. (61) it can be seen that

$$\mathbf{C}_{11}\mathbf{v}_x = \int \rho\mathbf{N}\left(v_x\frac{\partial\mathbf{N}}{\partial x} + v_y\frac{\partial\mathbf{N}}{\partial y}\right)^T d\Omega\cdot\mathbf{v}_x \tag{108}$$

The a-th row of $\mathbf{C}_{11}\mathbf{v}_x$ is

$$(\mathbf{C}_{11}\mathbf{v}_x)_a = \int \rho N_a\left[\sum_{c=1}^{n_{en}}\left(v_x\frac{\partial N_c}{\partial x} + v_y\frac{\partial N_c}{\partial y}\right)v_{xc}\right]d\Omega \tag{109}$$

Taking the derivative of $(\mathbf{C}_{11}\mathbf{v}_x)_a$ with respect to v_{xb} gives

$$\frac{d(\mathbf{C}_{11}\mathbf{v}_x)_a}{dv_{xb}} = \int \rho N_a\left[\sum_{c=1}^{n_{en}}\left(N_b\frac{\partial N_c}{\partial x}\right)v_{xc}\right]d\Omega + \int \rho N_a\left(v_x\frac{\partial N_b}{\partial x} + v_y\frac{\partial N_b}{\partial y}\right)d\Omega \tag{110}$$

Thus

$$\frac{d(\mathbf{C}_{11}\mathbf{v}_x)}{d\mathbf{v}_x} = \int \rho\mathbf{N}\mathbf{N}^T\left(\frac{\partial v_x}{\partial x}\right)d\Omega + \mathbf{C}_{11} \tag{111}$$

In similar ways,

$$\frac{d(\mathbf{C}_{11}\mathbf{v}_x)}{d\mathbf{v}_y} = \int \rho\mathbf{N}\mathbf{N}^T\left(\frac{\partial v_x}{\partial y}\right)d\Omega \tag{112}$$

$$\frac{d(\mathbf{C}_{11}\mathbf{v}_y)}{d\mathbf{v}_x} = \int \rho\mathbf{N}\mathbf{N}^T\left(\frac{\partial v_y}{\partial x}\right)d\Omega \tag{113}$$

$$\frac{d(\mathbf{C}_{11}\mathbf{v}_y)}{d\mathbf{v}_y} = \int \rho\mathbf{N}\mathbf{N}^T\left(\frac{\partial v_y}{\partial y}\right)d\Omega + \mathbf{C}_{11} \tag{114}$$

For the nonlinear term $\frac{d(\mathbf{C}_s\mathbf{v})}{d\mathbf{v}}$, from Eq. (62) it can be seen that

$$\mathbf{C}_{s11}\mathbf{v}_x = \int \tau_{SUPG}\rho \left(v_x \frac{\partial \mathbf{N}}{\partial x} + v_y \frac{\partial \mathbf{N}}{\partial y} \right) \left(v_x \frac{\partial \mathbf{N}}{\partial x} + v_y \frac{\partial \mathbf{N}}{\partial y} \right)^T d\Omega \cdot \mathbf{v}_x \tag{115}$$

The a-th row of $\mathbf{C}_{s11}\mathbf{v}_x$ is

$$(\mathbf{C}_{s11}\mathbf{v}_x)_a = \int \tau_{SUPG}\rho \left(v_x \frac{\partial N_a}{\partial x} + v_y \frac{\partial N_a}{\partial y} \right) \left[\sum_{c=1}^{n} \left(v_x \frac{\partial N_c}{\partial x} + v_y \frac{\partial N_c}{\partial y} \right) v_{xc} \right] d\Omega \tag{116}$$

Taking the derivative with respect to v_{xb}

$$\begin{aligned} \frac{d(\mathbf{C}_{s11}\mathbf{v}_x)_a}{dv_{xb}} = & \int \tau_{SUPG}\rho \left(N_b \frac{\partial N_a}{\partial x} \right) \left[\sum_{c=1}^{n} \left(v_x \frac{\partial N_c}{\partial x} + v_y \frac{\partial N_c}{\partial y} \right) v_{xc} \right] d\Omega \\ & + \int \tau_{SUPG}\rho \left(v_x \frac{\partial N_a}{\partial x} + v_y \frac{\partial N_a}{\partial y} \right) \left[\sum_{c=1}^{n} \left(N_b \frac{\partial N_c}{\partial x} \right) v_{xc} \right] d\Omega \\ & + \int \tau_{SUPG}\rho \left(v_x \frac{\partial N_a}{\partial x} + v_y \frac{\partial N_a}{\partial y} \right) \left(v_x \frac{\partial N_b}{\partial x} + v_y \frac{\partial N_b}{\partial y} \right) d\Omega \end{aligned} \tag{117}$$

Thus

$$\begin{aligned} \frac{d(\mathbf{C}_{s11}\mathbf{v}_x)}{d\mathbf{v}_x} = & \int \tau_{SUPG}\rho \left(\frac{\partial \mathbf{N}}{\partial x} \mathbf{N}^T \right) \left[\left(v_x \frac{\partial \mathbf{N}}{\partial x} + v_y \frac{\partial \mathbf{N}}{\partial y} \right)^T \mathbf{v}_x \right] d\Omega \\ & + \int \tau_{SUPG}\rho \left(v_x \frac{\partial \mathbf{N}}{\partial x} + v_y \frac{\partial \mathbf{N}}{\partial y} \right) \mathbf{N}^T \left(\frac{\partial v_x}{\partial x} \right) d\Omega + \mathbf{C}_{s11} \end{aligned} \tag{118}$$

Similarly,

$$\frac{d(\mathbf{C}_{s11}\mathbf{v}_x)}{d\mathbf{v}_y} = \int \tau_{SUPG}\rho\left(\frac{\partial \mathbf{N}}{\partial y}\mathbf{N}^T\right)\left[\left(v_x\frac{\partial \mathbf{N}}{\partial x}+v_y\frac{\partial \mathbf{N}}{\partial y}\right)^T\mathbf{v}_x\right]d\Omega + \int \tau_{SUPG}\rho\left(v_x\frac{\partial \mathbf{N}}{\partial x}+v_y\frac{\partial \mathbf{N}}{\partial y}\right)\mathbf{N}^T\left(\frac{\partial v_x}{\partial y}\right)d\Omega \tag{119}$$

$$\frac{d(\mathbf{C}_{s11}\mathbf{v}_y)}{d\mathbf{v}_x} = \int \tau_{SUPG}\rho\left(\frac{\partial \mathbf{N}}{\partial x}\mathbf{N}^T\right)\left[\left(v_x\frac{\partial \mathbf{N}}{\partial x}+v_y\frac{\partial \mathbf{N}}{\partial y}\right)^T\mathbf{v}_y\right]d\Omega + \int \tau_{SUPG}\rho\left(v_x\frac{\partial \mathbf{N}}{\partial x}+v_y\frac{\partial \mathbf{N}}{\partial y}\right)\mathbf{N}^T\left(\frac{\partial v_y}{\partial x}\right)d\Omega \tag{120}$$

$$\frac{d(\mathbf{C}_{s11}\mathbf{v}_y)}{d\mathbf{v}_y} = \int \tau_{SUPG}\rho\left(\frac{\partial \mathbf{N}}{\partial y}\mathbf{N}^T\right)\left[\left(v_x\frac{\partial \mathbf{N}}{\partial x}+v_y\frac{\partial \mathbf{N}}{\partial y}\right)^T\mathbf{v}_y\right]d\Omega + \int \tau_{SUPG}\rho\left(v_x\frac{\partial \mathbf{N}}{\partial x}+v_y\frac{\partial \mathbf{N}}{\partial y}\right)\mathbf{N}^T\left(\frac{\partial v_y}{\partial y}\right)d\Omega + \mathbf{C}_{s11} \tag{121}$$

The 3rd nonlinear term $\frac{d(\mathbf{C}_p\mathbf{v})}{d\mathbf{v}}$ is computed in the following way.

$$\mathbf{C}_p(\mathbf{v})\mathbf{v} = \begin{bmatrix}\mathbf{C}_{p1} & \mathbf{C}_{p2}\end{bmatrix}\begin{bmatrix}\mathbf{v}_x \\ \\ \mathbf{v}_y\end{bmatrix} = \mathbf{C}_{p1}\mathbf{v}_x + \mathbf{C}_{p2}\mathbf{v}_y \tag{122}$$

$$\frac{d(\mathbf{C}_p\mathbf{v})}{d\mathbf{v}} = \begin{bmatrix}\frac{d(\mathbf{C}_{p1}\mathbf{v}_x+\mathbf{C}_{p2}\mathbf{v}_y)}{d\mathbf{v}_x} & \frac{d(\mathbf{C}_{p1}\mathbf{v}_x+\mathbf{C}_{p2}\mathbf{v}_y)}{d\mathbf{v}_y}\end{bmatrix} \tag{123}$$

From Eqs. (81, 82), it is clear that

$$\mathbf{C}_{p1}\mathbf{v}_x + \mathbf{C}_{p2}\mathbf{v}_y = \int \tau_{PSPG}\rho\frac{\partial \mathbf{N}}{\partial x}\left(v_x\frac{\partial \mathbf{N}}{\partial x}+v_y\frac{\partial \mathbf{N}}{\partial y}\right)^T d\Omega\cdot\mathbf{v}_x + \int \tau_{PSPG}\rho\frac{\partial \mathbf{N}}{\partial y}\left(v_x\frac{\partial \mathbf{N}}{\partial x}+v_y\frac{\partial \mathbf{N}}{\partial y}\right)^T d\Omega\cdot\mathbf{v}_y \tag{124}$$

And then

$$\frac{d(\mathbf{C}_p\mathbf{v})}{d\mathbf{v}_x} = \int \tau_{PSPG}\rho\frac{\partial\mathbf{N}}{\partial x}\mathbf{N}^T\frac{\partial v_x}{\partial x}d\Omega + \mathbf{C}_{p1} + \int \tau_{PSPG}\rho\frac{\partial\mathbf{N}}{\partial y}\mathbf{N}^T\frac{\partial v_y}{\partial x}d\Omega \tag{125}$$

$$\frac{d(\mathbf{C}_p\mathbf{v})}{d\mathbf{v}_y} = \int \tau_{PSPG}\rho\frac{\partial\mathbf{N}}{\partial x}\mathbf{N}^T\frac{\partial v_x}{\partial y}d\Omega + \int \tau_{PSPG}\rho\frac{\partial\mathbf{N}}{\partial y}\mathbf{N}^T\frac{\partial v_y}{\partial y}d\Omega + \mathbf{C}_{p2} \tag{126}$$

When $\Delta\mathbf{a}^{(i)}$, $\Delta\mathbf{p}^{(i)}$ are calculated, predicted values are corrected according to Eqs. (91-94).

Bibliography

[1] Y. Shu and I. Lien, "Analysis of power output for piezoelectric energy harvesting systems," *Smart materials and structures*, vol. 15, no. 6, p. 1499, 2006.

[2] T. Seuaciuc-Osório and M. F. Daqaq, "On the reduced-order modeling of energy harvesters," *Journal of Intelligent Material Systems and Structures*, vol. 20, no. 16, pp. 2003–2016, 2009.

[3] S. Roundy, P. K. Wright, and K. S. Pister, "Micro-electrostatic vibration-to-electricity converters," in *ASME 2002 International Mechanical Engineering Congress and Exposition*, pp. 487–496, American Society of Mechanical Engineers, 2002.

[4] A. Perez-Rodriguez, C. Serre, N. Fondevilla, C. Cereceda, J. Morante, J. Esteve, and J. Montserrat, "Design of electromagnetic inertial generators for energy scavenging applications," *Proc. Eurosensors XIX (Barcelona, Spain)*, 2005.

[5] D. Liu and P. Lin, "A numerical study of three-dimensional liquid sloshing in tanks," *Journal of Computational Physics*, vol. 227, no. 8, pp. 3921–3939, 2008.

[6] J. A. Paradiso and T. Starner, "Energy scavenging for mobile and wireless electronics," *IEEE Pervasive computing*, vol. 4, no. 1, pp. 18–27, 2005.

[7] V. Raghunathan, C. Schurgers, S. Park, and M. B. Srivastava, "Energy-aware wireless microsensor networks," *IEEE Signal processing magazine*, vol. 19, no. 2, pp. 40–50, 2002.

[8] S. P. Beeby, M. J. Tudor, and N. M. White, "Energy harvesting vibration sources for microsystems applications," *Measurement science and technology*, vol. 17, no. 12, p. R175, 2006.

[9] A. Khaligh, P. Zeng, and C. Zheng, "Kinetic energy harvesting using piezoelectric and electromagnetic technologies—state of the art," *Industrial Electronics, IEEE Transactions*, vol. 57, no. 3, pp. 850–860, 2010.

[10] A. Harb, "Energy harvesting: State-of-the-art," *Renewable Energy*, vol. 36, no. 10, pp. 2641–2654, 2011.

[11] D. St. Clair, A. Bibo, V. Sennakesavababu, M. Daqaq, and G. Li, "A scalable concept for micropower generation using flow-induced self-excited oscillations," *Applied Physics Letters*, vol. 96, no. 14, p. 144103, 2010.

[12] A. Bibo, G. Li, and M. F. Daqaq, "Electromechanical modeling and normal form analysis of an aeroelastic micro-power generator," *Journal of Intelligent Material Systems and Structures*, vol. 22, no. 6, pp. 577–592, 2011.

[13] A. Bibo, G. Li, and M. F. Daqaq, "Performance analysis of a harmonica-type aeroelastic micropower generator," *Journal of Intelligent Material Systems and Structures*, vol. 23, no. 13, pp. 1461–1474, 2012.

[14] J. Noel, R. Yadav, G. Li, and M. Daqaq, "Improving the performance of galloping micro-power generators by passively manipulating the trailing edge," *Applied Physics Letters*, vol. 112, no. 8, p. 083503, 2018.

[15] L. Wang and F. Yuan, "Vibration energy harvesting by magnetostrictive material," *Smart Materials and Structures*, vol. 17, no. 4, p. 045009, 2008.

[16] A. Triplett and D. D. Quinn, "The effect of non-linear piezoelectric coupling on vibration-based energy harvesting," *Journal of Intelligent Material Systems and Structures*, vol. 20, no. 16, pp. 1959–1967, 2009.

[17] M. Li, Y. Wen, P. Li, J. Yang, and X. Dai, "A rotation energy harvester employing cantilever beam and magnetostrictive/piezoelectric laminate transducer," *Sensors and Actuators A: Physical*, vol. 166, no. 1, pp. 102–110, 2011.

[18] M. El-Hami, P. Glynne-Jones, N. M. White, M. Hill, S. P. Beeby, E. James, A. D. Brown, and J. N. Ross, "Design and fabrication of a new vibration-based electromechanical power generator," *Sensors and Actuators A: Physical*, vol. 92, no. 1, pp. 335–342, 2001.

[19] P. Glynne-Jones, M. J. Tudor, S. P. Beeby, and N. M. White, "An electromagnetic, vibration-powered generator for intelligent sensor systems," *Sensors and Actuators A: Physical*, vol. 110, no. 1, pp. 344–349, 2004.

[20] A. R. M. Foisal, C. Hong, and G.-S. Chung, "Multi-frequency electromagnetic energy harvester using a magnetic spring cantilever," *Sensors and Actuators A: Physical*, vol. 182, pp. 106–113, 2012.

[21] Y. Wang, Q. Zhang, L. Zhao, and E. S. Kim, "Non-resonant electromagnetic broadband vibration-energy harvester based on self-assembled ferrofluid liquid bearing," *Journal of Microelectromechanical Systems*, vol. 26, no. 4, pp. 809–819, 2017.

[22] S. Wang and D. Li, "Design and analysis of a plane vibration-based electromagnetic generator using a magnetic spring and ferrofluid," *Journal of the Korean Physical Society*, vol. 67, no. 5, pp. 818–822, 2015.

[23] S. H. Chae, S. Ju, Y. Choi, Y.-E. Chi, and C.-H. Ji, "Electromagnetic linear vibration energy harvester using sliding permanent magnet array and ferrofluid as a lubricant," *Micromachines*, vol. 8, no. 10, p. 288, 2017.

[24] S. Wu, P. Luk, C. Li, X. Zhao, and Z. Jiao, "Investigation of an electromagnetic wearable resonance kinetic energy harvester with ferrofluid," *IEEE Transactions on Magnetics*, vol. 53, no. 9, pp. 1–6, 2017.

[25] Y. Wang, Q. Zhang, L. Zhao, Y. Tang, A. Shkel, and E. S. Kim, "Vibration energy harvester with low resonant frequency based on flexible coil and liquid spring," *Applied Physics Letters*, vol. 109, no. 20, p. 203901, 2016.

[26] H. R. Yun, D. J. Lee, J. R. Youn, and Y. S. Song, "Ferrohydrodynamic energy harvesting based on air droplet movement," *Nano Energy*, vol. 11, pp. 171–178, 2015.

[27] D. Kim, S. Yu, B.-G. Kang, and K.-S. Yun, "Electrostatic energy harvester using magnetically actuated liquid dielectric layers," *Journal of Microelectromechanical Systems*, vol. 24, no. 3, pp. 516–518, 2015.

[28] A. Bibo, R. Masana, A. King, G. Li, and M. F. Daqaq, "Electromagnetic ferrofluid-based energy harvester," *Physics Letters A*, vol. 376, no. 32, pp. 2163–2166, 2012.

[29] S. F. Alazemi, A. Bibo, and M. F. Daqaq, "A ferrofluid-based energy harvester: An experimental investigation involving internally-resonant sloshing modes," *The European Physical Journal Special Topics*, vol. 224, no. 14-15, pp. 2993–3004, 2015.

[30] S. Alazmi, Y. Xu, and M. F. Daqaq, "Harvesting energy from the sloshing motion of ferrofluids in an externally excited container: Analytical modeling and experimental validation," *Physics of Fluids*, vol. 28, no. 7, p. 077101, 2016.

[31] S. Alazemi, W. Lacarbonara, and M. F. Daqaq, "Harvesting energy from faraday waves," *Journal of Applied Physics*, vol. 122, no. 22, p. 224501, 2017.

[32] Y. S. Kim, "Analysis of electromotive force characteristics for electromagnetic energy harvester using ferrofluid," *Journal of Magnetics*, vol. 20, no. 3, pp. 252–257, 2015.

[33] M.-L. Seol, S.-B. Jeon, J.-W. Han, and Y.-K. Choi, "Ferrofluid-based triboelectric-electromagnetic hybrid generator for sensitive and sustainable vibration energy harvesting," *Nano Energy*, vol. 31, pp. 233–238, 2017.

[34] S. F. Alazemi and M. F. Daqaq, "Ferrofluids for concurrent vibration absorption and energy harvesting," in *ASME 2013 Conference on Smart Materials, Adaptive Structures and Intelligent Systems*, pp. V002T07A029–V002T07A029, American Society of Mechanical Engineers, 2013.

[35] J. P. McTague, "Magnetoviscosity of magnetic colloids," *The Journal of Chemical Physics*, vol. 51, no. 1, pp. 133–136, 1969.

[36] T. Seuaciuc-Osório and M. F. Daqaq, "Effect of bias conditions on the optimal energy harvesting using magnetostrictive materials," in *The 15th International Symposium on: Smart Structures and Materials & Nondestructive Evaluation and Health Monitoring*, pp. 69280B–69280B, International Society for Optics and Photonics, 2008.

[37] N. E. DuToit and B. L. Wardle, "Experimental verification of models for microfabricated piezoelectric vibration energy harvesters," *AIAA journal*, vol. 45, no. 5, pp. 1126–1137, 2007.

[38] A. Erturk and D. J. Inman, "A distributed parameter electromechanical model for cantilevered piezoelectric energy harvesters," *Journal of vibration and acoustics*, vol. 130, no. 4, p. 041002, 2008.

[39] S. Roundy and Y. Zhang, "Toward self-tuning adaptive vibration-based microgenerators," in *Smart Materials, Nano-, and Micro-Smart Systems*, pp. 373–384, International Society for Optics and Photonics, 2005.

[40] N. Stephen, "On energy harvesting from ambient vibration," *Journal of sound and vibration*, vol. 293, no. 1, pp. 409–425, 2006.

[41] J. M. Renno, M. F. Daqaq, J. R. Farmer, and D. J. Inman, "Parameter optimization of a vibration-based energy harvester with an rl electric circuit," in *ASME 2007 International Design Engineering Technical Conferences and Computers and Information in Engineering Conference*, pp. 787–794, American Society of Mechanical Engineers, 2007.

[42] B. Mann and N. Sims, "Energy harvesting from the nonlinear oscillations of magnetic levitation," *Journal of Sound and Vibration*, vol. 319, no. 1, pp. 515–530, 2009.

[43] V. R. Challa, M. Prasad, Y. Shi, and F. T. Fisher, "A vibration energy harvesting device with bidirectional resonance frequency tunability," *Smart Materials and Structures*, vol. 17, no. 1, p. 015035, 2008.

[44] Q. Liu, S. F. Alazemi, M. F. Daqaq, and G. Li, "A ferrofluid based energy harvester: Computational modeling, analysis, and experimental validation," *Journal of Magnetism and Magnetic Materials*, vol. 449, pp. 105–118, 2018.

[45] Q. Liu, M. F. Daqaq, and G. Li, "Performance analysis of a ferrofluid-based electromagnetic energy harvester," *IEEE Transactions on Magnetics*, vol. 54, no. 5, p. 4600314, 2018.

[46] G. Matthies and L. Tobiska, "Numerical simulation of normal-field instability in the static and dynamic case," *Journal of Magnetism and Magnetic Materials*, vol. 289, pp. 346–349, 2005.

[47] S. M. Elborai, *Ferrofluid surface and volume flows in uniform rotating magnetic fields*. PhD thesis, Massachusetts Institute of Technology, 2006.

[48] S. R. Khushrushahi, *Ferrofluid spin-up flows from uniform and non-uniform rotating magnetic fields*. PhD thesis, Massachusetts Institute of Technology, 2010.

[49] L. Mao and H. Koser, "Ferrohydrodynamic pumping in spatially traveling sinusoidally time-varying magnetic fields," *Journal of Magnetism and Magnetic Materials*, vol. 289, pp. 199–202, 2005.

[50] A. M. Morega, A. A. Dobre, and M. Morega, "Numerical simulation of magnetic drug targeting with flow–structural interaction in an arterial branching region of interest," in *Comsol Conference*, pp. 17–19, 2010.

[51] S. Afkhami, L. J. Cummings, and I. M. Griffiths, "Interfacial deformation and jetting of a magnetic fluid," *Computers & Fluids*, vol. 124, pp. 149–156, 2016.

[52] H. Ki, "Level set method for two-phase incompressible flows under magnetic fields," *Computer Physics Communications*, vol. 181, no. 6, pp. 999–1007, 2010.

[53] J. Liu, S.-H. Tan, Y. F. Yap, M. Y. Ng, and N.-T. Nguyen, "Numerical and experimental investigations of the formation process of ferrofluid droplets," *Microfluidics and nanofluidics*, vol. 11, no. 2, pp. 177–187, 2011.

[54] U. Sen, S. Chatterjee, S. Sen, M. K. Tiwari, A. Mukhopadhyay, and R. Ganguly, "Dynamics of magnetic modulation of ferrofluid droplets for digital microfluidic applications," *Journal of Magnetism and Magnetic Materials*, vol. 421, pp. 165–176, 2017.

[55] S. Afkhami, Y. Renardy, M. Renardy, J. Riffle, and T. St Pierre, "Field-induced motion of ferrofluid droplets through immiscible viscous media," *Journal of Fluid Mechanics*, vol. 610, pp. 363–380, 2008.

[56] J. G. Marchetta and K. M. Roos, "Simulating magnetic positive positioning of cryogenic propellants in a transient acceleration field," *Computers & Fluids*, vol. 38, no. 4, pp. 843–850, 2009.

[57] J. M. Jin, *The finite element method in electromagnetics*. John Wiley & Sons, 2014.

[58] R. E. Rosensweig, *Ferrohydrodynamics*. Courier Corporation, 2013.

[59] M. Sussman, K. M. Smith, M. Y. Hussaini, M. Ohta, and R. Zhi-Wei, "A sharp interface method for incompressible two-phase flows," *Journal of computational physics*, vol. 221, no. 2, pp. 469–505, 2007.

[60] R. D. Cook *et al.*, *Concepts and applications of finite element analysis*. John Wiley & Sons, 2007.

[61] G. Tomar, D. Gerlach, G. Biswas, N. Alleborn, A. Sharma, F. Durst, S. W. J. Welch, and A. Delgado, "Two-phase electrohydrodynamic simulations using a volume-of-fluid approach," *Journal of Computational Physics*, vol. 227, no. 2, pp. 1267–1285, 2007.

[62] T. E. Tezduyar and Y. Osawa, "Finite element stabilization parameters computed from element matrices and vectors," *Computer Methods in Applied Mechanics and Engineering*, vol. 190, no. 3, pp. 411–430, 2000.

[63] T. E. Tezduyar, *Stabilized finite element formulations for incompressible flow computations*. Academic Press, 1992.

[64] A. N. Brooks and T. J. R. Hughes, "Streamline upwind/petrov-galerkin formulations for convection dominated flows with particular emphasis on the incompressible navier-stokes equations," *Computer methods in applied mechanics and engineering*, vol. 32, no. 1, pp. 199–259, 1982.

[65] C. W. Hirt and B. D. Nichols, "Volume of fluid (vof) method for the dynamics of free boundaries," *Journal of computational physics*, vol. 39, no. 1, pp. 201–225, 1981.

[66] E. G. Puckett, A. S. Almgren, J. B. Bell, D. L. Marcus, and W. J. Rider, "A high-order projection method for tracking fluid interfaces in variable density incompressible flows," *Journal of Computational Physics*, vol. 130, no. 2, pp. 269–282, 1997.

[67] R. Scardovelli and S. Zaleski, "Direct numerical simulation of free-surface and interfacial flow," *Annual review of fluid mechanics*, vol. 31, no. 1, pp. 567–603, 1999.

[68] D. Gueyffier, J. Li, A. Nadim, R. Scardovelli, and S. Zaleski, "Volume-of-fluid interface tracking with smoothed surface stress methods for three-dimensional flows," *Journal of Computational Physics*, vol. 152, no. 2, pp. 423–456, 1999.

[69] W. J. Rider and D. B. Kothe, "Reconstructing volume tracking," *Journal of computational physics*, vol. 141, no. 2, pp. 112–152, 1998.

[70] J. E. Pilliod and E. G. Puckett, "Second-order accurate volume-of-fluid algorithms for tracking material interfaces," *Journal of Computational Physics*, vol. 199, no. 2, pp. 465–502, 2004.

[71] D. B. Kothe, R. C. Mjolsness, and M. D. Torrey, *RIPPLE: a computer program for incompressible flows with free surfaces*. Available to DOE and DOE contractors from OSTI, 1991.

[72] M. M. Francois, S. J. Cummins, E. D. Dendy, D. B. Kothe, J. M. Sicilian, and M. W. Williams, "A balanced-force algorithm for continuous and sharp interfacial surface tension models within a volume tracking framework," *Journal of Computational Physics*, vol. 213, no. 1, pp. 141–173, 2006.

[73] S. Popinet, "An accurate adaptive solver for surface-tension-driven interfacial flows," *Journal of Computational Physics*, vol. 228, no. 16, pp. 5838–5866, 2009.

[74] S. J. Cummins, M. M. Francois, and D. B. Kothe, "Estimating curvature from volume fractions," *Computers & structures*, vol. 83, no. 6, pp. 425–434, 2005.

[75] G. X. Wu, Q. W. Ma, and R. E. Taylor, "Numerical simulation of sloshing waves in a 3d tank based on a finite element method," *Applied Ocean Research*, vol. 20, no. 6, pp. 337–355, 1998.

[76] S. Popinet and S. Zaleski, "A front-tracking algorithm for accurate representation of surface tension," *International Journal for Numerical Methods in Fluids*, vol. 30, no. 6, pp. 775–793, 1999.

[77] D. Gerlach, G. Tomar, G. Biswas, and F. Durst, "Comparison of volume-of-fluid methods for surface tension-dominant two-phase flows," *International Journal of Heat and Mass Transfer*, vol. 49, no. 3, pp. 740–754, 2006.

[78] M. Herrmann, "A balanced force refined level set grid method for two-phase flows on unstructured flow solver grids," *Journal of Computational Physics*, vol. 227, no. 4, pp. 2674–2706, 2008.

[79] R. A. Ibrahim, *Liquid sloshing dynamics: theory and applications*. Cambridge University Press, 2005.

[80] S. R. Idelsohn, E. Oñate, and F. D. Pin, "The particle finite element method: A powerful tool to solve incompressible flows with free-surfaces and breaking waves," *International journal for numerical methods in engineering*, vol. 61, no. 7, pp. 964–989, 2004.

[81] A. Colagrossi, C. Lugni, and M. Brocchini, "A study of violent sloshing wave impacts using an improved sph method," *Journal of hydraulic research*, vol. 48, no. S1, pp. 94–104, 2010.

[82] G. A. Flores, J. Liu, M. Mohebi, and N. Jamasbi, "Magnetic-field-induced nonequilibrium structures in a ferrofluid emulsion," *Physical Review E*, vol. 59, no. 1, p. 751, 1999.

[83] L. Shen, A. Stachowiak, S.-E. K. Fateen, P. E. Laibinis, and T. A. Hatton, "Structure of alkanoic acid stabilized magnetic fluids. a small-angle neutron and light scattering analysis," *Langmuir*, vol. 17, no. 2, pp. 288–299, 2001.

[84] M. Klokkenburg, R. P. Dullens, W. K. Kegel, B. H. Erné, and A. P. Philipse, "Quantitative real-space analysis of self-assembled structures of magnetic dipolar colloids," *Physical review letters*, vol. 96, no. 3, p. 037203, 2006.

[85] E. W. Chuan Lim and R. Feng, "Agglomeration of magnetic nanoparticles," *The Journal of chemical physics*, vol. 136, no. 12, p. 124109, 2012.

[86] E. Siebert, V. Dupuis, S. Neveu, and S. Odenbach, "Rheological investigations on the theoretical predicted "poisoning" effect in bidisperse ferrofluids," *Journal of Magnetism and Magnetic Materials*, vol. 374, pp. 44–49, 2015.

[87] P. Teixeira, J. Tavares, and M. T. da Gama, "The effect of dipolar forces on the structure and thermodynamics of classical fluids," *Journal of Physics: Condensed Matter*, vol. 12, no. 33, p. R411, 2000.

[88] A. Y. Zubarev and L. Y. Iskakova, "Theory of structural transformations in ferrofluids: Chains and "gas-liquid" phase transitions," *Physical Review E*, vol. 65, no. 6, p. 061406, 2002.

[89] K. I. Morozov and M. I. Shliomis, "Ferrofluids: flexibility of magnetic particle chains," *Journal of Physics: Condensed Matter*, vol. 16, no. 23, p. 3807, 2004.

[90] A. O. Ivanov, Z. Wang, and C. Holm, "Applying the chain formation model to magnetic properties of aggregated ferrofluids," *Physical Review E*, vol. 69, no. 3, p. 031206, 2004.

[91] V. S. Mendelev and A. O. Ivanov, "Ferrofluid aggregation in chains under the influence of a magnetic field," *Physical Review E*, vol. 70, no. 5, p. 051502, 2004.

[92] C. Holm, A. Ivanov, S. Kantorovich, E. Pyanzina, and E. Reznikov, "Equilibrium properties of a bidisperse ferrofluid with chain aggregates: theory and computer simulations," *Journal of Physics: Condensed Matter*, vol. 18, no. 38, p. S2737, 2006.

[93] A. O. Ivanov, S. S. Kantorovich, V. S. Mendelev, and E. S. Pyanzina, "Ferrofluid aggregation in chains under the influence of a magnetic field," *Journal of Magnetism and Magnetic Materials*, vol. 300, no. 1, pp. e206–e209, 2006.

[94] S. Kantorovich, J. J. Cerda, and C. Holm, "Microstructure analysis of monodisperse ferrofluid monolayers: theory and simulation," *Physical Chemistry Chemical Physics*, vol. 10, no. 14, pp. 1883–1895, 2008.

[95] J. J. Cerdà, E. Elfimova, V. Ballenegger, E. Krutikova, A. Ivanov, and C. Holm, "Behavior of bulky ferrofluids in the diluted low-coupling regime: Theory and simulation," *Physical Review E*, vol. 81, no. 1, p. 011501, 2010.

[96] J. O. Sindt and P. J. Camp, "Simulations of dipolar fluids using effective many-body isotropic interactions," *The Journal of chemical physics*, vol. 143, no. 2, p. 024501, 2015.

[97] P. Jund, S. Kim, D. Tománek, and J. Hetherington, "Stability and fragmentation of complex structures in ferrofluids," *Physical review letters*, vol. 74, no. 15, p. 3049, 1995.

[98] E. Lomba, F. Lado, and J. Weis, "Structure and thermodynamics of a ferrofluid monolayer," *Physical Review E*, vol. 61, no. 4, p. 3838, 2000.

[99] Z. Wang, C. Holm, and H. W. Müller, "Molecular dynamics study on the equilibrium magnetization properties and structure of ferrofluids," *Physical Review E*, vol. 66, no. 2, p. 021405, 2002.

[100] Z. Wang and C. Holm, "Structure and magnetic properties of polydisperse ferrofluids: A molecular dynamics study," *Physical Review E*, vol. 68, no. 4, p. 041401, 2003.

[101] J. Weis, J. Tavares, and M. T. Da Gama, "Structural and conformational properties of a quasi-two-dimensional dipolar fluid," *Journal of Physics: Condensed Matter*, vol. 14, no. 40, p. 9171, 2002.

[102] J. Weis, "Simulation of quasi-two-dimensional dipolar systems," *Journal of Physics: Condensed Matter*, vol. 15, no. 15, p. S1471, 2003.

[103] M. Aoshima and A. Satoh, "Two-dimensional monte carlo simulations of a polydisperse colloidal dispersion composed of ferromagnetic particles for the case of no external magnetic field," *Journal of colloid and interface science*, vol. 280, no. 1, pp. 83–90, 2004.

[104] J. Huang, Z. Wang, and C. Holm, "Computer simulations of the structure of colloidal ferrofluids," *Physical Review E*, vol. 71, no. 6, p. 061203, 2005.

[105] Y. Xuan, M. Ye, and Q. Li, "Mesoscale simulation of ferrofluid structure," *International Journal of Heat and Mass Transfer*, vol. 48, no. 12, pp. 2443–2451, 2005.

[106] P. D. Duncan and P. J. Camp, "Aggregation kinetics and the nature of phase separation in two-dimensional dipolar fluids," *Physical review letters*, vol. 97, no. 10, p. 107202, 2006.

[107] J. Tavares, J. Weis, and M. T. da Gama, "Phase transition in two-dimensional dipolar fluids at low densities," *Physical Review E*, vol. 73, no. 4, p. 041507, 2006.

[108] J. J. Cerdà, S. Kantorovich, and C. Holm, "Aggregate formation in ferrofluid monolayers: simulations and theory," *Journal of Physics: Condensed Matter*, vol. 20, no. 20, p. 204125, 2008.

[109] P. Ilg, "Importance of depletion interactions for structure and dynamics of ferrofluids," *The European Physical Journal E: Soft Matter and Biological Physics*, vol. 26, no. 1, pp. 169–176, 2008.

[110] P. Ilg and E. Del Gado, "Non-linear response of dipolar colloidal gels to external fields," *Soft Matter*, vol. 7, no. 1, pp. 163–171, 2011.

[111] B. Tanygin, V. Kovalenko, M. Petrychuk, and S. Dzyan, "Molecular dynamics study of the primary ferrofluid aggregate formation," *Journal of Magnetism and Magnetic Materials*, vol. 324, no. 23, pp. 4006–4010, 2012.

[112] R. Weeber, M. Klinkigt, S. Kantorovich, and C. Holm, "Microstructure and magnetic properties of magnetic fluids consisting of shifted dipole particles under the influence of an external magnetic field," *The Journal of chemical physics*, vol. 139, no. 21, p. 214901, 2013.

[113] S. Thurm and S. Odenbach, "Particle size distribution as key parameter for the flow behavior of ferrofluids," *Physics of Fluids*, vol. 15, no. 6, pp. 1658–1664, 2003.

[114] S. S. Kantorovich, "Chain aggregate structure in polydisperse ferrofluids: different applications," *Journal of magnetism and magnetic materials*, vol. 289, pp. 203–206, 2005.

[115] P. J. Camp, E. A. Elfimova, and A. O. Ivanov, "The effects of polydispersity on the initial susceptibilities of ferrofluids," *Journal of Physics: Condensed Matter*, vol. 26, no. 45, p. 456002, 2014.

[116] S. Han, J. Li, R. Gao, T. Zhang, and B. Wen, "Study of magnetisation behaviours for binary ionic ferrofluids," *Journal of Experimental Nanoscience*, vol. 4, no. 1, pp. 9–19, 2009.

[117] R. Gao, J. Li, S. Han, B. Wen, T. Zhang, H. Miao, and Q. Zhang, "Magnetisation behaviour of mixtures of ferrofluids and paramagnetic fluids with same particle volume fractions," *Journal of Experimental Nanoscience*, vol. 7, no. 3, pp. 282–297, 2012.

[118] P. Ilg, M. Kröger, and S. Hess, "Magnetoviscosity of semidilute ferrofluids and the role of dipolar interactions: Comparison of molecular simulations and dynamical mean-field theory," *Physical Review E*, vol. 71, no. 3, p. 031205, 2005.

[119] P. Ilg, M. Kröger, and S. Hess, "Anisotropy of the magnetoviscous effect in ferrofluids," *Physical Review E*, vol. 71, no. 5, p. 051201, 2005.

[120] Y. Yamada and Y. Enomoto, "Effects of oscillatory shear flow on chain-like cluster dynamics in ferrofluids without magnetic fields," *Physica A: Statistical Mechanics and its Applications*, vol. 387, no. 1, pp. 1–11, 2008.

[121] A. Leschhorn, J. Embs, and M. Lücke, "Magnetization of rotating ferrofluids: the effect of polydispersity," *Journal of Physics: Condensed Matter*, vol. 18, no. 38, p. S2633, 2006.

[122] S. Plimpton, "Fast parallel algorithms for short-range molecular dynamics," *Journal of computational physics*, vol. 117, no. 1, pp. 1–19, 1995.

[123] W. Humphrey, A. Dalke, and K. Schulten, "Vmd: visual molecular dynamics," *Journal of molecular graphics*, vol. 14, no. 1, pp. 33–38, 1996.

[124] O. C. Zienkiewicz, R. L. Taylor, and P. Nithiarasu, *The Finite Element Method for Fluid Dynamics*. Butterworth-Heinemann, 2005.